Bioactive microstructures for enhanced cardiac recovery after myocardial infarction

by

Priya Mohindra

DISSERTATION

Submitted in partial satisfaction of the requirements for degree of

DOCTOR OF PHILOSOPHY

in

Bioengineering

in the

GRADUATE DIVISION

of the

UNIVERSITY OF CALIFORNIA, SAN FRANCISCO
AND
UNIVERSITY OF CALIFORNIA, BERKELEY

Approved:

DocuSigned by:
Tejal A. Desai — Tejal A. Desai
5D917BC35F4B4A0...
Chair

DocuSigned by:
Matthew Springer — Matthew Springer
DocuSigned by:
Ting Xu — Ting Xu
02729C5B9AB3414...

Committee Members

Dedication and Acknowledgements

This dissertation would not have been possible without the endless support and guidance I've received from advisors, colleagues, friends, and family. I am so thankful for each one of you. I would not have been able to accomplish as much as I have without your constant encouragement.

Firstly, I would like to sincerely thank my advisor, Dr. Tejal Desai, for giving me the opportunity to pursue my scientific interests and focus my graduate research on developing novel translational biomaterial-based therapies. Throughout graduate school, she always challenged me to think about the bigger picture and approach experimental design in a rigorous manner. The drive to create high quality, safe, and efficacious therapies was instilled into me as a lab member, and I will carry this passion as I continue my work in the scientific field. After five years in her lab, I have watched myself transform into a confident, resourceful, and resilient scientist and I will forever be thankful for this personal growth I've experienced while in her lab.

I would also like to thank my qualifying exam committee– Dr. Tamara Alliston, Dr. Guo Huang, Dr. Matt Springer, and Dr. Phil Messersmith– for their continued support and feedback as I developed my research proposal. Additionally, I would like to sincerely thank my dissertation committee– Dr. Tejal Desai, Dr. Matt Springer, and Dr. Ting Xu– for their guidance and expertise as I navigated my thesis work.

Throughout my PhD, I had the opportunity to work with many scientific collaborators whose guidance and efforts have been crucial to producing the data that are detailed in this dissertation. I would like to thank Dr. Randall Lee, Dr. Qizhi Fang, Richard Sievers, and Dr. Dongwei Gao as well as Dr. Matt Springer and Dr. Huiliang

Qui for their invaluable contributions to the all work pertaining to the ischemia-reperfusion myocardial infarction models. I am also extremely grateful to Dr. Bhushan Kharbikar and Dr. Xiao Huang for always being willing to share their expertise regarding microfabrication and imaging techniques, respectively. Through working with all of you, I have learned so much and have become a better scientist.

To my labmates, your friendship and support both inside and outside of the lab has made my Ph.D. experience so memorable. The friendships I've made with Gauree Chendke, Long Le, Liz Levy, Joel Finbloom, Yiqi Cao, Karen Samy, and Will Lykins are those that I will cherish and I'm so happy they came into my life. Long, you not only exemplified all the qualities of an outstanding mentor, but those of a wonderful friend as well. Thank you for going above and beyond to make sure I was well supported both in and outside the lab. I will miss our boba runs, wine and cheese nights, and all-around food-centric conversations but am excited to know that there will be many more in the future. Liz, thank you for always being willing to troubleshoot science with me and for the endless entertainment from bonding over our love for Leia to lab shenanigans. I am so grateful I got the opportunity to travel with you and share some incredible experiences that I will never forget; and I am very happy to call you a close friend. Joel, thank you for always making time, being willing to listen, and sharing your advice with me no matter how busy you were. I've learned so many invaluable things from you over the past few years– from important concepts relating to conjugation chemistry all the way to where the best ice cream in SF is located. I'm very grateful that you (and Shasta) came into my life. Yiqi, I am so thankful I got the opportunity to sit next to you in lab. I'll miss our scientific discussions such as qPCR controls and biological vs. technical

replicates. But most of all, I'll miss the intense laughing (borderline wheezing) we would do at literally anything and everything that happened. I absolutely loved traveling with you and am so happy we got to create even more hilarious memories together. Karen, thank you so much for being so selfless with your time and for your motivational talks whenever I had a question about how to proceed or lost confidence. There was never a dull moment in lab with you around and I'll miss hearing your laughs from the Byers hallway. Will, thank you so much for you brightening the lab every day with your laughs, witty comments, and overall love for science. You took it upon yourself to make sure everyone felt supported and never hesitated to offer help to those who around you. This sentiment is at the core of our lab culture, and you were at the heart of it. Thank you all for being such inspiring and incredible, lifelong friends.

I would like to sincerely thank Gauree– your unwavering friendship and support has kept me grounded through the highs and lows of graduate school and has been instrumental in allowing me to accomplish all that I have thus far. You have been there for me at every step of my PhD journey, whether troubleshooting a failed positive control, commiserating over broken equipment, or celebrating passing my qualifying exam. Not only that, but you've been a major part of my life outside of lab and I am so thankful for all the wonderful memories we've been able to share throughout the years. I'm so grateful this PhD has brought you as my best friend into my life and I can't wait to see firsthand all that you'll accomplish in the future.

Of course, none of this would have been possible without the unconditional love and support of my family. My parents have been important role models for me my entire life. Watching them become experts in their respective fields inspired me to reach

higher within my own field as well. I would not have had the confidence to apply to graduate programs and believe that I could earn a PhD without your constant words of encouragement. I'm grateful to my siblings for always being ready and willing to listen to me talk about science regardless of whether they understood what I was talking about. Thank you all for always believing that I can achieve anything I set my mind to.

And lastly, thank you Eric for being my fiercest advocate and loudest cheerleader. I am so grateful to have had you by my side while I tackled the most difficult and rewarding experience of my career thus far. You were always there to boost my confidence on days when experiments didn't go as planned, and selfless with your time and energy to make sure my workload was easier and that my mental health was taken care of. I'll treasure our shared commiseration over the seemingly endless work of graduate school but am very excited to begin making new memories with you.

Contributions

Chapter 1 was modified from “Micro- and nanoscale biophysical cues for cardiovascular disease therapy”, a review article that was published by Priya Mohindra and Tejal A. Desai in the journal *Nanomedicine: Nanotechnology, Biology and Medicine* in June 2021 and “Biomaterials to enhance stem cell transplantation”, a review article that was published by Bhushan N. Kharbikar, Priya Mohindra, and Tejal A. Desai in the journal *Cell Stem Cell* in April 2022. Chapter 2 was modified from “Injectable hyaluronic acid based microrods provide local micromechanical and biochemical cues to attenuate cardiac fibrosis after myocardial infarction”, a research article that was published by Long V. Le, Priya Mohindra, *et al.* in *Biomaterials* in July 2018. Chapter 4 includes work that is in preparation for submission to a peer-reviewed journal for publication.

Bioactive microstructures for enhanced cardiac recovery after myocardial infarction

Priya Mohindra

Abstract

Myocardial infarction (MI) is the leading cause of heart failure (HF) and despite advances in the management of MI, subsequent pathologic remodeling of ischemic myocardium with fibrotic scar tissue and aneurysmal degeneration leads to HF and death. Early attempts at stem cell delivery and biological therapeutics to promote positive remodeling following MI have been promising but inconsistent and often involve systemic inhibition of signaling factors, which can have unintended side effects. A compelling approach to combat pathological cellular processes that often arise due to myocardial injury includes engineering materials to mimic biological and physical traits of native ECM architecture to provide biophysical cues that may yield more healthy cell phenotypes.

This dissertation describes the therapeutic applications of biophysical cues in cardiovascular diseases (CVDs), specifically myocardial infarction and heart failure. First, Chapter 1 provides a comprehensive discussion regarding how nano- and microscale biophysical cues affect the phenotypes and behaviors of key cardiovascular cells– cardiomyocytes, fibroblasts, and endothelial cells– and how these resulting effects may be leveraged for therapeutic success in CVDs. Chapter 2 then details the development of a biodegradable polymeric microstructure technology made of hyaluronic acid. In this study, we investigated how hyaluronic acid microrods affect

fibroblast phenotype and if they can improve cardiac outcomes in rodent models of ischemia-reperfusion (I/R) MI injury. We demonstrated that treatment with hyaluronic acid microrods decreases fibrotic phenotype in fibroblasts as well as exhibits enhanced cardiac function and decreased fibrosis after 6 weeks post-MI. Further, treatment with hyaluronic acid microrods outperformed treatment with equivalent mass of soluble hyaluronic acid material control, indicating the importance of the material geometry.

Beyond physical regulation of cellular behaviors by topographical cues, the incorporation of biochemical factors may further enhance the efficacy of these therapeutic strategies. As such, Chapter 3 comprises studies that probed the effects of several pro-angiogenic stimuli (i.e., Qk, RoY, and HepIII peptides) on endothelial cells and the feasibility of conjugating them onto hyaluronic acid microrods to create dual-pronged strategy that tackled both rampant fibrosis and lack of vascularization that occur post-MI. Chapter 4 follows a similar approach but investigates the therapeutic effects of a decorin-loaded hyaluronic acid microrod strategy in rodent models of I/R MI injury. Here, we demonstrate distinguishable improvement in cardiac function and ventricular remodeling and decreased fibrosis and cardiomyocyte hypertrophy in animals treated with decorin-loaded hyaluronic acid microrods. Together, this body of work aims to contribute important knowledge to help develop rationally designed, engineered biomaterials that may be used to successfully treat CVDs.

Table of Contents

List of Figures

List of Tables

Chapter 1 – Micro- and nanoscale biophysical regulation of cardiovascular cells for cardiovascular disease therapy

1.1. Introduction

Cardiovascular diseases (CVDs) remain the leading cause of death worldwide and continue to place debilitating health and economic burdens on global communities today. Current projections anticipate worsening conditions worldwide with CVDs estimated to cause 22.2 million deaths and cost over $1 trillion by 2030.[1,2] CVDs refer to a range of conditions that affect proper functioning of the heart and blood vessels. These conditions include ischemic heart disease, cerebrovascular disease, and coronary artery disease which often result from atherosclerosis and represent the largest proportion of CVDs.[3] Other conditions such as congenital heart disease, rheumatic heart diseases, cardiomyopathies, and cardiac arrythmias are also included.[3] In many of these pathologies, the onset of cardiovascular tissue damage and dysfunction triggers wound repair mechanisms that lead to stark changes in resident cell behaviors as well as in the native cellular microenvironment.

Several physiological events and processes that are important when discussing cellular response in CVDs include cell death[4], inflammation[5], hypertrophy[6], fibrosis[7,8], and impaired endothelial function[9] and vascularization.[10] Many of these reparative responses function as compensatory mechanisms tasked with salvaging and preventing further insult. Even so, morbidity and mortality of CVDs worsen when these wound healing responses become pathologic and ultimately contribute to disease progression. In the case of myocardial infarction (MI), profound cardiomyocyte death triggers a robust inflammatory response and fibrosis results in order to maintain the structural

integrity of the weakened myocardium. Cardiomyocyte hypertrophy in non-infarcted myocardium may also occur to compensate for lost myocyte volume due to cell death.[11] However, problems arise when deposited granulation tissue disrupts myocyte contractility and endothelial cell (EC) proliferation is insufficient to compensate for enlarged myocytes: this results in an increased oxygen diffusion distance and an exacerbated disease state.[12–14]

Owing to these altered cell phenotypes, it is therefore important to dictate and control cellular responses after cardiovascular injury in order to provide more favorable microenvironments that promote wound healing resolution and tissue repair mechanisms. As such, CVD therapies should focus on modulating the function of cell types adversely impacted during CVD pathologies, such as cardiomyocytes, fibroblasts, and ECs. Many strategies have explored regulating cell behavior and mitigating CVD processes through the use of biologics, pharmacological agents, and cell-based therapies. However, these interventions have had limited success in promoting long-term cardiovascular repair, with reasons including inefficient delivery and short half-life of therapeutic factors,[15,16] as well as poor engraftment, survival, and differentiation of transplanted cells.[17,18] Therefore, technologies that provide continuous cues to recapitulate native tissue architectures and appropriately guide cell behavior may yield higher therapeutic success for the treatment of CVDs.

It is well established that many cell types are mechanosensitive and that their biological behaviors vary in response to physical cues sensed in their microenvironment.[19,20] In the human body, the extracellular matrix (ECM) is a unique environmental niche composed of fibrillar and laminar structural components that

provide micro- and nanoscale biophysical cues to resident cells. In the myocardium, linear bundles of collagen (120 – 150 nm in diameter) connect adjacent myocytes and networks of coiled perimysial fibers (1 – 10 μm in diameter) are present throughout the muscle and ventricular wall.[21,22] The ECM surrounding cardiac cells exhibits average pores sizes of 21.4 μm as seen in decellularized porcine myocardium.[23] Further, topographies present within vascular basement membranes consist of pores and fibers that span the submicron (100 – 1000 nm) and nanoscale (1 – 100 nm) range.[24] Physical cues such as these can influence and dictate cellular behavior like adhesion, orientation, morphology, and phenotype through a phenomenon called “contact guidance”.[25,26] As such, it has become increasingly compelling to harness these micro- and nanoscale cell-substrate interactions to elicit more native, non-diseased cell behaviors that impede progression of CVD pathological processes and enhance regenerative potential.

Chapter 1 seeks to highlight and discuss recent *in vitro* and *in vivo* work that has investigated the therapeutic implications of micro- and nanoscale topography at the cellular level and highlight preclinical studies that have utilized biophysical cues as therapeutic strategies in CVD models. In particular, we focus on studies regarding cell types involved in CVDs— cardiomyocytes, fibroblasts, and ECs. A full discussion regarding methods of micro- and nanofabrication and the mechanisms by which these topographies modulate cell behavior is beyond the scope of this chapter and can be found elsewhere.[19,27–29] Further, while an understanding of how biophysical cues alter platelet interactions and influence material hemocompatibility demands consideration when developing materials-based strategies for CVDs, this topic will not be covered in

this chapter and readers are directed elsewhere.[30,31] Lastly, while the term “biophysical cues” is inclusive of characteristics ranging from stiffness, geometry, externally applied forces, material chemistry, and surface wettability, this chapter will focus on the effect of geometry-based topographic cues on cardiovascular cell types.

1.2. Micro- and nanoscale biophysical cues to modulate cellular function

1.2.1. Cardiomyocytes

Due to the poor prognosis of current pharmacological and surgical interventions, as well as the limited regenerative potential of mature cardiomyocytes, stem cell transplantations hold great promise to regenerate and restore cardiovascular tissue function. However, stem cell-based clinical trials have shown limited functional recovery of the myocardium and vasculature mainly due to low survival and retention of transplanted stem cells.[32] The emerging biomaterial-facilitated stem cell transplantation methods are poised to improve the overall outcomes of stem cell therapy.

Both biochemical and biophysical attributes of the biomaterial play important roles in facilitating the efficacy of stem cell transplantation for cardiovascular purposes. Notably, the abilities to recapitulate appropriate architecture in the native cardiac microenvironment as well as bestow mechanical properties that can withstand the contractile mechanisms of the heart are imperative. By providing a 3D structural scaffold for the transplanted cells, not only is cell retention in the target site greatly increased, but the ability to provide key physical cues to aid in stem cell differentiation into functional myocytes can be achieved.[33] Mechanical stiffness, nanotopographic architecture, physical stretch, and anisotropic patterns have all been shown to guide the

differentiation of stem cells with success.[33] Proteins, growth factors, genes, and microRNA have all also been used to modulate the biochemical microenvironment to one that is more amenable to cardiac repair.[34–36]

The native myocardial architecture features directionally dependent behavior in both mechanical and electrical properties, known as cardiac anisotropy. During therapeutic intervention, it has become increasingly apparent that inability to ensure appropriate cardiomyocyte orientation, differentiation, and intercellular connections post-transplantation could have dire consequences, such as poor host-graft interactions and lethal arrythmias.[37,38] As such, recent efforts have successfully designed substrates that provide directional cues to developing cells *in vitro* that yield cardiomyocytes with better morphological, conductive, and mechanical properties compared to counterparts grown in the absence of these features. Understanding how biophysical cues can be harnessed to increase cardiomyocyte maturation will inform clinical strategies that exogenously deliver stem cells with better host-integration and function and those that aim to restore normative function to endogenous cardiomyocytes during CVDs. This section will discuss *in vitro* findings pertaining to how physical cues have promoted more mature cardiomyocyte phenotypes by modulating alignment, morphology, gene and protein expression, and contractile behavior of cells. *In vivo* studies that have explored using topographic cues to improve disease outcomes by augmenting cardiomyocyte maturation and function in CVD preclinical models will be discussed. Additionally, implications for biophysical cues in drug discovery and screening for CVDs will be explored.

In vitro cardiomyocyte responses to micro- and nanotopography

In the native myocardium, regional cardiomyocyte alignment leads to global arrangements of cardiac muscle fibers which can effectively coordinate anisotropic myocardial contractions and electrical signal propagation. Adult cardiomyocytes are generally characterized as having high aspect ratios (~7:1),[39,40] containing parallel arrays of laterally registered sarcomeres,[41] and having end-to-end polarization of gap junction proteins[42,43]. Studies culturing cells on anisotropic micro- and nano-topographies have demonstrated that biophysical cues can dictate numerous aspects of cardiomyocyte behaviors that may have important implications for translational impact. Through dynamic organization of focal adhesions, cardiomyocytes are capable of interacting with and responding to physical cues on substrata.[44] However, topographic modulation is dependent on intact cellular mechano-signaling capabilities[44] and continuous presence of patterned cues[45] as otherwise, the observed effects are negated. Various studies have demonstrated increased alignment, aspect ratio, and elongated, cross-striated sarcomere structures in cardiomyocytes when cultured on patterned surfaces compared to unpatterned surfaces. Interrogation of geometric constraints on cardiomyocyte behavior indicate that alignment may be more dependent on feature width than aspect ratio[46] and that there are ideal size regimes that promote morphological indices such as increased cell areas, elongation, and sarcomere lengths in cardiomyocytes.[47] Sarcomere length is also an important indicator of cardiac maturity as it directly correlates with the amount of force that can be generated from cell contractions.[48] Adult cardiomyocyte sarcomeres range from 1.8 – 2.1 μm in length,[39]

whereas immature human induced pluripotent stem cell-derived cardiomyocytes (hiPSC-CMs) have lengths of ~1.65 μm.[49]

Cx43 is a key gap junction protein important for normal electrophysiological function and is preferentially located on the axial ends of mature cardiomyocytes to enable the generation of high contractile forces and rapid conduction between adjacent cells.[42,43] Many studies have reported higher Cx43 expression[50–53] and characteristic end-to-end polarization of Cx43 on patterned substrates[51,52,54], both of which are indicative of mature contractile function. The ability to control Cx43 end-to-end polarization will be crucial to ensuring efficient electrical activation and potential propagation, as lateral Cx43 distribution often impedes electrical conduction and is frequently observed in CVDs.[55] Studies have also successfully utilized a combination of conductive material,[52] electrical stimulation,[56] or mechanical stimulation[57] and physical cues to produce more mature cardiomyocyte phenotypes with increased expression of gap junction proteins, enhanced sarcomere density, and larger Z-band widths than patterns alone. The ability for topographical cues to increase expression of cardiac markers relating to early regulators of cardiomyogenesis and cardiac maturity when used alone[52,58–60] as well as in conjunction with directed differentiation and reprogramming protocols[61–63] have been documented. Morez *et al*. showed that parallel microgrooves enhanced lentivirus-mediated direct reprogramming of cells via topographical regulation of their epigenetic landscape.[62] Further, differentiation of hiPSC-CMs cultured on aligned poly lactic-co-glycolic acid (PLGA) fibrous scaffolds was significantly enhanced, as indicated by increased expression of genes encoding structural proteins alpha actinin), troponin T, and troponin I and Ca^{2+} handling proteins

like phospholamban and ryanodine receptor 2.[63,64] In addition to physical cues being able to enhance cardiac maturity at the transcriptional and translational level, these effects have been reported to increase functional characteristics such as contractile and electrophysiological capability of cardiomyocytes. Several studies have reported enhanced calcium transient synchronicity[65] and contraction force[66] of cardiomyocytes in the presence of microgrooves likely due to increased cell alignment and overall cell connectivity. Further, alignment and elongation of cells have been linked to enhanced contractile function. Cells on aligned scaffolds had significantly increased maximum contraction velocity,[60] beating rate,[51] and beating amplitude[51] compared to those on random scaffolds. Moreover, cells on tissue patches with higher aspect ratio pores and thus, more elongated morphologies, produced higher conduction velocity anisotropy ratios and twitch forces than cells on lower aspect ratio pores.[67]

Implications of micro- and nanotopography in CVD therapeutic strategies via cardiomyocyte modulation

While cell-based therapies for CVDs have generated a lot of interest, barriers to therapeutic success remain due to challenges in successful integration and appropriate function of delivered cells post-transplantation.[17,18,68] Progenitor cell-seeded material scaffolds have represented an exciting avenue for mitigating issues relating to insufficient cell retention in target tissues.[69,70] Further, material-based solutions are amenable to surface modifications and can deliver continuous cues to promote mature cardiomyocyte phenotypes in transplanted cells. Several labs have interrogated the effects of cell-seeded directional scaffolds on CVD outcomes. Lin *et al*. assessed the

effects of cell-seeded aligned- and random-oriented polyacrylonitrile nanofibrous patches on cardiac function and electrophysiology in rodent models of permanent-ligation MI.[51] Aligned cell-seeded patches yielded high survival of implanted cardiomyocytes that were also aligned with host cardiomyocytes and resulted in improved left ventricle ejection fraction (LVEF), mitigated ventricular dilation, and reduced infarct size 2 months post-MI. Interestingly, cell-seeded random patches resulted in deteriorated cardiac function and maladaptive cardiac remodeling similar to that of the MI control group, indicating the severity of poor host-graft interactions due to inappropriate cues. Aligned cell-seeded patches also improved post-MI electroconductivity and had high expression and polarization of Cx43, whereas cell-seeded random patches resulted in slower conductivities with Cx43 distribution around the nucleus.[51] In another study, Li *et al*. utilized cell-seeded aligned PLGA nanofibers and characterized preclinical therapeutic performance on permanent ligation post-MI outcomes. After 4 weeks, improved LVEF, increased fractional shortening, and decreased left ventricle (LV) end-systolic diameter was observed in cellular scaffolds versus acellular control scaffolds, demonstrating favorable ventricular remodeling outcomes.[64]

Beyond the use of directionally-aligned fiber scaffolds, a few groups have utilized unique micropattern designs, such as hexagon and honeycomb-like shapes, to produce cardiac patches that better recapitulate the architectural and mechanical properties of native myocardial tissue.[57,71] Cui *et al*. investigated the use of stretchable hexagon patterned cardiac patches for the treatment of murine models of chronic MI with ischemia/reperfusion (I/R) injury.[57] Beam-scanning stereolithography printing was used

to fabricate a physiologically adaptable design that mimicked spatiotemporal architecture and relevant biophysiochemical properties. A triculture of human-induced pluripotent stem cell (hiPSC) cardiomyocytes, human mesenchymal stromal cells, and human endothelial cells in the bioink consisting of gelatin methacrylate (GelMA) and polyethylene glycol diacrylate (PEGDA) was used to print the 4D cardiac tissue construct with anisotropic nonlinear microstructure to imitate epicardial fibers and the surrounding vascular network. Four months after epicardial implantation, while cellular cardiac patches demonstrated high engraftment rates and strong host-integration, implanted human induced pluripotent stem cell-derived endothelial cell (hiPSC-CMs) did not exhibit organized sarcomere structures, indicating immature phenotypes. Moreover, while both cellular and acellular cardiac patch groups demonstrated increased cardiac performance compared to MI control, their performance was equivalent. These results indicate that the mechanical support these patches offered was the primary mechanism for preventing maladaptive LV remodeling instead of enhanced cardiomyogenesis of implanted cells.[57] Kapnisi *et al.* explored the use of auxetic micropatterning to generate conductive cardiac patches that were capable of expanding in multiple directions to better accommodate the mechanical stress of the heart. In rodent models of permanent-ligation MI, no differences in fractional shortening, end diastolic volume, and end systolic volume were found between auxetic patch and MI control groups. However, higher LV mass in the control MI group indicated that the auxetic patch may have exerted some beneficial effects on cardiomyocytes by reducing mechanical stress experienced through bulking effects as opposed to topographical regulation of cells. To confirm this hypothesis, in-depth analysis of cardiomyocyte size and gene expression

would be required to assess the effect of auxetic patches on hypertrophy.[71] Other work has also utilized electrically-conductive carbon nanotube and nanofibers to augment electrophysiological therapeutic outcomes in infarcted myocardium.[72,73]

Another interesting avenue for biophysical cues to help progress work for viable CVD therapies is during drug screening and discovery. Over 30% of drug withdrawals from various markets between 1990 and 2006 were related to cardiotoxicity concerns, making cardiotoxicity determination a critical task during drug discovery.[74] Therefore, the use of physiologically representative *in vitro* models to identify therapeutic candidates can greatly minimize potential failures and health risks during clinical trials and expedite time spent during CVD drug development. Several published works have demonstrated that cells cultured on scaffolds with directional cues respond more robustly to drug challenges than cells on conventional culture systems and represent better alternatives to use during drug discovery.[63,64,66,75] To highlight the impact of more accurate culture models, one study analyzed a series of drugs that failed or were withdrawn from the market due to induction of torsades de pointes (Tdp), a potentially lethal form of arrhythmia. They found that an *in vitro* microgroove culture system was able to capture the torsadogenicity of these drugs whereas conventional culture systems had failed in detecting their cardiotoxicity prior to clinical trials.[76] Further, biophysical cues can also enable the visualization of more physiologically relevant and differential responses of diseased and healthy cardiomyocyte phenotypes *in vitro* during drug challenges, such as in the case of patient-specific long QT syndrome type 3 (LQT3) and Duchenne Muscular Dystrophy (DMD). Ma *et al*. found that on smaller diameter fibers, LQT3-iPS-CMs were more susceptible to drug-induced cardiac

arrythmias when compared to 2D pharmaceutical industry standard surfaces, potentially leading to high rates of false-negative readouts during toxicity testing if only traditional 2D cell culture systems are used for drug screening.[54] Another group found that myotubes derived from healthy and varying DMD severities had substantial differences in alignment when presented with topographic substrates— a finding that could provide an inexpensive phenotypic readout during high-throughput screening of DMD drugs.[77]

1.2.2. Fibroblasts

Fibroblasts make up the largest cell population in the heart and are responsible for coordinating numerous processes that maintain normal cardiac function. They coordinate synthesis and degradation of ECM, cell-cell signaling between cardiomyocytes, and cytokine and growth factor secretion.[78] Upon cardiovascular injury, fibroblasts become effector cells and transform into their activated myofibroblast phenotype under the influence of pro-inflammatory signals secreted during the wound healing response. Myofibroblasts predominantly function to increase ECM deposition to provide provisional matrices that stabilize the site of injury; in MI, this compensatory fibrosis maintains the mechanical integrity and pressure generating ability of the myocardium, reducing likelihood of myocardial dysfunction or rupture.[79] Issues arise when persistent inflammatory signals result in rampant fibrosis that may lead to chronic deposition of stiff, dense scar tissue that impairs contractility and perfusion mechanisms within the heart.[79] Mechanical cues have been reported to modulate fibroblast phenotype,[80,81] and as such, ongoing efforts aim to leverage fibroblast mechanosensing to yield quiescent fibroblast phenotypes that mitigate fibrotic response in CVDs and

minimize scar tissue formation around implanted devices. This section will discuss findings related to how these features affect fibroblast adhesion, proliferation, morphology, gene and protein expression, migration, and secretion profiles. Additionally, *in vivo* studies that have investigated the ability of topographic cues to improve therapeutic outcomes in CVDs by inhibiting fibrotic responses will be discussed.

In vitro fibroblast responses to micro- and nanotopography

Fibroblasts are sensitive to biophysical cues in their environment. The transduction of these signals by focal adhesions subsequently affect contractility mechanisms and heavily dictate their resulting behaviors.[19] Recent studies that have reported topography-induced modulation of fibroblast morphology and behavior are briefly summarized. During wound repair, fibroblasts can be activated by pro-fibrotic signals to increase proliferation and initiate differentiation into myofibroblasts. The use of biophysical cues have been documented to modulate fibroblast adhesion[82] and proliferation,[83,84] reporting unique size regimes that can promote or inhibit these behaviors. Identifying length scales that reliably dampen proliferative behaviors can prove essential to strategies aiming to mitigate rampant fibrotic response.

Myofibroblasts exhibit high expression of alpha-smooth muscle actin (ACTA2/α-SMA) in their stress fibers to augment contractile activity and aid in the generation of tissue contractures.[85] Further, myofibroblast characteristics include upregulated ECM protein secretion, matrix metalloproteinases (MMPs) synthesis, and cytokine production to promote ECM remodeling and fibrosis.[85] Many reports have discussed interesting

relationships between focal adhesion-dependent cytoskeletal tension, nucleus remodeling, and transcriptional activity.[83,86,87] This therefore opens up the possibility for geometric control of gene and protein expression profiles of fibroblast populations to discourage myofibroblast phenotypes. The formation of focal adhesions on substrates subsequently leads to cytoskeletal tension. Generated local tensile stresses governed by substrate properties (i.e. geometry, surface area, and aspect ratio) have been reported to affect cytoskeletal organization, remodeling of the nucleus, and chromatin compaction.[86] Another study showcased that changes in cell-geometry and nuclear morphology from underlying substrates can lead to reorientation of chromosome territories and result in differential transcriptional activity.[87] Cell proliferation and collagen secretion were found to strongly correlate with nuclear volume, highlighting the nucleus as a critical mechanosensor for fibroblast behavior.[83] Moreover, this same study showed that nuclear volume was effectively modulated by the height of nanotopography features through the rearrangement of focal adhesions, demonstrating the ability for topographies to influence cell behavior through nuclear remodeling.[83] These findings are in line with observations that have demonstrated how topography can physically influence fibroblast gene and protein expression and, of clinical relevance, how physical cues can suppress fibrotic activation as evidenced by decreased expression of ACTA2, collagen I (Col1A1), matrix metalloproteinase 2 (MMP2), and tafazzin (TAZ)[84,88–91] and reduced secretion of common pro-fibrotic cytokines.[91] Regular arrays of 4 x 2 μm adhesive islands allowed for fibroblast attachment and proliferation while simultaneously suppressing α-SMA organization into contractile fibers in the presence of TGF-β1, a potent pro-fibrotic cytokine.[84] Further,

discrete microscale polymeric structures have also shown to have success in decreasing gene expression of markers of the fibrotic phenotype in both 2D and 3D cultures regardless of material used.[88,89] However, not all variations of topographic patterns may result in attenuation of myofibroblast phenotypes. Cutiongco *et al*. recently developed a model to relate the effects of cell morphology to gene expression induced by nanotopography. Interestingly, they found that fibroblasts showed increased expression of pathogenic fibrosis markers on nanotopographic substrates compared to unpatterned surfaces. Interestingly, they did not observe any similarities in fibrotic gene expression profiles by nanotopographies induction versus biochemical fibrotic induction, indicating unique fibrosis signatures being elicited by these nanoscale physical patterns.[92]

During the wound healing response, fibroblasts are actively recruited to the injury via various signaling mechanisms such as IL-1β stimulation and angiotensin II type 1 receptor and β-adrenergic receptor activation.[79] Increased presence of these fibroblasts due to migration, much like with proliferation, greatly contributes to fibrosis progression. In terms of migration capability, numerous studies have reported that biophysical cues influence the migratory capacity of fibroblasts.[93–97] Cell migration on graphene oxide micropatterns revealed that the geometry of micropatterns (i.e. triangle, square) heavily influenced cell migration behavior including distance, speed, and directionality of travel and that migration likely correlated with observed cell morphology; cell migration distance and speed were significantly higher on triangle micropatterns than square micropatterns. Cells on square micropatterns were more spread than those on triangle patterns, which could have resulted in the slower migration behaviors.[94]

Another study corroborated the link between adhesive area and migration speed as nanopores that constrained adhesion areas resulted in increased migration speed as adhesive area decreased.[97] Further, it was found that there was increased migration, collagen synthesis, and proliferation on rough surfaces.[95] These studies all point to designs for topographical control of fibroblast behavior to include considerations for increasing cell adhesive area and reducing surface roughness.

Implications of micro- and nanotopography in CVD therapeutic strategies via fibroblast modulation

Therapeutic strategies that can successfully attenuate the fibrotic response have tremendous implications for the treatment of CVDs. After MI, onset of fibrosis can lead to stiffening of the myocardial wall and impede cardiac contractility, furthering disease progression and worsening morbidity outcomes.[79] Also, of importance, is the ability to prevent device failures and complications of medical implants due to fibrous encapsulation during FBR.[98–100]

In the context of MI, a few studies have demonstrated the therapeutic impact of intramyocardial injections of discrete microstructures for augmenting cardiac performance by attenuating cardiac fibrosis.[88,89,101] Pinney *et al*. compared the performance of injectable polyethylene glycol (PEG) microcube and microrod structures and demonstrated that both decreased collagen and TGF-β levels, increased elastin deposition, improved vascularization, and enhanced cardiac function after 6 weeks in rodent models of ischemia-reperfusion (I/R) MI.[89] Interestingly, while *in vitro* studies pointed to better performance of higher aspect ratio microrods, *in vivo* results

demonstrated that microcube structures saw increased cardiac performance as calculated by relative change in LVEF over the 6-week period post-MI.[89] Plausible explanations for these discrepancies between *in vitro* and *in vivo* performance may be attributed to (1) lower injection efficiency of the higher profile microrods and (2) increased surface area of the volume-controlled injection of microcubes. Further investigations into the mechanisms by which discrete microtopographical structures regulate fibroblast phenotype will inform whether higher aspect ratio structures, which can better resist cellular contractile forces, or higher surface area structures, which provide more adhesive area, are optimal for dictating therapeutic potential of microstructural strategies.

In a subsequent study, Le *et al*. investigated the performance of hyaluronic acid (HA) microrods compared to mass-controlled soluble HA injections in rodent models of I/R MI.[88] Improvements in morphological characteristics in the HA microrod group as evidenced by increased LV wall thickness and moderately reduced global LV collagen deposition were apparent.[88] However, the extent of fibrosis attenuation may have been underestimated due to the reporting of global collagen deposition as HA microrods provide a local anti-fibrotic response and only exert their mechanistic effects in their immediate area. This is corroborated histological analysis that demonstrates local reduction in collagen deposition in areas around HA microrod injections versus areas distal to the injection. Observed histological improvements correlated with functional assessments as both stroke volume and relative change in LVEF were greatly enhanced in the microrod group. Less significant improvements over saline were observed for soluble HA control, indicating that while HA itself does provide benefits

post-MI, the form factor of these structures was crucial to therapeutic efficacy. In a permanent ligation MI model, PEG microrods showed modest prevention of cardiac deterioration as measured by hemodynamic analysis and pathologic remodeling compared to MI controls.[101] Even so, PEG microrods attenuated gene expression of embryonic β-myosin heavy chain isoform and atrial natriuretic factor which are associated with pathological remodeling of the ventricles and preserved contractile efficiency after 10 weeks compared to MI control.[101] Overall, the use of injectable crosslinked hydrogel structures affords numerous benefits including fine control over geometry and stiffness, ability to release therapeutic factors,[101] and ease of injectability. Additionally, graphene oxide/alginate and reduced graphene oxide/alginate spherical microgels were investigated for their potential to protect delivered human mesenchymal stem cells (hMSCs) from oxidative stress after implantation into post-MI myocardium. While some therapeutic success was observed in the hMSC-loaded microgel group, minimal effects on fibrosis were observed for the microgel group alone.[102] It is interesting to note the differences in microstructure dosing, timing of administration, and MI models used across these studies and how these parameters may all influence therapeutic efficacy of microstructure strategies for MI treatment.

The potential of biophysical cues to mitigate FBR response to implanted devices has generated much excitement in the field of implantable biomaterials. Robotti *et al*. investigated the use of micropatterned hexagonal pits on biosynthesized cellulose (BC) membranes to reduce fibrous encapsulation of implanted pacemakers in a chronic minipig animal model.[103] Explants of both native and BC membrane protected pacemakers performed at 3 and 12 months after implantation showed that BC

pacemakers had no signs of degradation and had ~66% less fibrotic tissue generated around the device when compared to native device. Importantly, the generator and proximal parts of the leads were free from fibrotic tissue, highlighting the value of this anti-fibrotic membrane as complications with leads and the generator are commonly documented.[104,105] While not performed in this study, it would be interesting to parse out the contribution of BC as a material from the micropatterned features in reducing FBR to pacemakers. Results from these preclinical studies showcase the efficacy by which biophysical cues can exert anti-fibrotic effects in complex *in vivo* models of CVDs and how the attenuation of fibrotic mechanisms correlate to improved functional cardiovascular performance.

1.2.3. Endothelial Cells

The endothelium serves multiple functions in maintaining vascular homeostasis, playing crucial roles in processes including coagulation, thrombosis, platelet/leukocyte interactions, angiogenesis, and vasoconstriction/dilation.[106] The single layer of ECs that forms the lining of blood vessels is continuously exposed to diverse mechanical cues, including blood flow shear stress and ECM topographies, which help regulate behaviors such as proliferation, gene expression, and protein synthesis.[107] Dysfunction of vascular endothelium is highly associated with many CVDs and can be caused by various stimuli, like the formation of free radicals upon tissue injury. These pathological cues ultimately disrupt homeostatic mechanical regulation of ECs and activate pro-inflammatory and pro-thrombotic states that can contribute to cardiovascular conditions like peripheral artery disease (PAD) or restenosis after graft or stent implantation.[106]

Further, vascular grafts and stent failure modes often include inadequate endothelialization of the implanted material, greatly increasing thrombosis and neointimal hyperplasia risk.[108] Of particular importance is understanding how to harness EC mechanotransduction in therapeutic strategies to promote select behaviors that will enhance clinical outcomes. Recently published studies have showcased the use of topographical cues to obtain EC phenotypes that have enhanced proliferative behavior, reduced inflammatory state, and increased angiogenic potential. This section will briefly discuss how these features affect adhesion, proliferation, morphology, gene and protein expression, migration, and vascularization potential of ECs. Additionally, *in vivo* studies that have investigated the ability of topographic cues to improve disease outcomes by augmenting reendothelialization and vascularization potential will be discussed.

In vitro endothelial cell responses to micro- and nanotopography

The mechanosensitive nature of ECs has been detailed previously,[107] and studies culturing cells on patterned micro- and nanotopographies have demonstrated that physical cues can dictate various EC behaviors. In native endothelium, ECs align themselves along the axis of blood vessels to minimize shear stress caused by blood flow.[109] It has been elucidated that topographies can modulate preferential cell alignment, proliferation, and migration, through the regulation of endothelial adherens junctions and yes-associated protein 1 (YAP) nuclear localization.[110,111] Further, orientation, adhesion, and proliferation have been shown to be enhanced in geometries such as grooves,[112–115] wrinkles,[116] and fibers.[111,117,118] Studies utilizing groove patterns have found that widths of 1 μm were optimal to promote orientation, cell spreading, and

proliferation in ECs.[112,115] Synergies have also been found to exist between different length-scale topographies and their abilities to influence EC orientation, elongation, and spreading, which opens up the potential for multi-dimensional topographical modulation of these cells.[118] A critical observation was made Hagen *et al*. investigated the differential responses of carotid artery endothelial cells (CtAECs) and blood-derived endothelial cell colony forming cells (ECFCs) on micropatterned grooves and found that while alignment was robustly increased in both cell types, only CtAECs showed enhanced elongation on micropatterns.[113] Differential responses of various cell types and sources can have important implications for clinical strategies depending on the treatment site. Moreover, on low diameter fibers in 2D culture ECFC and human umbilical vein endothelial cell (HUVEC) morphology were found to be similar, but differences in cytoskeletal organization and deposited collagen patterns were observed on larger diameter fibers.[119]

A major barrier to endothelization of implants is the ability to maintain a confluent EC monolayer in the presence of physiological or greater wall shear stress (WSS) levels, such as those generated within vascular assist devices. Robotti *et al*. demonstrated that only cells cultured on 1 μm grooves had preserved monolayer integrity under high WSS; at physiological WSS, ECs were aligned with topography which was further reinforced by co-aligned flow direction.[120] However, at supraphysiological WSS, most ECs aligned themselves perpendicularly to the flow and topography direction.[120] When studying the effect of pre-polarizing ECs by culturing them on grooves oriented perpendicular to supraphysiological flow, they found endothelial layers with high connectivity index, alignment, and cell area had formed.

This demonstrated the ability for topographical surface modification to enhance endothelialization under supraphysiological flow conditions. ECs cultured on aligned scaffolds also had greater resistance to detachment compared to cells cultured on randomly-oriented and partially-aligned scaffolds.[121]

Topography-mediated alterations in EC gene expression and secretion profiles have been documented to yield phenotypes that reduce immunogenicity of ECs. These anti-inflammatory states are evidenced by reduced expression of vascular cell adhesion molecule 1 (VCAM1)[117,122,123], intercellular adhesion molecule 1 (ICAM1),[124] and platelet and endothelial cell adhesion molecule 1 (PECAM1),[112,117,123,124] increased secretion of nitric oxide,[125] collagen,[126] and elastin,[126] and reduced secretion of inflammatory cytokines IL-1β, interleukin 3 (IL-3), and MCP-1.[127] The ability to reduce pro-inflammatory activities in ECs is critical as they are implicated in the progression of atherosclerosis and restenosis.[128]

Further, enhanced migration capacity is associated with pro-angiogenic potential. Previous studies have demonstrated increased migratory potential on patterned features with regards to speed, persistence time, and distance when compared to flat substrates.[111,114,124,125,129] Gorji *et al*. observed significant increases in the migration of leader cells and, to a lesser extent, also follower cells after exposure to microgroove features.[110] Lastly, the ability for ECs to coalesce and organize into vascular tubes and networks is imperative. Some have found that anisotropic topography can encourage clustering of endothelial cells and development of tube-like structures when compared to isotropic scaffolds.[130,131] One study found a synergistic effect between 1.8 μm convex lens geometries and VEGF-enriched medium for enhancing differentiation of hMSCs

into ECs and promoting higher capillary density on explanted Matrigel plugs when compared to cells on unpatterned substrates.[132] Another study screened the impact of directional polydimethylsiloxane (PDMS) topographical gradients on human pulmonary microvascular ECs and found that larger microscale topographies inhibited vascular network formation compared to submicron topographies, which allowed for the limited formation of unstable networks. They further noted that the adhesion characteristics of a substrate coating layer largely influenced the dynamics of vascular network formation on topographic surfaces; by utilizing an appropriate instructive layer, otherwise unstable vascular networks that formed on submicron topographies could be stabilized.[133]

Implications of micro- and nanotopography in CVD therapeutic strategies via endothelial cell modulation

Critical applications of EC-modulating surface topographies in CVD therapies include stent, vascular graft, and cardiac patch implantations, where proliferative, anti-inflammatory, and pro-angiogenic behaviors are paramount to tissue repair. Major causes of stent and small graft failure, such as thrombosis and intimal hyperplasia, result from inadequate reendothelialization and increased inflammatory response, leading to a lack of vascular patency after implantation.[108] These procedures are typically performed in areas of regional ischemia, highlighting the need for appropriate pro-angiogenic stimuli to aid in the creation of new vasculature. Therefore, the use of biophysical cues to repair a denuded endothelial lining after surgical intervention and promote vascular growth represents an important strategy for expediting cardiovascular repair.

With respect to preclinical investigations of stent surface modifications, micro-nanostructured biomimetic surface patterns yielded more rapid reendothelialization of drug-eluting stents at 30- and 90-days post-implantation compared to unpatterned stents.[134] Further, this stent modification improved drug release kinetics, opening up the potential for dual-therapeutic approaches targeting both ECs and immune response.[134] A study using a rabbit model of restenosis corroborated *in vitro* findings[122] and showed titanium surfaces with ~90 nm tube features favored EC growth over that of vascular smooth muscle cells.[135] An investigated of nanoridge stent patterning similarly yielded rapid reendothelization and reduced neointimal thickening compared to bare stents, affirming the reliability of topographic patterns to improve EC coverage.[136]

Numerous investigations have focused on understanding the impact of topographical guidance on outcomes after vascular graft implantation.[137–140] In experimental models of PAD where nonobese diabetic/severe combined immunodeficiency (NOD SCID) mice were subjected to hindlimb ischemia, iPSC-EC-seeded aligned collagen scaffolds demonstrated enhanced perfusion recovery after 2 weeks compared to cell injection, acellular aligned scaffolds, and cell-seeded control scaffolds and improved microvascular density after 28 days when compared to PBS and cell injections.[137] Subsequent *in vivo* studies delivering stromal-vascular-fraction-cell-seeded aligned collagen scaffolds also resulted in improved perfusion recovery in PAD rodent models.[138] Interestingly, the superiority of aligned scaffolds over isotropic scaffolds for improved vascularization may be context dependent. Wanjare *et al*. demonstrated in an immunocompromised rodent model of mild MI that iPSC-CM and iPSC-CM/iPSC-EC-seeded isotropic scaffolds displayed either equivalent or increased

arteriole density compared to cell seeded aligned scaffolds.[139] Subcutaneous implantation of cell-seeded scaffolds further indicated higher survival of ECs and enhanced pro-angiogenic effects in random scaffolds, while aligned scaffolds encouraged anisotropic vessels formation.[139] These results stress the importance of understanding the differential responses of CVD-relevant cell types to topographical cues and the differences between *in vivo* models: while random scaffolds have been previously shown to have deleterious effects on transplanted cardiomyocyte function,[51] improved pro-angiogenic outcomes in ECs were observed here.[139]

Another approach attempted to utilize both physiologically relevant tubular molding and luminal surface micropatterning to impart optimal mechanical guidance of vascular cells after graft implantation. After infrarenal aortic implantation, 2 μm grating micropatterns had improved vascular patency after 20 days compared to unpatterned, pillar, convex, and concave micropatterns, and also demonstrated successful EC attachment to the luminal surface.[140] Additional studies have explored the use of patterned features to promote the formation of functional vasculature.[141–144] Human embryonic stem cell-derived cell (hESC)-EC-seeded microfluidic channel networks within hESC-EC-seeded collagen gel matrices showed high integration with coronary vasculature, enhanced vascular density, and comparable perfusion velocities to that of healthy myocardium when implanted into infarcted rat hearts.[141] Another strategy utilized aligned cords of EC and stromal cell populations formed via culture on microgroove substrates and subsequently encapsulated in a fibrin hydrogel to form a cardiac patch.[142] Following supra-epicardial transplantation onto an uninjured rat heart, the patches demonstrated perfusion 3 days post-transplantation and formed capillary- to

arteriole-sized microvessels at 7 days. A loss of patterning in newly formed vessels was observed between day 3 and 7, likely due to remodeling of the patch by local inflammatory response, but successful engraftment of cardiomyocytes, stromal cells, and ECs was still observed.[142] The advantages of delivering endothelial cells via material scaffolds were further highlighted when induced vascular progenitor cells (iVPCs) seeded on micro-bundle scaffolds showed higher survival and engraftment on myocardium compared to free iVPCs. Moreover, improved cardiac outcomes (LVEF, end systolic volume, fractional shortening), reduced infarct size, and increased vascularization in in rat models of MI, were also observed in iVPC-seeded scaffolds when compared to untreated control.[143] Another study demonstrated that circumferentially oriented fibrous grafts achieved complete endothelization, with cell alignment along the direction of blood flow achieved at 4 weeks. Additionally, formation of new capillaries was also observed during all time points over the 12 weeks.[144]

It has also been demonstrated that topography-mediated effects on tight-junction expression and cell morphology is maintained during successive passages, despite the removal of topographic cues after seeding.[145] An interesting avenue to explore is leveraging the memory of topographic modulation in ECs to improve regeneration *in-situ* without continuously providing such cues. Taken together, these findings indicate unique roles of biophysical cues on substrata to modulate EC behaviors including survival, proliferation, and vascularization and directly links these effects to improved cardiovascular outcomes.

1.3. Conclusion & Perspective

It is evident that micro- and nanoscale biophysical cues can effectively modulate the phenotype and function of cell types involved in CVDs. These features draw inspiration from native tissue architectures that continuously exert diverse mechanical cues to resident cells to maintain homeostatic behavior. Considering abnormal physical cues in the microenvironment can exacerbate CVD progression, strategies that introduce features that elicit native cell behaviors to impede CVD processes represent an exciting therapeutic direction to pursue.

A critical objective of materials-based therapeutic strategies is the identification of "optimal" feature geometries and dimensions for eliciting specific phenotypes. However, there are varied findings in the literature. Factors that are likely contributing to these differences include: (1) Reports have shown distinct cellular responses to physical cues depending on the nature of cells utilized, highlighting the potential of varying cell-sensitivities to mechanical cues.[113,146] Characteristics such as cell species, primary vs. cell lines, tissue source, cell heterogeneity, and cell maturity may account for the variability observed. Heterogeneous hiPSC-CM populations that can comprise of mixed nodal-, atrial-, or ventricular-like cell populations[147], each with distinct expression and electrophysiological profiles, may lead to inaccurate evaluations of topography-induced cardiomyocyte maturation and function. Further, immature cardiomyocytes have unique morphological and expression profiles compared to differentiated myocytes, such as Cx43 polarization[42,43] which directly impact functional outputs, and so can also contribute to differences observed across studies. (2) Both substrate surface chemistry and mechanical properties contribute to how physical cues are perceived and

interpreted by cells. Recent efforts have shown how material characteristics such as material functionalization[148], mechanical properties[149], degradation behavior[150], pore size[151], and thickness[152] can affect performance of therapeutic strategies. Hyaluronan-functionalized grafts promoted higher circumferential orientation of contractile α-SMA$^+$ cells than that of non-coated grafts *in vivo*.[148] Further, hydrophilicity has been found to have synergistic effects with topography on cell modulation.[125,153,154] Cell phenotypes are also heavily dictated by the elastic modulus of their microenvironment. For example, smaller diameter fibrous scaffolds correspondingly have lower stiffness which afford cells higher contractile ability against the fibers, highlighting a need to understand how stiffness and topography individually exert their roles on cell function.[50,54] (3) Ensuring that micro- and nanofabrication techniques are robust and precise enough to yield feature uniformity are vital to maximizing reproducibility in the field of therapeutic materials; failure to ensure this may lead to inability to replicate cell phenotypes and behaviors previously observed in other studies.[155] Since it is apparent that cells exhibit unique behaviors when exposed to specific size regimes[82,96,112,156], rigorous characterization, assessment, and comparison of geometry dimensions to other studies will be of great importance. (4) The environmental context of cell culture and exposure to the biophysical cues may be very different across studies. Parameters such as 2D versus 3D culture environments and whether cells were non-stimulated, pre-stimulated, or co-stimulated with soluble factors during exposure to biophysical cues all may have profound impacts on topography-induced modulation of cells. When cultured in a 2D monolayer, HUVEC and ECFC morphology and phenotypes were very similar; however, while in 3D cultures, there were stark differences in the behaviors of these cells.[119] (5)

The length and timescale after which the effects of physical cues are examined are crucial to note. Cell culture periods with topographies and subsequent timing of morphological, behavioral, expression, and functional analysis should accurately reflect the timescales during which these changes are expected to be taking place. Cell gene, protein, and secretion profiles are likely to vary over time and therefore attention to how topography-induced cell modulation may be temporally dependent demands attention.

Regulatory pathways are an additional challenge facing the utilization of combined biomaterial-engineered and stem cell technologies as viable regenerative therapies. Devices, drugs, and biological products are all governed by different regulations within the United States. Therefore, biologic/device combination products such as stem-cell/biomaterial strategies require special regulatory consideration to ensure that both constituent parts and the combination product are found to have sufficient quality, safety, and efficacy. The FDA's Office of Combination Products (OCP) is responsible for assigning a primary Agency center that will take the lead for the review and regulation of a specified combination product.[157,158] Assignment of the product's lead center (i.e., Center for Devices and Radiological Health, Center for Biologics Evaluation and Research, Center for Drug Evaluation and Research) is determined based on the evaluation of which constituent serves the primary mode of action (PMOA) of the final combination product. The PMOA is defined as "the single mode of action of a combination product that provides the most important therapeutic action of the combination product".[159] As appropriate, the lead center may often collaborate with other agencies to evaluate the information provided for regulatory submission.[157–159]. Given the sheer breadth of possible combination products and that

devices and biologics are typically developed and manufactured in accordance with different regulations, it is understandable that there is no gold-standard development approach and regulatory guidance that can be accurately applied to all combination products. Hence, existing guidance needs to be adapted to fully address the regulatory demands of each unique combination product. While biomaterial-engineered stem cell strategies may require significant regulatory considerations, several innovative programs such as the Breakthrough Therapy and Regenerative Medicine Advanced Therapy designation in the United States, the PRIME initiative in EU, and the Sakigake designation in Japan are being developed to enable patient access to experimental regenerative medicines.[160–162] Finally, any cell-based strategy must consider the issues of accessibility and affordability for widescale clinical translation.

While there still remains much to be explored regarding the intricacies of how cardiovascular cells respond to biophysical cues and how these responses may be leveraged for treating CVDs, this chapter provides a broad landscape of the efforts made in the field to date. Recent work has showcased a diverse array of geometries, materials, and size regimes for modulating cardiovascular cells both *in vitro* and in preclinical models of CVDs. In addition to being strong cell mediators on their own, topographies can work synergistically with additional cues such as electrical stimulation, mechanical stimulation, and stiffness to further regulate cell function. The versatility of these materials-based therapeutic strategy cannot be understated— micro- and nanofabrication techniques afford compatibility with a plethora of substrate materials, functionalization strategies, mechanical properties, feature geometries, and size regimes which may be tailored as needed. With these highly modular fabrication

capabilities, a fascinating direction for this strategy could be creating biophysical features based on specific patient and disease contexts as a more “personalized medicine” approach. However, first, optimization of all of the above parameters in addition to delivery and administration will need to be determined. Despite the long road ahead to effective translation of these strategies to the clinic, recent work at the intersection of materials, regenerative medicine, and cardiovascular research has demonstrated that biophysical cues have tremendous implications for cardiovascular disease therapy.

Chapter 2 – Hyaluronic acid microrods act as biophysical cues to regulate fibroblast phenotype and improve cardiac function after myocardial infarction

2.1. Introduction

The ability to successfully repair and regenerate injured cardiac tissue after myocardial infarction (MI) has remained a significant challenge for tissue engineering and regenerative medicine therapies. After MI, pathological remodeling leads to the formation of stiff scar tissue that critically impairs contractility mechanisms, cell engraftment and survival, and the flow of oxygen and nutrients to the myocardium.[163,164] Current treatments of this rampant fibrotic cascade often rely on systemic inhibition of pathological cytokines and chemokines; however, this indiscriminate approach may yield increased adverse events.[165,166] Therefore, ideal approaches would inhibit myocardial fibrosis to enable repopulation of functional cardiac cells and enhance the efficacy of cellular replacement/recruitment strategies. Successful modulation of the post-infarct microenvironment to one that encourages cardiac tissue regeneration holds great promise in enhancing our clinical capabilities in treating patients suffering from MI and preventing subsequent progression heart failure.

It is known that key cell types in the heart, including cardiomyocytes, fibroblasts, and endothelial cells, are mechanosensitive and therefore, their behaviors are heavily influenced by physical cues sensed in their microenvironment.[19,167] In native cardiac tissue, the extracellular matrix (ECM) consists of various fibrillar and laminar components including linear bundles of collagen and pores in vascular membrane basement membranes with features that span both the nano- and micron scale.[21–23]

Cells can detect these external stimuli via integrins, surface receptors, and ion channels. These cues are then transformed into signals that trigger the activation of intracellular pathways which lead to changes in transcriptional processes and cell behaviors (i.e., adhesion, morphology, phenotype).[19,167–170] Recent work has attempted to leverage these cell-substrate interactions to encourage more healthy cell behaviors in pathological cells to mitigate damage and enhance regeneration post-MI. Our lab has extensively investigated the effect of micron scale topographic features (i.e., polydimethylsiloxane (PDMS) micropegs, polypropylene microfibers, polyethylene glycol (PEG) microrods) on fibroblast transcriptional expression to determine if myofibroblast transition could be prevented.[89,171,172] Fibroblasts are able to attach to these features via focal adhesions which anchor the cells, resulting in notable differences in behaviors including proliferation, myofibroblast markers, and ECM protein expression. [89,171,172] Injection of PEG microrods in rodent models of ischemia-reperfusion (I/R) MI also demonstrated improved ejection fraction (EF), locally decreased collagen deposition, and demonstrated trends in improved revascularization.[89]

Biodegradable and tunable platforms are extremely desirable as clinically relevant, biomaterials-based strategies. As such, hyaluronic acid (HA) has become a promising candidate for use with the microrod technology. HA is a naturally occurring polysaccharide that is involved in several biological processes related to wound healing (i.e., regulation of inflammation, cell proliferation, cell migration, and angiogenesis).[173–175] Moreover, it is biocompatible, exhibits biological degradation, can have tunable stiffness, and is compatible with UV photolithography. Both high and low molecular weight HA have been shown to have distinct biological effects: high molecular weight

HA is anti-inflammatory whereas smaller fragments generated via HA degradation increase cell migration and angiogenesis.[176,177] By crosslinking HA polymer, microrods made of HA may leverage the qualities of high molecular weight HA and mitigate the initial inflammatory response after MI, while later encouraging repopulation of the post-infarct myocardium as the microrods degrade via hyaluronidases and oxidative stress.[177,178]

This chapter discusses the fabrication and evaluation of HA microrods for the treatment of cardiac fibrosis after MI. We show that microrods made of HA can be reliably fabricated with the desired dimensions using UV photolithography fabrication methods. HA microrods were also able to reduce expression of myofibroblast markers in both 2D and TGF-β1-stimulated 3D cell cultures and improve cardiac function after 6 weeks in rodents with I/R MI injury.

2.2. Materials and Methods

2.2.1. Materials

Sodium hyaluronate (100kDa) was obtained from Lifecore Biomedical (Chaska, MN) and stored at -20°C until use. Dimethylformamide (DMF), glycidyl methacrylate (GM), triethylamine (TEA), and 2-hydroxy-4′-(2-hydroxyethoxy)-2-methylpropiophenone (#410896) were purchased from Sigma-Aldrich (St. Louis, MO) and used as received. Spectrum™ Spectra/Por™ 3 RC dialysis membrane tubing, 3500 Dalton MWCO (#08-670-5B), deuterium oxide (#M1034280009), 4'-(aminomethyl)fluorescein, and CD44 monoclonal antibody (#MA4405) were purchased from Thermo Fisher Scientific (Waltham, MA). High concentration (HC) growth factor reduced (GFR) Matrigel

(#354263) and Cell Recovery Solution (#CB40253) was obtained from Corning (Corning, NY). Recombinant human TGF-β1 (#100-21) was obtained from PeproTech (Rocky Hill, NJ).

2.2.2. Synthesis of hyaluronic acid methacrylate

Hyaluronic acid methacrylate (HAMA) was synthesized based on a protocol adapted from Bencherif *et al*.[179] These methods have been previously reported by our lab.[88] Briefly, one gram of sodium hyaluronate (100 kDa) was dissolved at 3.76 mg/mL in a 1:1 solution of deionized (DI) water:DMF (266 mL). After solubilizing, a 73-fold molar excess of GM (24.86 mL, 0.1822 mol) and 26.5-fold molar excess of TEA (9.235 mL, 0.066 mol) with respect to the primary hydroxyl/hydroxymethyl functional group on hyaluronic acid was added to the mixture. The reaction was left to stir for 24 hours at ambient temperature while protected from light. HA and HAMA products were recovered via precipitation in an excess of isopropanol. Briefly, 35 mL of isopropanol was added to 15 mL of reaction solution and then the precipitate was isolated by centrifugation at 1275 × g for 5 min. This process was repeated until all of the reaction solution had been precipitated. The recovered precipitate was subsequently dissolved in 90 mL of DI water. The resulting solution was then dialyzed (3500 Dalton MWCO) against DI water (10 times volume of the solution) for 48 hours with three changes of water. The product was then lyophilized for 3−4 days at −40°C and 65 mTorr and the resulting white powder was then stored at −20°C until further use. ^{1}H NMR spectroscopy (Bruker Avance III HD 400 NMR) was used to determine the degree of methacrylation. Methacrylate peaks are observed at ~6.5, ~5.6, and ~1.85 ppm. Degree of

methacrylation was calculated based on the ratio of the relative peak integration of the methacrylate peak at 1.85 ppm and HA's acetamide peak which occurs at 1.9 ppm.

2.2.3. Hyaluronic acid microrod fabrication

HAMA was dissolved at the desired concentration (either 75 or 100 mg/mL) in DI water containing 0.5% w/v of the photoinitiator 2-hydroxy-4′-(2-hydroxyethoxy)-2-methylpropiophenone. The solution was stirred for 2 hours at ambient temperature to facilitate solubilization and protected from light. After, the solution was centrifuged at 15000 × g for 5 minutes to remove any impurities. Subsequently, a 15 μm layer of precursor solution was deposited onto a piranha-treated 3" silicon wafer. The wafer was then patterned using a Karl Suss MJB3 mask aligner by exposing the wafer through a photomask (15 μm × 100 μm features) to a 365 nm UV light source. Crosslinked microrods were then gently removed from the wafer using a cell scraper and collected into DI water, where any uncrosslinked HAMA would fully dissolve. Microrods were then passed through a 150 μm mesh filter to remove any aggregates and then concentrated by centrifugation. The microrods were subsequently sterilized with 70% ethanol for 30 minutes and then resuspended in either saline or cell culture medium prior to use. Microrod concentration was determined using a hemocytometer. To visualize 3D geometry, HA microrods were labeled with 4′-(aminomethyl)fluorescein (Thermo Fisher, Waltham, MA) through EDC/NHS coupling and imaged using confocal microscopy.

2.2.4. Cell culture and qPCR

NIH 3T3 mouse fibroblasts (ATCC, Manassas, Virginia) were cultured in Dulbecco's modified Eagle's medium with 10% fetal bovine serum and 1% penicillin/streptomycin. To investigate the effect of HA microrods on fibroblast

phenotype in 2D culture, cells were cultured with HA microrods (100 mg/mL) at a high ratio (1:5 microrods per cell) or a low ratio (1:20 microrods per cell). For 2D culture, the desired amount of HA microrods were first deposited onto the bottom of cell culture wells, followed by the addition of 3T3 fibroblasts at a seeding density of 10,000 cells/cm^2. To investigate the role of CD44 in the mechanism of how HA microrods modulate fibroblast phenotype, a final concentration of 12 μg/mL of CD44 monoclonal antibody (Thermo Fisher, Waltham, MA) was added to both untreated and HA microrod-treated wells.

For experiments using 3D culture, cells were mixed with either media or microrods (1:5 or 1:2 microrods per cell) and added to liquid state HC GFR Matrigel (Corning, Corning, NY) using a coating density of 100 μL/cm^2 Matrigel and a final concentration of 4 mg/mL. Cells were added using a seeding density of 30,000 cells/cm^2. The combined mixture was then seeded into ~2 mm thick cultures in a 24-well plate before being allowed to gel at 37°C. After gelation, regular media or media dosed with 2.5 ng/mL of TGF-β1 was added to each well. For example, if a 24 well plate was used with a growth surface area of 1.9 cm^2, 190 μL of 10 mg/mL HC GFR Matrigel would be used. To this, 286 μL of combined cell and microrod volume would be added. This was split into equal portions as follows: 143 μL of 57,000 cells to achieve the desired seeding density described above and 143 μL of the desired microrod amount per the ratio used. These parameters allowed for optimal distribution and interaction of cells and microrods in a 3D space.

Genetic material was harvested using the RNEasy Mini Kit (Qiagen, Hilden, Germany). For 3D cultures, Cell Recovery Solution (Corning, Corning, NY) was first used to extract cells prior to harvesting genetic material. RNA was converted into cDNA using the iScript cDNA synthesis kit (Bio-Rad Laboratories, Hercules, CA) and a Viia7 qPCR machine (Life Technologies, Carlsbad, CA) was used to measure relative expression levels of gene targets compared to the housekeeping gene 60S ribosomal protein L19 (RPL19). Expression levels of all genes were evaluated using the Fast SYBR Green Mastermix (Life Technologies, Grand Island, NY) and custom DNA primers (Integrated DNA Technologies, Coralville, IA) in triplicate for three biological replicates (Table 2.1).

2.2.5. Infarct model and microrod injections

The animal protocol for induction of MI was approved by the Committee for Animal Research of the University of California, San Francisco and was performed in accordance with the recommendations of the American Association for Accreditation of Laboratory Animal Care. The I/R MI model used in this study has been extensively tested in our labs.[88,89,180] To produce the I/R MI model, female Sprague-Dawley rats (180–220g) underwent occlusion of the left anterior descending coronary artery for 30 minutes, followed by reperfusion while under general anesthesia. General anesthesia was achieved by inhalation of 2% L/min isoflurane.[180] The chest was then sutured to close, and the animal was allowed to recover. Two days after MI, the rats were randomized into treatment groups– saline-injected, HA solution-injected, or microrod-injected. To administer the treatment, animals were given one intramuscular injection into the heart wall under blinded conditions via ultrasound guided transthoracic injection

using a 29-gauge syringe.[180] Injections consisted of either 50 μL of sterile 0.9% sodium chloride solution (n = 7), HA dissolved in sodium chloride solution at 4.2 mg/mL (n = 9), or 50,000 microrods (75 mg/mL) in sodium chloride solution (n = 7). Each injection was delivered to the center of the infarct region as visualized by hyperechoic signal on ultrasound. Successful injection was confirmed by a local increase in ultrasound signal near the tip of the syringe and brief thickening of the left ventricle (LV) wall.

2.2.6. Echocardiography

Transthoracic echocardiography was performed with a 15-MHz linear array transducer system (Sequoia c256, Acuson, Erlangen, Germany) on all animals under 2% L/min isoflurane. Echocardiography was performed prior to injection on Day 2 post-MI, and prior to sacrifice after 6 weeks post-MI. To determine EF at Day 2 and 6 weeks, the ventricular shadow was outlined in both systole and diastole and the single plane area length algorithmic method was applied. Two-dimensional images were obtained in both parasternal long- and short-axis views at the papillary muscle level. Change in EF was calculated as $\Delta EF = EF_{6\ weeks} - EF_{Day\ 2}$. Transverse images were obtained at three levels: basal (at the tip of the mitral valve leaflets), middle (at the papillary muscle level), and apical (distal to papillary muscle but before the cap of the cavity). All image analyses were performed in a blinded fashion. Animal hearts were excluded from echocardiographic analyses in cases where the ventricular shadow was not clearly identifiable in the Day 2 or 6-week image. Additionally, cases where the calculated ejection fraction was above 50% at Day 2 post-MI were excluded because they indicated an insufficient infarct model.

2.2.7. Histology

Sacrifice was performed after 6 weeks by maintaining the animal at 5% L/min isoflurane for five minutes, followed by bilateral thoracotomy and injection of potassium chloride into the right atrium to arrest the heart in diastole. The heart was then extracted and frozen in OCT (Sakura Finetech USA, Inc., Torrance, CA) on 2-methylbutane (Sigma Aldrich, St. Louis, MO) on dry ice. Tissue blocks were cryo-sectioned at a thickness of 10 μm starting at the apex of the left ventricle, collecting 10 serial sections every 350 μm until 100 sections were collected. Tissue sections were stained with H&E, Masson's trichrome, and Picrosirius red stains using standard protocols.

2.2.8. Image Analysis

For whole heart histology (H&E, Masson's trichrome, Picrosirius red), images were taken using a Nikon 6D optical microscope (NIKON Instruments, Inc., Melville, NY). All quantifications were performed using Nikon Elements software. For wall thickness analysis, the 5 measurements for minimum length were taken across the infarct area of each tissue section. The absolute minimum length measured across all available sections in each heart sample was selected as the minimum wall thickness. For collagen analysis, five sections of each heart were selected from throughout the coronal plane of the infarct zone and stained with Picrosirius red to assess the area and density of collagen in the infarcted hearts. These sections were imaged under brightfield as well as under polarized light to visualize the collagen fibers. Infarct area was quantified and normalized to total area of the LV free wall.

2.2.9. Statistical Analysis

All data are presented as the mean ± standard deviation unless otherwise indicated. *In vitro* and *in vivo* analysis were performed using a one-way analysis of variance (ANOVA), followed by multiple comparison by Holm-Sidak correction to identify differences between groups.

2.3. Results

2.3.1. Effect of HA microrods on fibroblast phenotype in 2D and 3D in vitro culture

To generate HA microrods via a UV photolithography fabrication method, we modified protocols that were previously used to functionalize HA polymer with photosensitive methacrylate handles.[179] ^{1}H NMR spectroscopy was used to confirm the successful modification of the HA polymer backbone with methacrylate groups. Methacrylate peaks are observed at ~6.1, ~5.6, and ~1.85 ppm (Figure 2.1A). To evaluate the reproducibility of the synthesis and degree of methacrylate substitution, the integrations of the methacrylate peak at 1.85 ppm was compared to that of the acetamide peak in HA at 1.9 ppm across four separate batches of HAMA.[179] We found that the protocol developed for synthesizing HAMA is reasonably reproducible with a 50.1 ± 6.9% substitution (Figure 2.1B).

The stiffness of both 75 mg/mL and 100 mg/mL HAMA concentrations that were used to fabricate HA microrods have been reported to be 70 kPa and 160 kPa, respectively.[88] HA microrods were fabricated via photolithography using a Karl Suss MJB3 mask aligner following the method illustrated in Figure 2.2A. Both fluorescence

microscopy and differential interference contrast (DIC) imaging confirm the dimensions of the 15 x 15 x 100 μm HA microrods (Figures 2.1B-C).

To investigate the effect of HA microrods on fibroblast phenotype, NIH 3T3s were cultured with varying amounts of HA microrods and then evaluated for changes in gene expression. Notably, fibroblasts experienced a dose-dependent decrease in gene expression of markers indicative of the myofibroblast phenotype, including alpha smooth muscle actin (ACTA2) and type I collagen (COL1A2) when cultured with ratios of 1:20 and 1:5 HA microrods:cells. When cultured with a 1:5 ratio HA microrods:cells, ACTA2 and COL1A2 expression were significantly reduced to 0.01 ± 0.002 fold expression and 0.15 ± 0.08 fold expression relative to cells grown without microrods, respectively (Figure 2.3A, $p < 0.001$). While the 1:20 ratio HA microrods:cells displayed a dampened reduction in ACTA2 and COL1A2 expression, the results were still significant compared to untreated controls where ACTA2 expression was decreased to 0.09 ± 0.02 fold expression and COL1A2 expression was decreased to 0.31 ± 0.04 fold expression relative to cells grown without microrods (Figure 2.3A, $p < 0.001$). Further, the effect of HA microrods on fibroblast phenotype was also observed in markers of the TGF-β signaling cascade, including TGFB1 and SMAD3 where expression was reduced to 0.34 ± 0.04 fold expression and 0.25 ± 0.01 fold expression relative to cells grown without microrods (Figure 2.3B, $p < 0.05$). These gene expression data suggest that HA microrods encourage less myofibroblast-like phenotypes by exerting its action on the TGFβ-signaling pathway.

To ascertain whether the ability for HA microrods to modulate fibrotic phenotype is maintained in more physiologically relevant 3D environments as well as in pro-fibrotic wound healing environments where TGF-β1 is present, we developed an optimized culture system that maximizes interactions between HA microrods and cells in 3D space while allowing for sufficient distribution throughout the culture environment (Figure 2.4A-B). When cultured at a high ratio of 1:2 ratio HA microrods:cells, decreased gene expression is observed in for ACTA2, COL1A2, TGFB1, and MMP2 (p = 0.08, 0.09, 0.07, and 0.06, respectively). This indicates that the capacity for HA microrods to exert their topographical influence over fibroblast phenotype is preserved in 3D environments, albeit to a lesser degree than what is observed in 2D culture systems (Figure 2.5A). Similarly, HA microrods also maintain their capability to modulate the expression of fibrotic markers in 3D culture environments stimulated with 2.5 ng/mL TGF-β1 (Figure 2.5B, p = 0.04). Overall, these data indicate the potential for HA microrods to serve as a promising therapeutic strategy aimed at mitigating rampant fibrotic response in post-infarct myocardium.

While it is thought that stiffness and topographical cues are primarily transduced by integrins, many physiological processes with HA are mediated by HA specific receptors. Of these, CD44, RHAMM, and ICAM-1 are the best characterized.[181] HA binding to these receptors triggers a signaling cascade that elicits cytoskeletal remodeling and leads to events such as cellular adhesion and cell trafficking. Specifically, HA-CD44 binding is heavily involved in mediating cell-cell and cell-matrix adhesions and signal transduction through interactions with ERM proteins, which crosslink actin filaments, and ankyrin, a membrane cytoskeletal component.[182]

Therefore, it is interesting to investigate whether HA ligand-receptor interactions play a role in fibroblast engagement with HAMRs and subsequent observed downregulation of the fibrotic phenotype. To probe the impact of CD44 blockade on the ability of HA microrods to modulate fibrotic phenotype, NIH 3T3 fibroblasts were co-cultured with HA microrods and a CD44 blocking antibody in 2D culture. Interestingly, results show that when CD44 on fibroblasts is less able to engage with HA microrods due to the presence of the antibody, there is still a downregulation of ACTA2 and COL1A2 expression, though not as pronounced as what we've previously observed in 2D environments (Figure 2.6A). This indicates that CD44 is not a key player in how fibroblasts sense and interpret HA microrods to achieve downregulation of the myofibroblast phenotype . We then performed immunofluorescence staining of NIH 3T3 fibroblasts that were cultured with HA microrods. Despite having significant binding interactions with HA, CD44 was found to distributed throughout the fibroblast membrane and did not appear to be localized to the surface of the HA microrod (Figure 2.6B). This also corroborates what the gene expression data showed and points to other binding mechanisms, such as integrin-binding, as being the primary mechanisms for cell interaction with HA microrods.

2.3.2. Effect of hyaluronic acid microrods in ischemia-reperfusion myocardial infarction in vivo models

MI was induced followed by reperfusion to generate a chronic heart failure model. Two days after MI, echocardiography was performed to obtain baseline EF measurements. Immediately after, injections consisting of either saline, HA solution, or

HA microrods were administered directly into the infarct zone via ultrasound-guided, intramyocardial injection. To generate an appropriate material control, total mass of HA was kept equivalent between HA solution and HA microrod injections. After six weeks, echocardiography was performed to obtain end-point EF measurements. Rats were then sacrificed, and their hearts were harvested for subsequent histological analyses. Tissue sections were then stained with H&E, Masson's trichrome, and Picrosirius red to evaluate HA microrod treatment efficacy on mitigating fibrotic response, when compared to vehicle (saline) and material control (HA solution). H&E and Masson's trichrome staining of heart tissue cryosections are provided in Figure 2.7A.

Cardiac performance was assessed as calculated by the change in EF, the difference in EF measured right before injection (Day 2) and right before sacrifice (6 weeks). Rats treated with HA microrods exhibit marked improvement in EF (5.91% ± 3.67%) compared to HA solution (−0.36% ± 4.20%, $p < 0.05$) and saline controls (−8.22% ± 7.28%, $p < 0.001$) (Figure 2.7B). Of note, animals treated with HA solution also showed better cardiac function compared to saline after 6 weeks post-MI ($p < 0.01$). This suggests that there may be some cardioprotective properties that are being bestowed by the biochemical properties of the HA material itself.

Wall thickness measurements were performed on sections throughout the heart where the LV cavity was able to be identified. Results show that rats treated with HA microrods had significantly greater minimum LV wall thickness (1.22 ± 0.38 mm) compared to saline treated hearts (0.70 ± 0.24 mm), which exhibited significant wall thinning ($p < 0.05$) (Figure 2.7C), and modest improvement over animals treated with

HA solution (1.03 ± 0.21 mm). Both brightfield and polarized images of Picrosirius red staining of heart tissue cryosections are provided in Figure 2.8A. Picrosirius red staining was used to quantify the extent of fibrosis in the infarcted hearts. Rats treated with HA microrods and HA solution seem to have less collagen deposition in the LV free wall compared to those treated with saline (Figure 2.8B, $p = 0.1$).

2.4. Discussion

Regenerative medicine strategies that focus on limiting scar tissue development after acute cardiac injury, while creating a hospitable microenvironment conducive to tissue repair would represent a crucial therapeutic innovation in cardiac therapies. While much of the current focus on therapies focused on delivering cells to replace injured myocardium, the success of these strategies is greatly hindered by poor engraftment and survival post transplantation.[17] Cardiac fibroblasts make up the largest population of cells in the heart and play critical roles in synthesis and degradation of ECM, cell-cell signaling between cardiomyocytes, and cytokine and growth factor secretion.[78] After MI, fibroblasts transform into their myofibroblast phenotype, which is characterized by increased ECM production, enhanced cytokine/chemokine secretion, and high contractility. This fibrotic response, if left unchecked, leads to maladaptive tissue stiffening, impaired cardiac contractility, and limited repopulation of functional cells.

Previous work has utilized HA in translational strategies such as injection of bulk HA polymer to stabilize and mechanically bolster the injured myocardium to improve cardiac outcomes after MI.[183–185] However, limitations of these strategies often involve the gelation kinetics of the crosslinking chemistries used to generate the HA hydrogel *in situ*. If the crosslinking occurs very quickly there is risk of gelation within the catheter

during administration of multiple injections. However, if the gelation occurs slowly, diffusion of uncrosslinked HA material into tissue may compromise the intended hydrogel mechanical properties, such as stiffness. The studies described here investigated the use of HA microrods for mitigating the myofibroblast phenotype to improve cardiac outcomes after myocardial infarction. Here, we report the ability to reliably synthesize HAMA and fabricate the HA microrods to achieve discrete 15 x 15 x 100 μm micropographical features (Figures 2.1 and 2.2). These features are already crosslinked prior to administration to avoid pitfalls of gelation kinetics of hydrogel materials post-injection and are compatible with catheter injection with minimal risk of clogging. Moreover, contrary to bulk polymer injections that minimize wall stress by bolstering the myocardium, HA microrods also provide discrete micromechanical cues to resident cells to modulate cell phenotypes.

There has been a growing push to leverage the mechanotransduction mechanisms of cells to dictate cellular phenotypes. Specifically for fibroblasts, there have been many reports using biophysical cues to modulate fibroblast behaviors such as morphology[90], adhesion[82], proliferation[83,84], and gene expression[88,89,171,172]. The formation of focal adhesions on substrate topography leads to the generation of cytoskeletal tension, which in turn affects cytoskeletal organization, remodeling of the nucleus, and transcriptional activity.[83,86,87] These interactions allow for material-based control of cellular behaviors of fibroblast populations to discourage myofibroblast phenotypes. Our lab has previously characterized the effect of microtopographic features using a variety of different materials and geometries on fibroblast behaviors.[89,171,172] Interestingly, HA microrods demonstrated the ability to more

significantly downregulate the expression of key markers of the fibrotic phenotype, such as alpha smooth muscle actin, TGF-β1 cascade members, and ECM components, compared to features of previously utilized, more bioinert materials (Figure 2.3).[88] Furthermore, attenuation of the myofibroblast phenotype was conserved in 3D and TGF-β1-stimulated environments (Figure 2.5).

Though exact mechanisms of HA microrod-fibroblast interactions were not investigated in our studies, we hypothesized that HA specific receptor CD44 may play a role in HA microrod regulation of fibroblast transcriptional activity. However, our results show that downregulation of fibrotic marker gene expression is still maintained despite CD44 blockade, albeit the effect is slightly lessened (Figure 2.6). This indicates that there are other mechanosensitive components that are responsible for HA microrod regulation of fibrotic genes in fibroblasts beyond CD44. It has been reported that chemical modification of the HA polymer backbone can impact binding to CD44.[186] Given the calculated degree of substitution being ~50%, it may follow that the binding interactions between CD44 and HA microrods may be negatively impacted. It is more likely that integrins are primarily responsible for transducing these supplied biophysical signals, however additional work will be necessary to confirm this hypothesis.

In line with observed *in vitro* results, treatment with HA microrods (5.91% ± 3.67%) in rodent models of I/R MI injury demonstrated improvements in cardiac performance and left ventricle wall thickness compared to those treated with material (−0.36% ± 4.20%) and vehicle (−8.22% ± 7.28%) controls as well as PEG microrods (−2.59% ± 8.11%) (Figure 2.7B).[89] Interestingly, HA solution had a beneficial effect in preventing further decline of EF 6 weeks after MI, likely due to the wound healing

properties HA. Evaluation of HA microrod treatment compared to HA solution treatment also indicates that geometry itself is an important factor in determining cardiac outcomes beyond the material itself. Further, some improvements in myocardial structure and cardiac fibrosis were observed in rats treated with HA microrods compared to those treated with HA solution and vehicle control (Figures 2.7C and Figure 2.8B). In addition to achieving desirable cardiac outcomes in *in vivo* models of MI, HA microrods represent an exciting technological development as they are inexpensive to product, scalable, injectable, and cell-free for facile translation of this strategy for clinical needs. The results described here show immense promise for HA microrods as a novel therapeutic strategy capable of reducing pathological scarring, enhancing tissue regeneration, and providing structural support to myocardium to minimize deleterious complications of MI.

Table 2.1. Primers used for qPCR.

Target Gene	Forward Primer (5' -> 3')	Reverse Primer (5' -> 3')
RPL19	CATTTTGCCCGACGAAAGGG	GATCTGCTGACGGGAGTTGG
ACTA2	GCTGCTCCAGCTATGTGTGA	CCATTCCAACCATTACTCCCTGA
COL1A2	AAGGGTGCTACTGGACTCCC	TTGTTACCGGATTCTCCTTTGG
TGFB1	GGACTCTCCACCTGCAAGAC	CTGGCGAGCCTTAGTTTGGA
TGFBR2	ACGTTCCCAAGTCGGA TGTG	TGTCGCAAGTGGACAGTCTC
SMAD3	AAGGCGACACATTGGGAGAG	GGGCAGCAAATTCCTGGTTG
MMP2	CAAGTTCCCCGGCGATGTC	TTCTGGTCAAGGTCACCTGTC

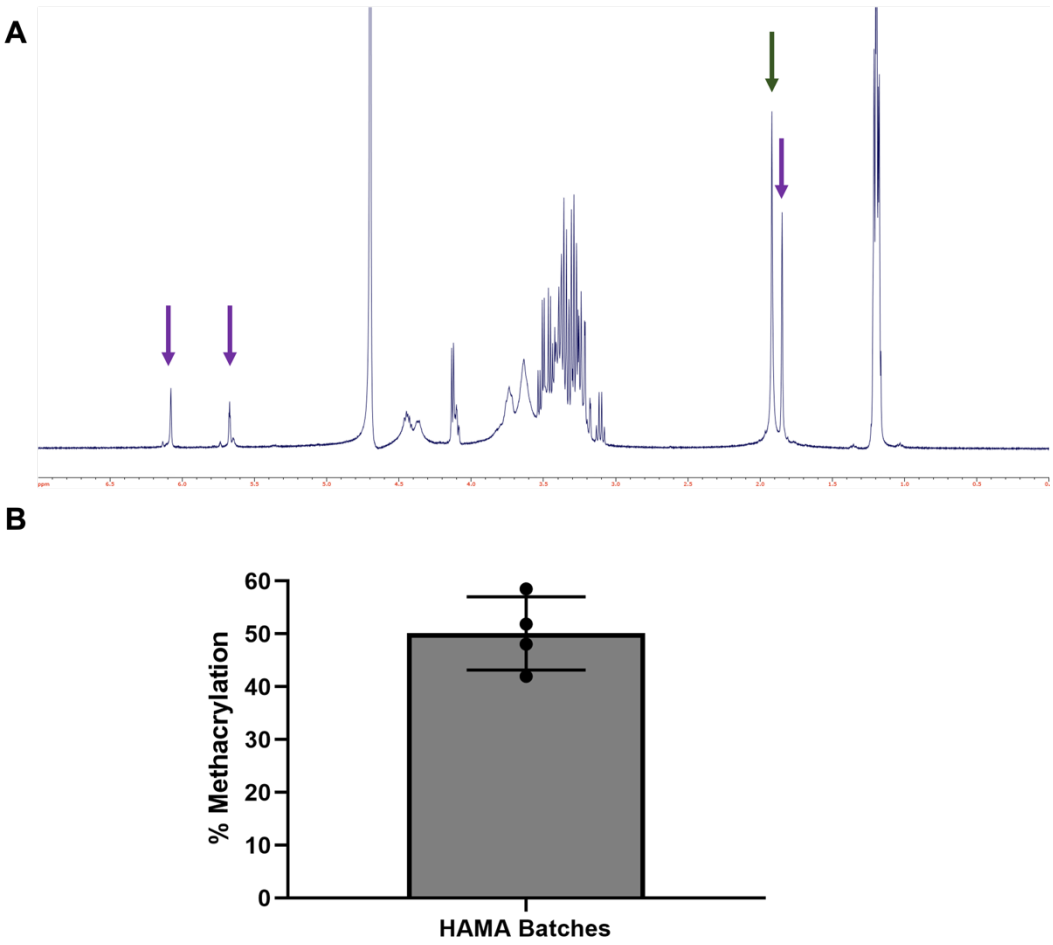

Figure 2.1. ^{1}H NMR spectra and characterization of hyaluronic acid methacrylate (HAMA). (A) Representative 1H NMR spectra of HAMA with methacrylate peaks at ~5.6 ppm, ~6.1 ppm, and ~1.85 ppm (purple arrows) and HA's acetamide peak is shown at 1.9 ppm (green arrow). The degree of substitution was calculated by comparing the peak integrations at 1.85 ppm and 1.9 ppm. (B) 1H NMR spectra were assessed to quantify the degree of HA methacrylation across four separate HAMA synthesis batches. The data are presented as the mean ± SD.

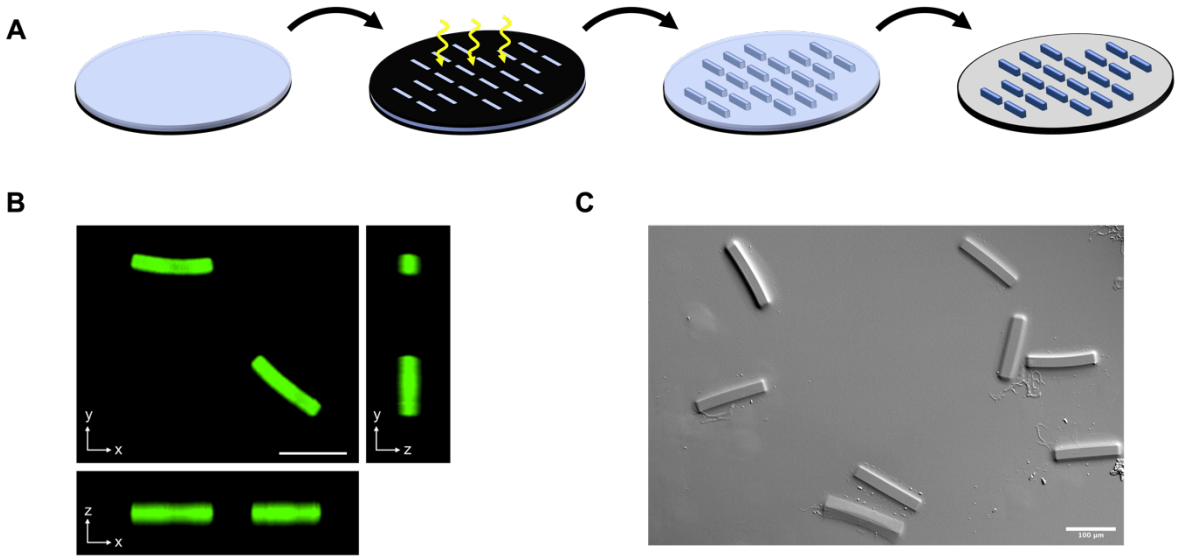

Figure 2.2. Hyaluronic acid microrod fabrication scheme and characterization of hyaluronic acid methacrylate. (A) Hyaluronic acid (HA) microrods were fabricated via exposure of a thin film (15 μm) of hyaluronic acid methacrylate to 365 nm UV light through a photomask with 15 μm x 100 μm features. HA microrods were subsequently developed and collected in water. (B) Fluorescein-labeled HA microrods exhibit the desired dimensions of 15 x 15 μm x 100 μm as illustrated via fluorescent microscopy. (C) DIC images of HA microrods also demonstrate appropriate dimensions. Scale bars = 100 μm. Adapted from Le *et al*., 2018.

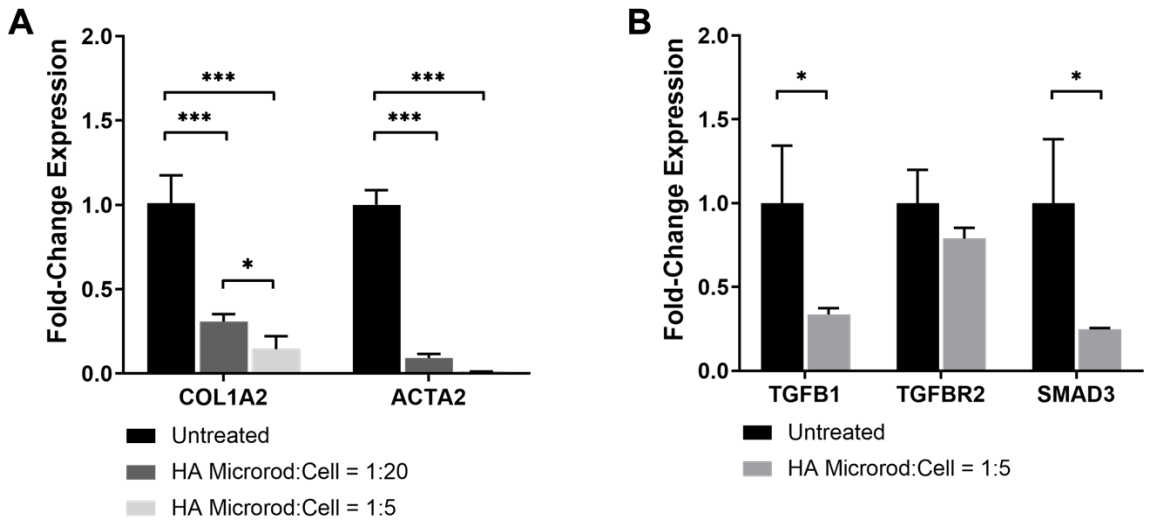

Figure 2.3. Hyaluronic acid microrods modulate fibroblast phenotype in 2D and 3D culture. (A) NIH 3T3 fibroblasts cultured with HA microrods demonstrate dose-dependent reduction in gene expression of pro-fibrotic markers including ACTA2 and COL1A2 when cultured at a density of 1 microrod per 5 and 20 cells. (B) Fibroblasts show a reduction in gene expression of TGFB1 and SMAD3 when cultured at a density of 1 microrod per 5 cells. The data are presented as the mean ± SD. *$p < 0.05$, **$p < 0.01$, ***$p < 0.001$. Adapted from Le *et al.*, 2018.

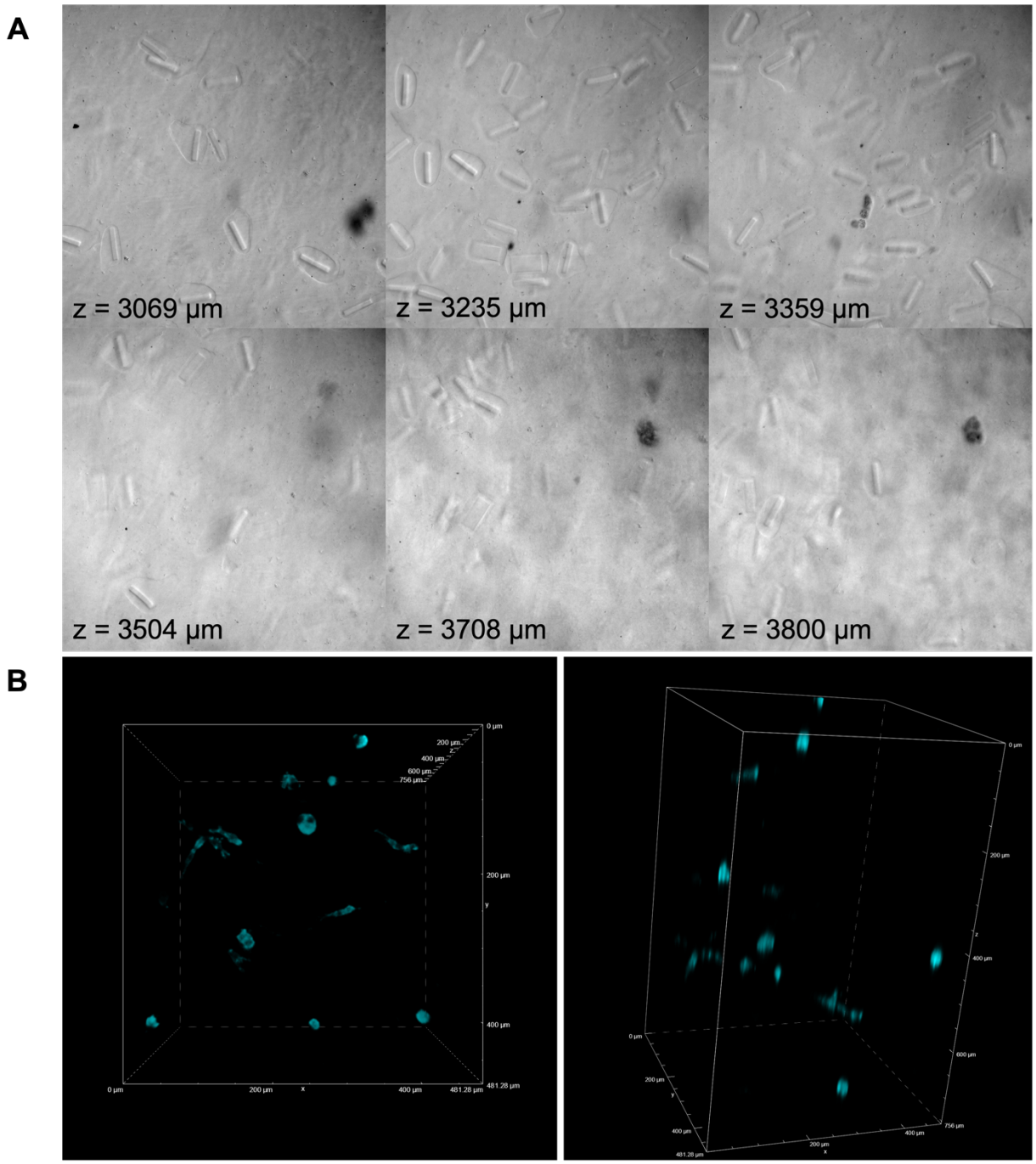

Figure 2.4. Hyaluronic acid microrod and fibroblast distribution in optimized 3D Matrigel culture conditions. Confocal microscopy was used to illustrate that (A) HA microrods and (B) NIH 3T3 fibroblasts show good distribution throughout the z-direction of the 3D Matrigel environment using the optimized culture protocol described. Fibroblasts are stained with DAPI to visualize their distribution.

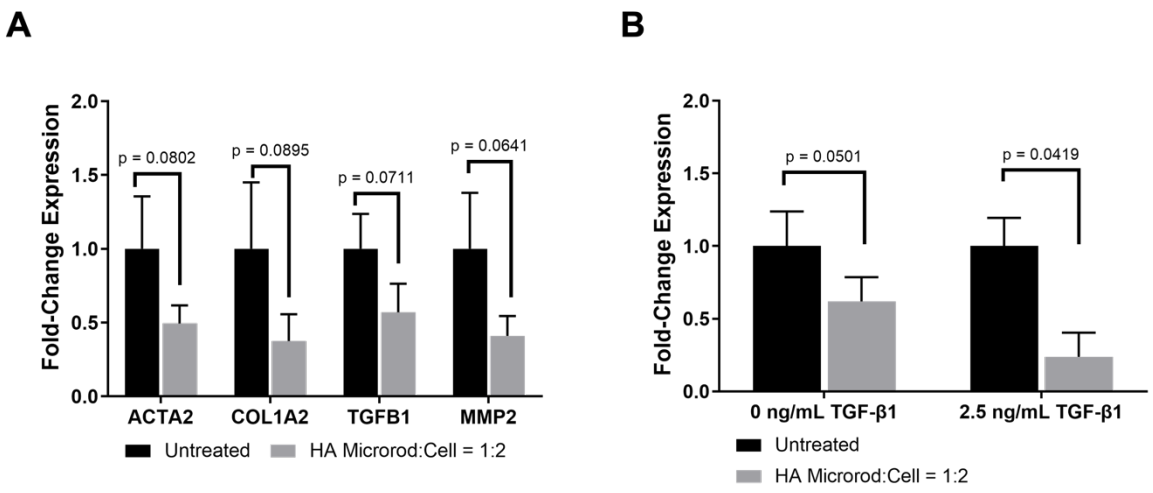

Figure 2.5. Hyaluronic acid microrods modulate fibroblast phenotype in 3D culture. The capacity for HA microrods to decrease gene expression of myofibroblast-like markers in NIH 3T3 fibroblasts is maintained in (A) 3D Matrigel culture and in (B) a TGF-β1-stimulated 3D Matrigel environment. The data are presented as the mean ± SD.

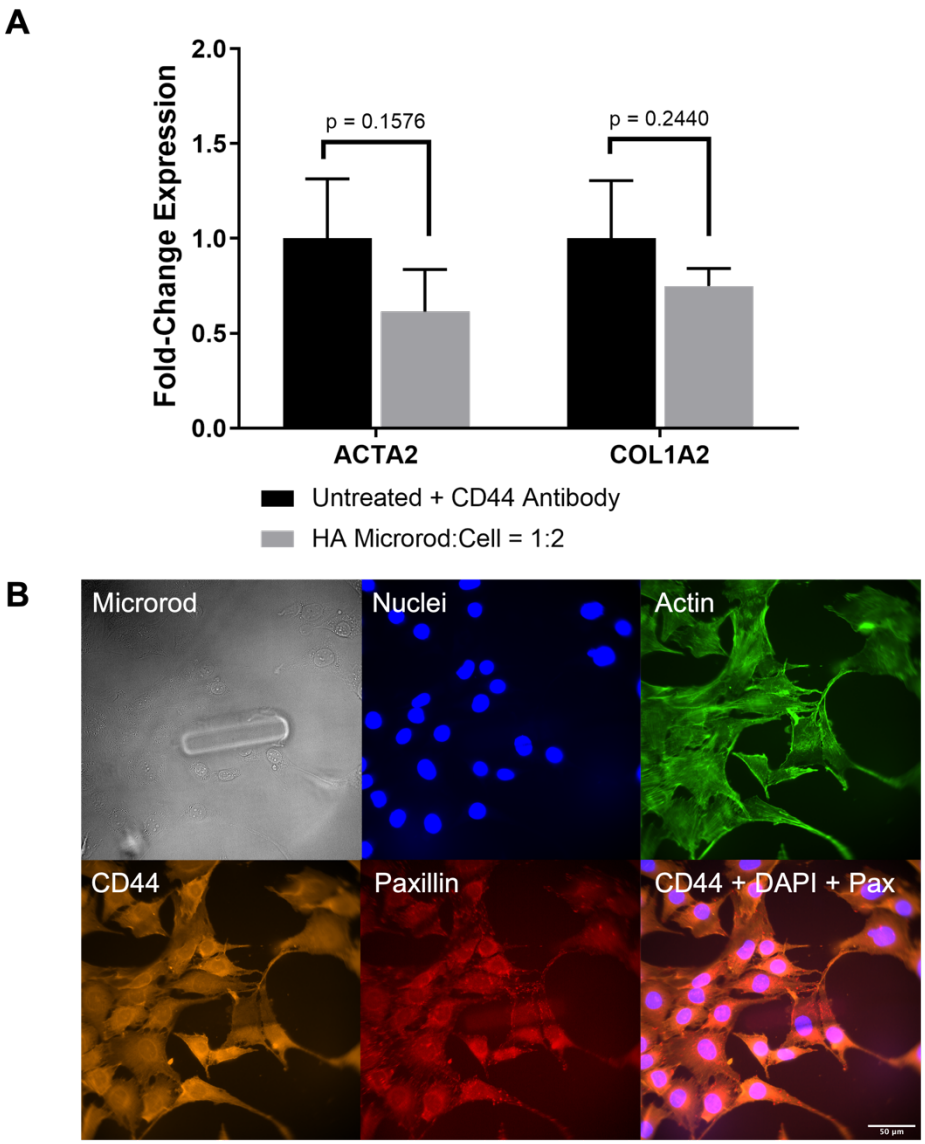

Figure 2.6. CD44 and hyaluronic acid microrod modulation of fibroblast phenotype. (A) NIH 3T3 fibroblasts were co-cultured with CD44 neutralizing antibody and yet, HA microrods still exhibit decreased gene expression of ACTA2 and COL1A2, pointing to another means of receptor engagement to HA microrods. The data are presented as the mean ± SD. (B) Fluorescent microscopy showcases staining of fibroblasts interacting with a microrod (nuclei = blue, actin = green, CD44 = orange, and paxillin = red. Scale bar = 50 µm.

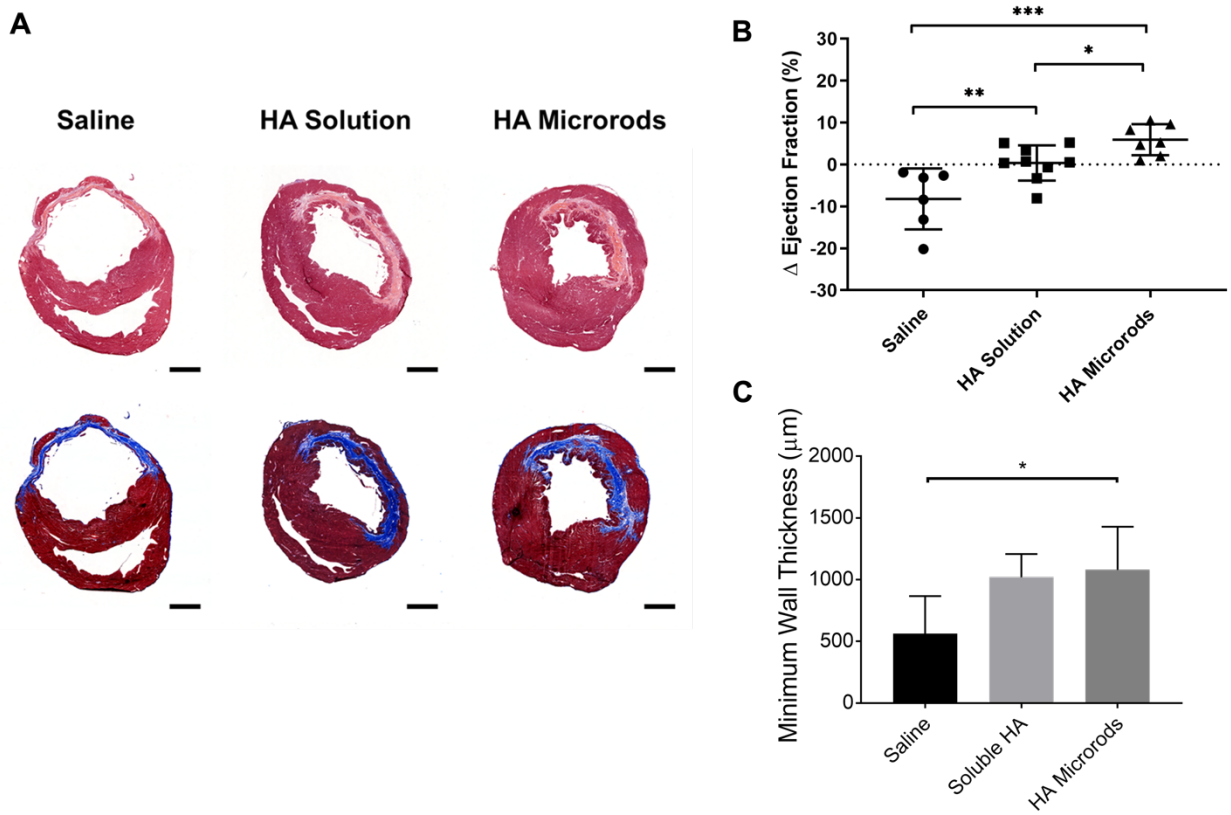

Figure 2.7. Hyaluronic acid microrod treatment improves cardiac performance post-MI. (A) Histological assessment was performed by staining cardiac tissue sections with H&E and Masson's trichrome using standard methods. (B) Ejection fraction (EF) at Day 2 (prior to injection) and 6 weeks (prior to sacrifice) post-MI was assessed via echocardiography in rats treated with saline (n = 6), HA solution (n = 9), and HA microrods (n = 7). Rats treated with HA microrods exhibit significantly higher change in EF after 6 weeks post-MI compared to rats treated with saline or HA solution. (C) Left ventricular wall thinning is significantly reduced in rats treated with HA microrods (n = 6) compared to those treated with saline (n = 7). Rats treated with HA solution (n = 8) also experienced reduced wall thinning. The data are presented as the mean ± SD. *p < 0.05, **p < 0.01, ***p < 0.001. Scale bars = 2 mm. Adapted from Le *et al*., 2018.

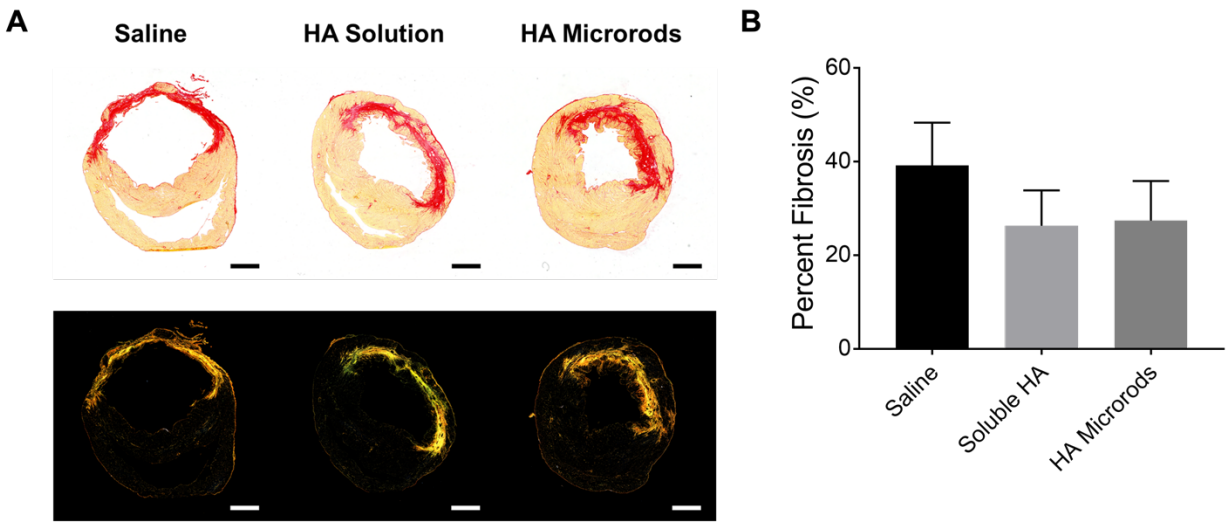

Figure 2.8. Hyaluronic acid and hyaluronic acid microrods moderately reduce fibrosis post-MI. (A) Histological assessment was performed by staining cardiac tissue sections with Picrosirius red using standard methods to quantify collagen content. Both brightfield and polarized imaging was performed. (B) Fibrosis area in the left ventricular free wall was measured and normalized to total area of the left ventricular free wall. Fibrosis appears to be moderately reduced after 6 weeks post-MI in animals treated with both HA solution and HA microrods. The data are presented as the mean ± SD. Scale bars = 2 mm. Adapted from Le *et al*., 2018.

Chapter 3 – Investigation of pro-angiogenic stimuli for use with hyaluronic acid microrods

3.1. Introduction

Adequate vascularization is critical to achieving myocardial regeneration and repair after cardiac injury. Impaired coronary and systemic perfusion observed in heart failure often leads to endothelial dysfunction and vascular rarefaction, which further contribute to the coronary environment being less amenable to cell survival.[187] Angiogenesis describes the formation of new microvessels from existing vasculature and is a vital response mechanism to decreased oxygen levels after ischemia to increase myocardial perfusion and mitigate pathological tissue damage.[16,188,189] Clinical trials involving the delivery of pro-angiogenic factors, like vascular endothelial growth factor (VEGF) and fibroblast growth factor (FGF), have demonstrated limited physiological improvements long-term.[190] One plausible explanation is the short half-life of these soluble factors that hinder translation to sustainable clinical benefits. Another strategy that is being explored is the delivery of recombinant genes to achieve persistent expression of pro-angiogenic targets. These trials have had mixed success, with some reporting substantial improvements in clinical endpoints[191,192], while others found no significant benefits over placebo.[190,193] There are also important concerns that need to be addressed with gene therapies including destruction by nucleases, risk of immune reactions, and potential formation of vascular tumors due to unregulated continuous gene expression.[190,194]

To date, there have been significant efforts to develop biomaterial platforms that can deliver pro-angiogenic factors to the post-infarct environment to encourage new

vessel formation. By tethering these pro-angiogenic molecules to the scaffold, it is possible to mitigate concerns of short half-life and have more control over biological presentation of the factor. There have been reports of hydrogel materials that were functionalized with VEGF, bFGF, platelet-derived growth factor (PDGF), and stromal-derived factor-1 (SDF-1) that were able to yield improved therapeutic outcomes and/or vascularization in various *in vivo* models.[195–198]

This chapter describes initial studies that aimed to characterize promising pro-angiogenic stimuli that may be used in conjunction with our developed HA microrod technology. Three peptides were investigated– Qk (KLTWQELYQLKYKGI), RoY (YPHIDSLGHWRR), and HepIII (GEFYFDLRLKGDKY)– for their ability to promote endothelial cell proliferation and tube formation. Qk is an engineered mimicking peptide that resembles the α-helix region of $VEGF_{165}$. Further, Qk has been reported to have similar *in vitro* and *in vivo* effects as $VEGF_{165}$, including the ability to induce capillary formation and neovascularization in rodent models of hind limb ischemia.[199,200] RoY is a synthetic peptide that binds to the GRP78 receptor on endothelial cells to induce increased cell proliferation, migration, and tube formation under hypoxic conditions.[201,202] HepIII is a peptide derived from collagen IV and has been demonstrated to enhance cell adhesion, proliferation, activation of Erk, and angiogenesis and arteriogenesis in rodent models of ischemia-reperfusion MI.[203]

3.2. Materials and Methods

3.2.1. Materials

Fluorescein-NHS, N′- ethylcarbodiimide hydrochloride (EDC), N-hydroxysulfosuccinimide (sulfo-NHS), Micro BCA Protein Assay Kits (#23235), and

CyQUANT Cell Proliferation Assays (#C7026) were purchased from Thermo Fisher Scientific (Waltham, MA). Hyaluronic acid methacrylate (HAMA) was synthesized and HA microrods were fabricated in our lab as discussed in Chapter 2. Qk (KLTWQELYQLKYKGI) and RoY (YPHIDSLGHWRR) peptides were purchased from LifeTein (Somerset, NJ). HepIII (GEFYFDLRLKGDKY) and HepIII-FITC were custom synthesized by GenScript (Piscataway, NJ). High concentration (HC) growth factor reduced (GFR) Matrigel (#354263) was obtained from Corning (Corning, NY).

3.2.2. Conjugation of HepIII and HepIII-FITC to HA microrods

HA microrods (75 mg/mL) were fabricated as described in Chapter 2. HepIII and FITC-HepIII peptides were conjugated to HA microrods via amine coupling by EDC/NHS chemistry. HA microrods were concentrated via centrifugation and then an equivalent volume of 50 mM 2-(N-morpholino)ethanesulfonic acid (MES) buffer with 0.2% Tween-20 (pH 5.5) was added to the HA microrod volume. Next, EDC and sulfo-NHS were dissolved in 25 mM MES buffer with 0.1% Tween-20 (pH 5.5) at 10 mM and 20 mM, respectively. Solubilized EDC and sulfo-NHS were then added to the microrods to generate a final concentration of 1 mM of EDC and 2 mM of sulfo-NHS and allowed to react for 30 mins with agitation at 4°C. For HepIII conjugation, HepIII was prepared in water at a concentration of 2 mg/mL and subsequently diluted four-fold to 0.5 mg/mL with 100 mM HEPES buffer with 0.1 % Tween-20 (pH 8.0). This was then added in equivalent volume to the activated microrods and left to react overnight with agitation at 4°C. For FITC-HepIII conjugation, FITC-HepIII was prepared in DMSO at a concentration of 2 mg/mL and subsequently diluted two-fold to 1 mg/mL with 100 mM HEPES buffer with 0.1 % Tween-20 (pH 8.0). This was then added in equivalent volume

to the activated microrods and left to react overnight with agitation at 4°C. The reaction was purified and conjugated HA microrods were separated by centrifugation with washes into water. Loading of HepIII into HA microrods was determined using a Micro BCA Protein Assay Kit (Thermo Fisher Scientific, Waltham, MA).

3.2.3. Cell culture & optimization studies

NIH 3T3 mouse fibroblasts (ATCC, Manassas, Virginia) were cultured in Dulbecco's modified Eagle's medium with 10% fetal bovine serum and 1% penicillin/streptomycin. Human umbilical endothelial cells (HUVECs) (Lonza, Basel, Switzerland) were cultured in EGM BulletKit (#CC-3124) (Lonza, Basel, Switzerland). Prior to investigating the effect of Qk, RoY, and HepIII peptides on HUVEC tube formation in 3D culture, a series of optimization experiments were conducted.

First, serum starvation conditions were optimized for HUVEC cells in 3D culture to minimize confounding variables as to whether serum or the added pro-angiogenic peptide was causing observed effects. The optimal starvation media condition was determined to be 0.5% serum and so this formulation was used for negative controls and all treatment conditions. Several volumes (25, 35, 45, 55, 65, 75 µL) of 10 mg/mL HC GFR Matrigel were examined to generate the substrate layer that HUVECs would grow on. We found that allowing 75 µL Matrigel to gel prior to seeding cells allowed for full coverage of 96 wells while minimizing variability in height throughout the well. Additional optimization required for tube formation studies included cell seeding density and incubation period. We tested four different seeding densities (15,000, 25,000, 35,000, and 45,000 cells/well) and two different time points (16 and 22 hours) to identify

ideal experimental conditions for observing tube formation in a 96 well plate. To visualize the tube networks, fluorescein diacetate (FDA) staining was used. FDA was first dissolved in acetone at 5 mg/mL to create a stock solution. To create a working solution, 8 µL of FDA stock was added to 5 mL of basal media. Media was aspirated from the wells and 125 µL of FDA working solution was added to each well and left to incubate at room temperature for 5 min while protected from light. The FDA solution was then removed from wells and samples were washed with phosphate buffered saline (PBS). After the wash step, basal media was added to each well and samples were imaged via fluorescent microscopy.

We observed that 35,000 cells plated onto 75 µL of 10 mg/mL HC GFR Matrigel in 96 wells plates and incubated for 16 hours exhibited the highest stability and integrity of the tubule network with minimal aggregation. At 22 hours, apoptosis started to occur, and the tubule network had begun disintegrating. Therefore, 35,000 cells/well and a 16-hour timepoint were used for all subsequent tube formation studies.

3.2.4. Tube formation studies

Soluble Qk, RoY, and HepIII peptide

HUVECs were serum starved for 24 hours prior to seeding. P7 HUVECs were subsequently seeded at 35,000 cells on top of a layer of 10 mg/mL GFR Matrigel. Qk, RoY, and HepIII peptides were added to cells at 6, 30, and 60 ng/mL in 0.5% FBS media and tube formation was observed after 16 hours. FDA staining, as described above, was used to visualize the tubules.

3.2.5. Proliferation studies

Soluble Qk, RoY, HepIII peptide

HUVECs were serum starved for 24 hours prior to seeding. P7 HUVECs were then seeded at a density of 5,000 cells/cm^2 and treated with varying concentrations of Qk, RoY, and HepIII peptide (10, 50, 100 ng/mL) in triplicate. Media with 0.5% serum was used as a negative control. Proliferation was assessed over 72 hours via a CyQUANT assay.

Adsorbed RoY and HepIII peptide

HUVECs were serum starved for 4 hours prior to seeding. 50 µL of varying concentrations of RoY and HepII (10, 50, 100, 400, and 800 ng/mL) in PBS were added to bottom of a 96 well plate in triplicate. The 96 well plate was left at room temperature in the tissue culture hood to allow for evaporation. Media with 0.5% serum was used as a negative control. P7 HUVECs were then seeded at a density of 20,000 cells/cm^2 and treated with varying concentrations of Qk, RoY, and HepIII peptide (10, 50, 100 ng/mL). Proliferation was assessed over 48 hours via a CyQUANT cell proliferation assay (Thermo Fisher Scientific, Waltham, MA).

HA microrod and HepIII microrod treatment – HUVECs

The desired amount of either HA microrods or HepIII microrods (1:2, 1:5, or 1:20 microrods:cells) were first deposited onto the bottom of the cell culture wells, followed by the addition of P11 HUVECs at a seeding density of 6,000 cells/cm^2 in phenol red free media. A HepIII coating equivalent to the amount of HepIII dosed in the highest

density of HepIII microrod treatment was included (~554 ng/well). Proliferation was assessed at 48 and 120 hours via a CyQUANT assay (Thermo Fisher Scientific, Waltham, MA).

HA microrod and HepIII microrod treatment – NIH 3T3 fibroblasts

The desired amount of either HA microrods or HepIII microrods (1:2, 1:5, 1:10, or 1:20) were first deposited onto the bottom of the cell culture wells, followed by the addition of NIH 3T3 fibroblasts at a seeding density of 10,000 cells/cm^2. Proliferation was assessed over 72 hours via a CyQUANT assay (Thermo Fisher Scientific, Waltham, MA).

3.2.6. qPCR studies

HA microrod and HepIII microrod treatment – NIH 3T3 fibroblasts

HA microrods and HepIII microrods (ratio of 1:2 microrods:cells) were cultured with NIH 3T3 fibroblasts and HUVECs in individual cultures. The desired amount of HA microrods or HepIII microrods were first deposited onto the bottom of the cell culture wells, followed by the addition of cells at a seeding density of 10,000 cells/cm^2. Genetic material was harvested using the RNEasy Mini Kit (Qiagen, Hilden, Germany). RNA was converted into cDNA using the iScript cDNA synthesis kit (Bio-Rad Laboratories, Hercules, CA). A Viia7 qPCR machine (Life Technologies, Carlsbad, CA) and Fast SYBR Green Master Mix (Life Technologies, Grand Island, NY) was used to perform qPCR. Relative gene expression levels of gene targets were calculated using the ΔΔCt method and normalized to the housekeeping gene. Custom-made DNA primers

(Integrated DNA Technologies, Coralville, IA) that were used for these experiments can be found in Table 3.1.

HA microrod and HepIII microrod treatment – HUVECs

The desired amount of HA microrods or HepIII microrods (1:2, 1:5, 1:10, or 1:20 microrods:cells) were first deposited onto the bottom of the cell culture wells, followed by the addition of P7 HUVECs at a seeding density of 10,000 cells/cm^2. After two days, genetic material was harvested using the RNEasy Mini Kit (Qiagen, Hilden, Germany). RNA was converted into cDNA using the iScript cDNA synthesis kit (Bio-Rad Laboratories, Hercules, CA) and a Viia7 qPCR machine (Life Technologies, Carlsbad, CA) was used to measure relative expression levels of gene targets compared to the housekeeping gene 60S ribosomal protein L19 (RPL19). Expression levels of all genes were evaluated using the Fast SYBR Green Mastermix (Life Technologies, Grand Island, NY) and custom DNA primers (Integrated DNA Technologies, Coralville, IA) in triplicate for three biological replicates (Table 3.1).

3.2.7. Statistical Analysis

All data are presented as the mean ± standard error of the mean unless otherwise indicated. *In vitro* analysis was performed using either student's t-tests to identify statistical differences between two groups or a one-way analysis of variance (ANOVA), followed by the Tukey's multiple comparisons test to identify differences between three or more groups.

3.3. Results

3.3.1. Effect of pro-angiogenic peptides Qk, RoY, and HepIII on endothelial cell tube formation and proliferation

Peptides Qk (KLTWQELYQLKYKGI), RoY (YPHIDSLGHWRR), and HepIII (GEFYFDLRLKGDKY) were all investigated as potential pro-angiogenic stimuli that could be combined with the HA microrod technology to yield more potent therapeutic outcomes during the treatment of MI. The capacity for endothelial cells to connect and form networks of tubules and proliferate is critical for the formation of patent, functional vessels. As such, the impact of these peptides on these endothelial cell behaviors were assessed in a series of studies. Prior to initiating these experiments, optimization of serum starvation conditions, cell seeding densities, and timepoints were performed. It was determined that optimal conditions of starvation media for HUVECs was 0.5% FBS in basal media. Furthermore, a cell seeding density of 35,000 cells/well and 16-hour timepoint were ideal for investigating tube formation of HUVECs on GFR Matrigel (Figure 3.1). These identified parameters were used in all subsequent studies, unless otherwise stated.

When Qk, RoY, and HepIII were solubilized and dosed to HUVECs at varying concentrations (6, 30, and 60 ng/mL), distinguishable differences in tube formation as visualized via fluorescence microscopy were observed (Figure 3.2). As expected, complete starvation media at 0.5% FBS did not show any formation of endothelial cell tubes. Only the highest dose of Qk peptide (60 ng/mL) demonstrated slight connections of endothelial cells into budding tubes, however these clusters of tubes were never connected to others. Increased tube formation was observed in RoY peptide-treated

conditions in a dose-dependent manner. As the concentration of RoY peptide increased, so did the tube coverage area, length of tubes, and number of connections. Interestingly, tube formation in response to HepIII concentration seem to follow a bell curve; at lower and higher concentrations of HepIII dosing, tube formation was decreased, while the middle concentration of 30 ng/mL bestowed the most favorable conditions for tube formation. These observations of HepIII having an optimal dosing range are in line with previous reports.[203]

Next, the effect of Qk, RoY, and HepIII treatment on HUVEC proliferation was characterized over three days. Qk, RoY, and HepIII were solubilized in starvation media and dosed at 10, 50, and 100 ng/mL. CyQUANT assays were performed at 24, 48, and 72 hours to assess total cell number at each timepoint. While not significant, several trends were identified based on the cell growth profiles observed from the different peptide treatments. A dosing of 50 ng/mL of HepIII yielded the highest total number of cells at 72 hours out of all other treatments (Figure 3.3A). Percentage growth at 48 and 72 hours was then calculated as follows: $Percentage\ growth\ at\ 48/72\ hr = \frac{(Cell\ \#\ @\ 48/72\ hr - Cell\ \#\ @\ 24\ hr)}{Cell\ \#\ @\ 24\ hr} x\ 100\%$. At 72 hours, Qk (10 ng/mL), RoY (50 ng/mL), and HepIII (50 ng/mL) treatments exhibited high percentage growth based on their respective cell numbers at the 24-hour timepoint (Figures 3.3C). Based on both the proliferation and tube formation data, we decided to characterize RoY and HepIII peptides further in our experiments. Given that once conjugated to the surface of HA microrods, the peptide will not be presented in its soluble form, we wanted to assess the impact of adsorbed peptide on HUVEC proliferation. RoY or HepIII peptide was solubilized in PBS at 10, 50, 100, 400, 800 ng/mL and added to the bottom of 96 wells

and allowed to adhere overnight. HUVECs were then seeded into each treatment condition and proliferation was observed over 48 hours. Total cell number over 48 hours was plotted, and it was found that treatments with 10, 100, 800 ng/mL of RoY peptide (p = 0.038, p = 0.034, and p = 0.011, respectively) and 50 ng/mL of HepIII peptide (p = 0.061) caused notable increases in cell number compared to control (Figure 3.4A). Percentage growth at 24 and 48 hours compared to 12 hours were calculated and while no significant trends existed at 24 hours, treatments with 100, 400, and 800 ng/mL of RoY peptide (p = 0.054, p = 0.068, and p = 0.063) and 10 and 50 ng/mL of HepIII peptide (p = 0.079 and p = 0.096, respectively) showed trends towards increased cell growth compared to control (Figures 3.4B-C).

3.3.2. Effect of HepIII microrods on endothelial cell and fibroblast behaviors

HepIII was selected to move forward with the HA microrod strategy due to its favorable performance in increasing proliferation and tube formation in HUVECs. Further, our lab has experience with conjugation of HepIII to polymer materials.[180] HepIII peptide that was modified with a FITC tag was used to confirm successful conjugation to HA microrods using EDC/NHS carbodiimide chemistry (Figure 3.5A). To ascertain whether HepIII peptide was adsorbed versus conjugated to the surface of HA microrods, we set up two reactions where EDC/NHS was either present or absent. Therefore, any HepIII that was detected in the microrod reaction that did not contain EDC/NHS could be deemed as adsorbed to the surface of the microrods. Based on fluorescence imaging, minimal amounts of HepIII were found to adsorb to the microrod surface as evidenced by the absence of FITC signal (Figure 3.5B). Protein quantification using a Micro BCA Protein Assay showed that there is approximately 27.7

μg of HepIII per 50,000 HA microrods (microrod dosing used for *in vivo* injections) based on our conjugation reaction (Figure 3.5C). Fluorescent imaging also demonstrated that HepIII is conjugated throughout the geometry of the HA microrod and was not strictly localized to the surface (Figure 3.6).

After confirming successful conjugation of HepIII to HA microrods, we wanted to assess the ability for HepIII microrods to affect endothelial cell behaviors while still being able to modulate fibroblast phenotype. Both endothelial cell and fibroblast proliferation were assessed when treated with varying doses of microrods (1:2, 1:5, 1:10, or 1:20 microrods:cells). HepIII microrods dosed at 1:2 microrods:cells exhibited significant increases in percentage growth at 120 hours (compared to 48 hours) versus control, all doses of HA microrods, and the 1:20 HepIII microrod ratio ($p < 0.05$ for all). HA microrods did not appear to impact HUVEC proliferation compared to control (Figure 3.7A). HA microrods at all doses demonstrated increased percentage growth at 72 hours (compared to 24 hours) versus control (Figure 3.7B). Interestingly, only the 1:10 ratio of HepIII microrods demonstrated a significant increase in proliferation compared to control ($p < 0.01$). Overall, HA microrods and HepIII microrods exerted similar effects on fibroblast proliferation at equivalent dosing.

Lastly, gene expression in fibroblasts and HUVECs were evaluated after treatment with HA microrods and HepIII microrods. It was found that at an equivalent dosing of 1:2 microrods:cells, both HA microrod and HepIII microrods showcased similar downregulation of ACTA2 expression in NIH 3T3 fibroblasts (Figure 3.8A). This indicates that the conjugation of HepIII did not impede the ability for microrods to exert topographical modulation on fibroblasts. Given the pro-angiogenic effects of HepIII on

proliferation and tube formation, we wanted to explore if HepIII microrods had any effect on NOS3 gene expression in HUVECs. The NOS3 gene encodes for nitric oxide synthase 3, an enzyme that is responsible for the production of nitric oxide which is a potent regulator of endothelial cell behaviors and angiogenesis.[204] However, our results show that there is no difference in NOS3 gene expression between control, HA microrods, or HepIII microrods at any dose (1:2, 1:5, 1:10, or 1:20 microrods:cells) after two days of microrod treatment (Figure 3.8).

3.4. Discussion

Therapeutic angiogenesis is a promising strategy to produce new collateral blood vessels in ischemic myocardium to mitigate severity of tissue damage due to ischemia.[188] This process relies on endothelial cell proliferation and migration in conjunction with extracellular matrix remodeling to develop new blood vessels.[205] Unfortunately, endogenous mechanisms for induction of angiogenesis during cardiac injury are not very effective as less than one-third of patients with coronary artery disease develop sufficient collateral vasculature.[206] However, studies have shown that new vessel formation along the endocardium in the ischemic zone can enhance cardiomyocyte survival and decrease maladaptive ventricular remodeling in infarcted hearts.[207] Further, the development of an adequate vascular bed in ischemic tissue should enable increased cell engraftment and survival.[208–210] Therefore, there is great interest in developing strategies to bolster endogenous neovascularization to improve rescue and repair process in cardiac tissue.

Delivery of growth factors, genes, and stem cells to address issues of myocardial perfusion have been explored.[16,190,191,211] However, challenges associated with short

half-life, immunogenic risk, and low engraftment have hindered therapeutic efficacy of these strategies. Recent years have seen an increased interest in leveraging biomaterials to deliver key physiological cues to aid in tissue regeneration and repair. Characteristics of biomaterials including biocompatibility, biodegradation, tunable mechanical properties are very desirable for promising translational therapies. Further, the capacity for biochemical modification to incorporate bioactive components greatly enhances the utility of biomaterials to address a diverse array of clinical diseases. Synthetic peptides with sequences that represent epitopes of bioactive sites and mimic their native structural conformation have represented a promising source of pro-angiogenic stimuli. Many synthetic pro-angiogenic peptides are VEGF mimics, given that VEGF is a core regulator of angiogenic processes.[212] One extensively researched peptide called Qk is a synthetic peptide that reproduces the helix region 17-25 from the binding region of VEGF and has been investigated for its capacity to induce pro-angiogenic behaviors in endothelial cells such as increasing endothelial cell proliferation, VEGF signaling, and neovascularization.[199,200] However, there are several other peptides that target other growth factor receptors which work alongside VEGF pathways. RoY is a synthetic peptide consisting of 12 amino acids that was shown to promote pro-angiogenic activity in endothelial cells experiencing hypoxia through binding to heat shock protein GRP78.[201] Another peptide of interest is HepIII, which has demonstrated its capacity to increase endothelial cell attachment, proliferation, migration, and activation of the Erk1/2 signaling pathway.[203]

In this work, we investigated the three synthetic peptides Qk, RoY, and HepIII for their potential in inducing endothelial cell proliferation and tube formation so that we

could create a dual-acting, anti-fibrotic and pro-angiogenic microtechnology therapy. After a series of in vitro assessments, we identified HepIII as a promising candidate to move forward with. Other studies have explored targeting HepIII delivery to the infarct site to enhance therapeutic efficacy in models of cardiac injury.[180,203] HepIII was conjugated to anti-rat cardiac α-myosin heavy chain (anti-MHC) and injected intravenously into rodents that underwent ischemia-reperfusion (I/R) MI. Results showed that the delivery of the ECM peptide to the infarct region resulted in enhanced neovascularization and decreased ventricular remodeling.[203] Additionally, when HepIII was conjugated to thermo-reversible carboxymethylcellulose (CMC) and delivered to the infarct region, rats exhibited increased wall thickness, cardiac function, and angiogenesis along with reduced infarct size compared to rats treated with vehicle and non-peptide modified CMC.[180]

While HepIII has been less researched in the therapeutic biomaterials space, its pro-angiogenic effects may be traced to its integrin bindings partners. Several studies have reported that HepIII binds both integrins $\alpha_2\beta_1$ and $\alpha_3\beta_1$.[213,214] Work done in dermal microvascular cells demonstrated that binding to $\alpha_2\beta_1$ led to VEGF-mediated activation of the Erk1/Erk2 signaling pathway and migration *in vitro*, both of which are crucial for angiogenesis.[215] Additionally, studies in keratinocytes showed that $\alpha_3\beta_1$ is also implicated in the Erk1/Erk2 signaling pathway.[216]

Here, we demonstrated the successful conjugation of HepIII to HA microrods (Figure 3.5) with HepIII present throughout the entirety of the microrod, and not strictly localized to the microrod surface (Figure 3.6). Early preliminary work demonstrated functional equivalency to HA microrods with respect to modulating fibroblast phenotype

(Figure 3.8A), while also maintaining the unique ability to improve HUVEC proliferation (Figure 3.7). In our studies, we didn't observe any differences in NOS3 expression between control, HA microrods, and HepIII microrods (Figure 3.8B). While angiogenic factors, including VEGF, have been reported to increase expression of NOS3, it is possible that due to HepIII's integrin-mediated activity, distinct pathways involved in angiogenesis that do not directly involve NOS3 are activated.[217–219]

While the RoY peptide was not pursued in this work, it also showed great potential as a viable bioactive component to be incorporated with the HA microrod strategy. Previous studies have demonstrated the capacity for RoY peptide to promote endothelial cell proliferation, migration, and tube formation under hypoxic conditions *in vitro* as well as induce therapeutic angiogenesis in rodent models of ischemia through binding to heat shock protein GRP78.[201,202,220] Future work conjugating RoY peptide to HA microrods should also explore testing culture conditions in hypoxic environments as GRP78 is typically overexpressed on endothelial cells in low oxygen environments.

The ability to incorporate pro-angiogenic functionality to microrods shows great promise to enhance post-MI therapeutic efficacy of the microrod platform by stimulating endogenous mechanisms to create *de novo* vasculature while minimizing fibrosis to support myocardial repair.

Table 3.1. Primers used for qPCR.

Target Gene	Forward Primer (5’ -> 3’)	Reverse Primer (5’ -> 3’)
RPL19	CATTTTGCCCGACGAAAGGG	GATCTGCTGACGGGAGTTGG
ACTA2	GCTGCTCCAGCTATGTGTGA	CCATTCCAACCATTACTCCCTGA
NOS3	TGATGGCGAAGCGAGTGAAG	ACTCATCCATACACAGGACCC

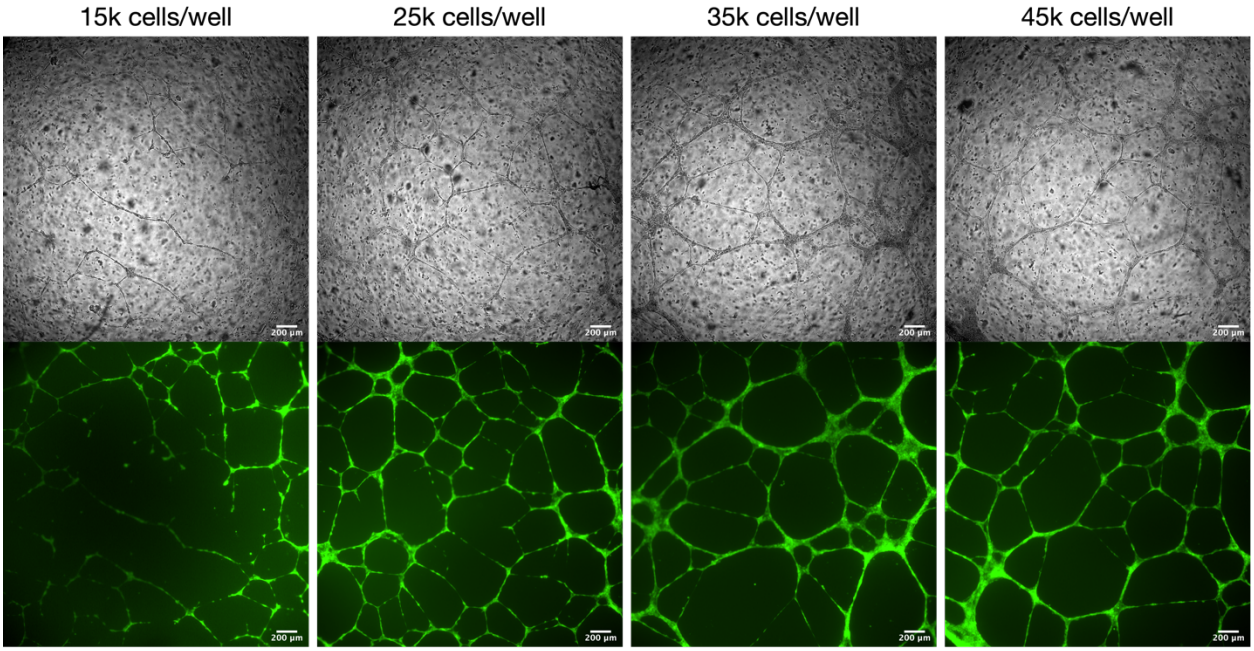

Figure 3.1. Optimization of the tube formation assay. Varying cell seeding densities (15,000, 25,000, 35,000, and 45,000 cells/well) and time points (16 and 22 hours) were investigated for optimal tube network formation. Brightfield (top) and fluorescence (bottom) microscope images were taken at 16 hours to observe tube formation of HUVECs seeded onto high concentration growth factor reduced Matrigel. Scale bars = 200 µm.

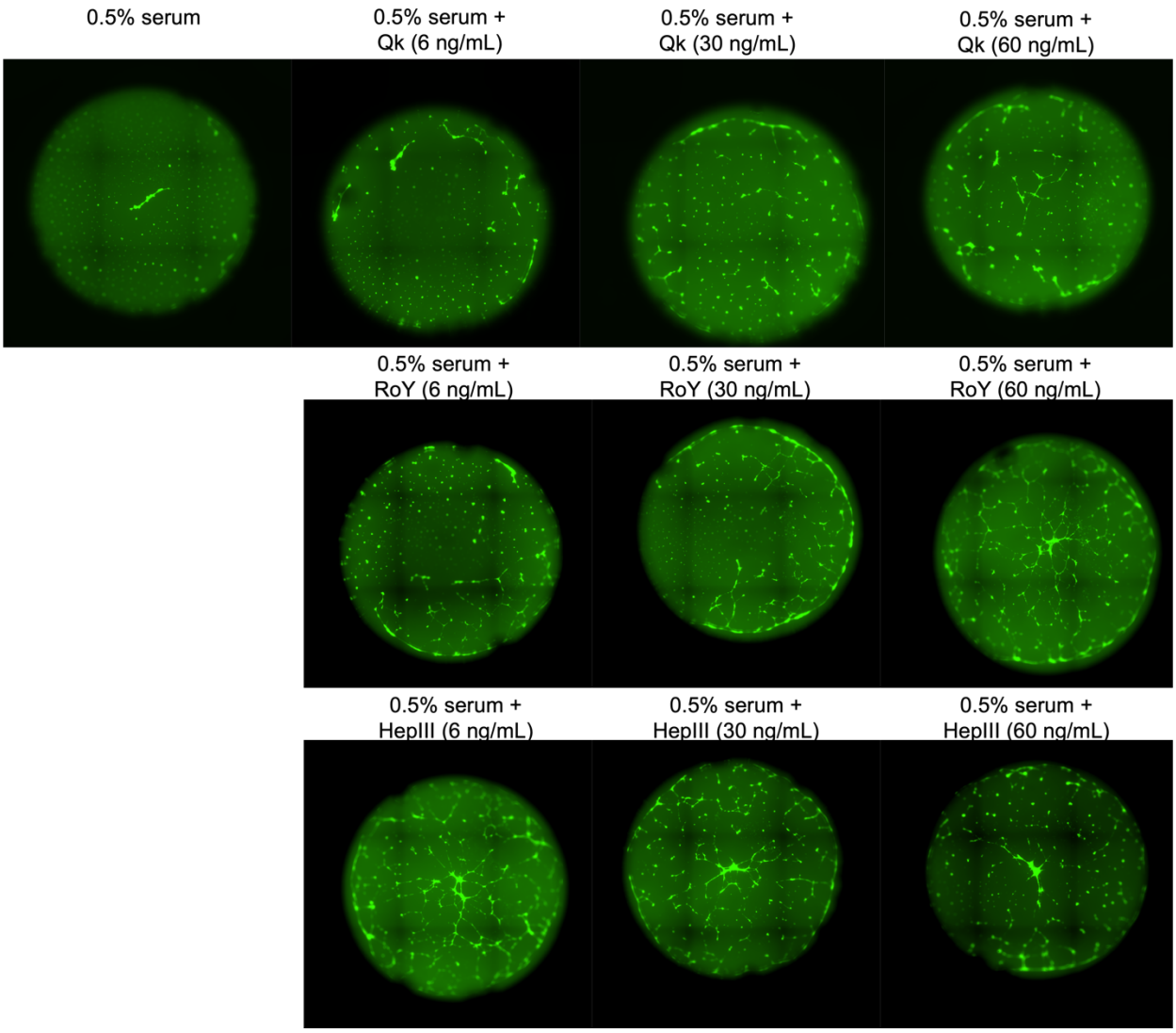

Figure 3.2. Qk, RoY, and HepIII treatment affects tube formation. HUVECs were treated with varying concentrations (6, 30, and 60 ng/mL) of Qk, RoY, and HepIII peptides and observed for tube network formation after 16 hours. Media with 0.5% serum served as the negative control. Both RoY and HepIII peptide treatment seemed to improve tube network formation in HUVECs compared to Qk peptide treatment.

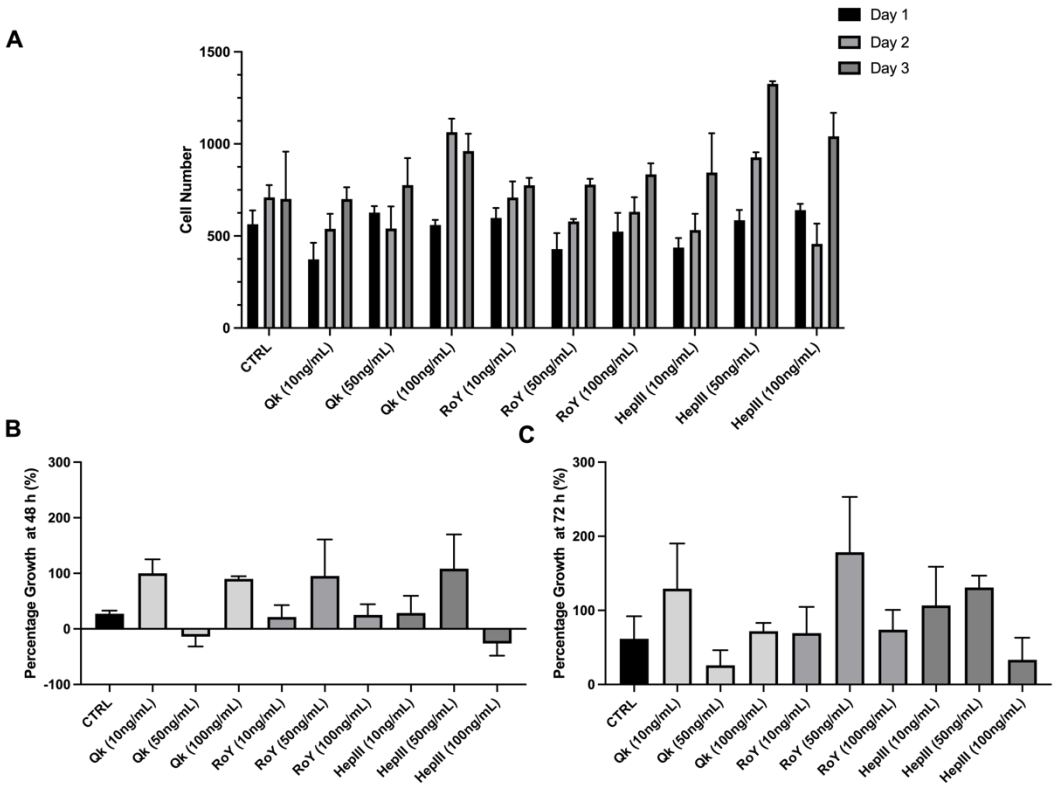

Figure 3.3. Effect of soluble Qk, RoY, and HepIII peptides on endothelial cell proliferation. All three peptides demonstrated a trend towards improved growth rate of HUVECs, though it appears the effect is concentration dependent. (A) Cell number of HUVECs that were treated with Qk, RoY, and HepIII at 10, 50, and 100 ng/mL over three days. (B-C) Maximal effects on proliferation at 48 and 72 hours compared to 24 hours occurred with lower concentrations of peptides. The data are presented as the mean ± SEM.

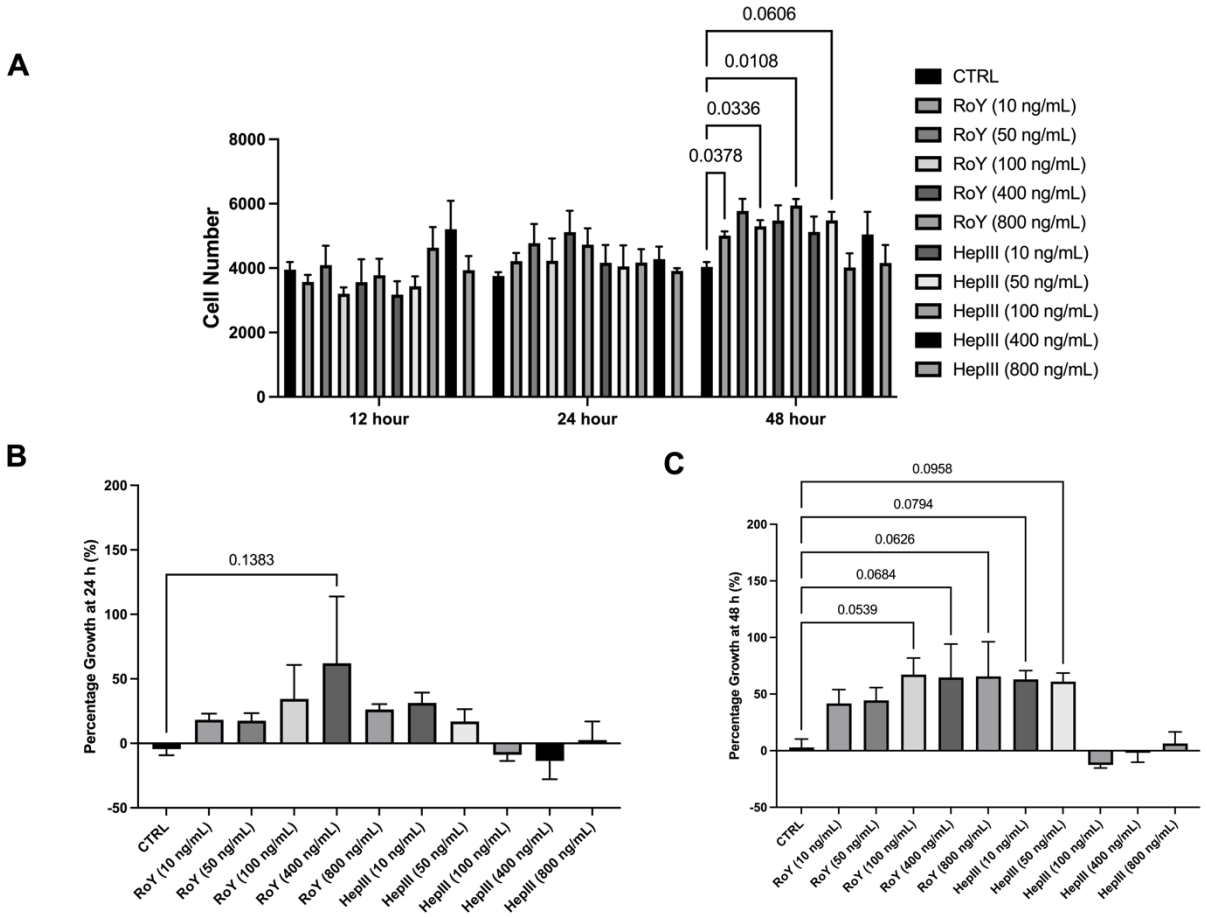

Figure 3.4. Effect of adsorbed RoY and HepIII peptides on endothelial cell proliferation. Both RoY and HepIII peptides demonstrated increased proliferation of HUVECs. (A) Cell number of HUVECs that were grown on wells treated with 50 µL of 10, 50, 100, 400, or 800 ng/mL of RoY or HepIII peptide. (B-C) Growth rates at 24 and 48 hours of HUVECs are shown. Higher concentrations of RoY peptide and lower concentrations of HepIII significantly improved HUVEC growth at 48 hours. The data are presented as the mean ± SEM.

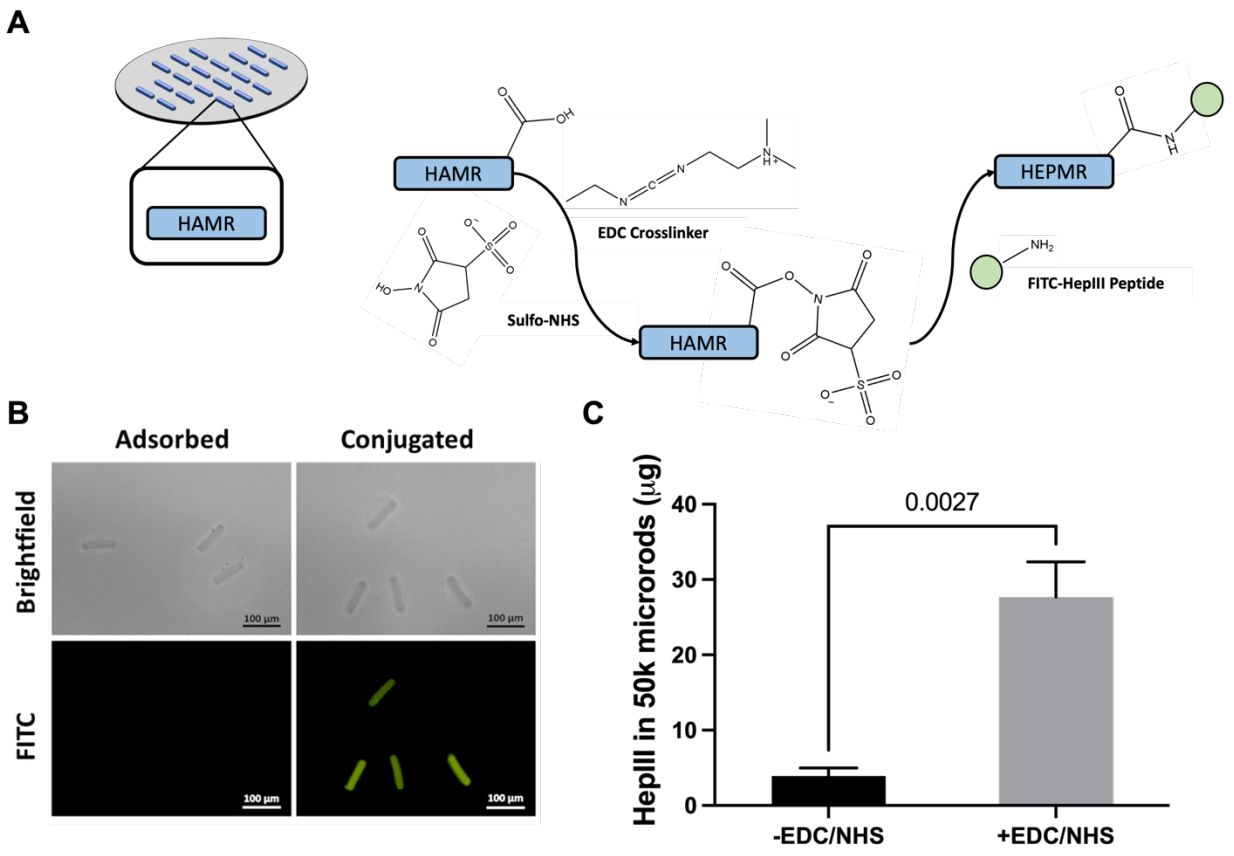

Figure 3.5. Conjugation scheme of HepIII to HA microrods. (A) A schematic describing the coupling of HepIII peptide to HA microrods (HAMRs) by amine coupling via EDC/NHS chemistry to create HepIII microrods (HEPMRs). (B) Brightfield and fluorescence images confirm the conjugation of FITC-modified HepIII peptide only when EDC/NHS were included in the reaction. Minimal HepIII is found to adsorb to the microrods as evidenced by the absence of FITC signal in the microrods that did not have EDC/NHS. (C) Protein quantification studies showed that approximately 27.7 µg of HepIII is present per 50,000 HA microrods based on our conjugation reaction. The data are presented as the mean ± SD. Scale bars = 100 µm.

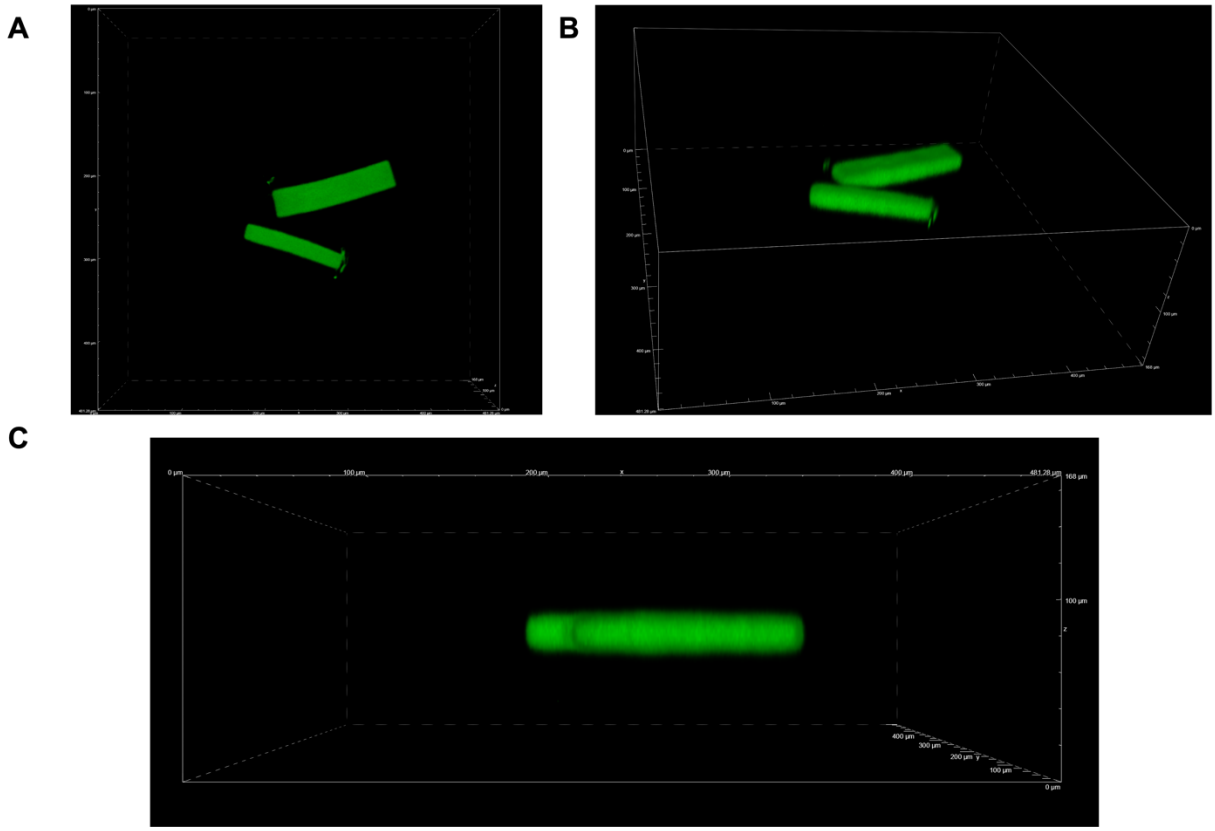

Figure 3.6. Conjugated HepIII is present throughout the microrod geometry. Fluorescence microscopy was used to visualize HepIII microrods throughout the 3D plane. Images provided above are as follows: (A) XY-plane, (B) XYZ-plane, and (C) XZ-plane.

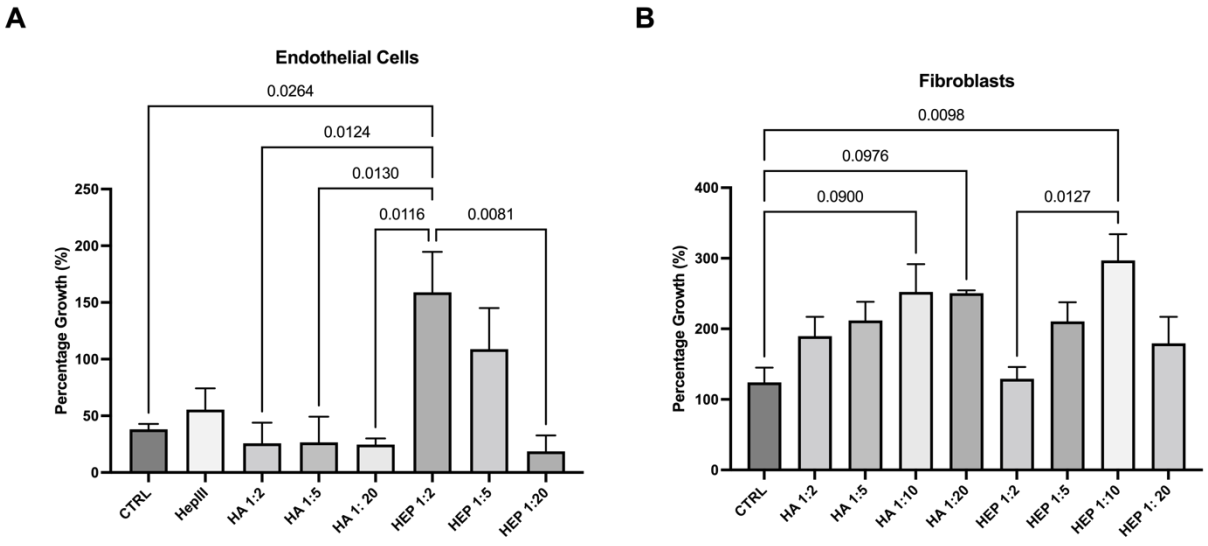

Figure 3.7. Comparison of HA microrods and HepIII microrods on endothelial cell and fibroblast proliferation. (A) Evaluation of varying ratios of HA microrods and HepIII microrods (1:2, 1:5,1:20 microrods:cells) on HUVEC proliferation indicate that higher ratios of HepIII microrods significantly increase proliferation compared to control, all HA microrods ratios, and the lowest HepIII microrod ratio. Percentage growth depicts a comparison of cell number at 120 hours and 48 hours. (B) Evaluation of varying ratios of HA micorods and HepIII microrods (1:2, 1:5, 1:10, and 1:20 microrods:cells) on NIH 3T3 fibroblast proliferation showed that all HA microrods and HepIII microrods at equivalent ratios perform equivalently in improving fibroblast proliferation. Percentage growth depicts a comparison of cell number at 72 hours and 24 hours. The data are presented as the mean ± SEM.

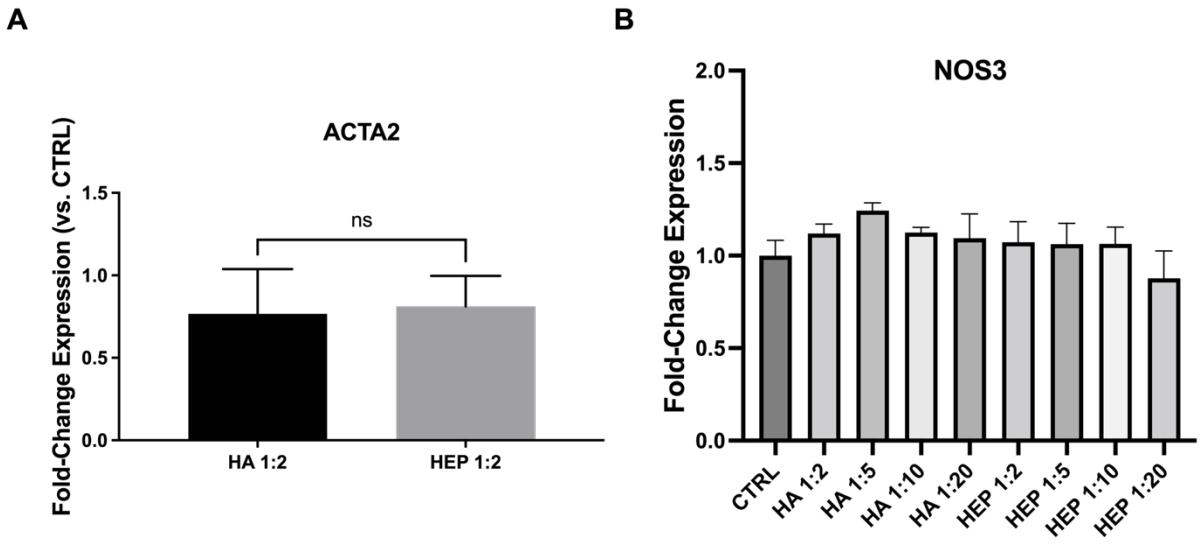

Figure 3.8. Comparison of HA microrods and HepIII microrods on fibroblast and endothelial cell gene expression. (A) Equivalent ratios of HA microrods and HepIII microrods exhibit similar downregulation of ACTA2 in NIH 3T3 fibroblasts, indicating that the addition of HepIII does not interfere with the biophysical regulation of fibroblasts by microrods. (B) There is no difference in NOS3 gene expression between control, HA microrods, or HepIII microrods after two days of microrod treatment. The data are presented as the mean ± SEM.

Chapter 4 – Localized delivery of decorin via hyaluronic acid microrods improves cardiac performance after myocardial infarction

4.1. Introduction

Heart failure (HF) affects approximately 6 million Americans, and the prevalence is projected to increase 46% from 2012 to 2030.[221] The prognosis for HF is poor, with an estimated mortality rate of 50% within 5 years of the diagnosis. Myocardial infarction (MI) from coronary artery disease is the leading cause of HF and despite advances in the management of MI, subsequent pathologic remodeling of ischemic myocardium with fibrotic scar tissue and aneurysmal degeneration leads to HF and death. Therefore, therapies that can prevent scar tissue formation, increase cell survival, and promote contractile tissue regeneration need to be identified to treat this growing patient population in the wake of increasing rates of obesity and heart disease.[221] To date, cellular therapies have had limited success in promoting long-term cardiovascular repair[222,223] and no delivery system for an effective pharmacotherapy exists. Moreover, current treatment of fibrosis involves systemic inhibition of cytokines and chemokines which leads to many adverse side effects for patients.[224,225]

In recent years, there has been growing interest in targeting pathways that lead to altered cardiovascular cell phenotypes and microenvironments after injury to reduce maladaptive repair and promote functional recovery. As most of these cell types are mechanosensitive and rely on micro- and nanoscale cues from the extracellular matrix (ECM) to dictate homeostatic function, it is possible to harness these interactions through biomaterials with similar size scale biophysical cues to

elicit more native cell phenotypes, thereby mitigating cardiovascular disease progression and enhancing regenerative potential.[226] Fibroblasts represent the largest percentage of cells in the heart and coordinate numerous functions including ECM turnover, cell-cell signaling, and cytokine and growth factor secretion. After MI, fibroblasts transform into a highly contractile, activated phenotype known as myofibroblasts which function to stabilize the injury site by increasing ECM deposition to preserve the integrity of the myocardial wall and maintain the pressure generating ability of the heart.[227] While this compensatory process is initially beneficial, problems arise when pro-fibrotic inflammatory signals such as TGF-β1 persist, leading to continual deposition of stiff scar tissue which ultimately impairs contractility and perfusion within in the heart.[227]

We have previously demonstrated the ability to modulate fibroblast morphology and function using polymeric microstructural cues to achieve less fibrotic phenotypes, which could have tremendous implications in heart failure therapy.[228–231] Recent work showed that *in vitro* treatment with polymeric microrods (15 x 15 x 100 μm) decreased fibroblast proliferation and that microrod injections in preclinical rodent models of heart failure cause reductions in scar tissue and improvements in cardiac function by influencing the cardiac microenvironment.[230,231] Benefits of using hydrogel microstructure strategies with mechanobiological mechanisms of action as therapeutic approaches for cardiovascular diseases include being injectable, cell-free, and highly tunable in terms of geometry, stiffness, and material. Further, as their therapeutic effects are restricted based on proximity, concerns related to systemic side effects are avoided. Being hydrogels also allows for combination therapies with

the ability to load and release various therapeutic factors from the microstructures.[101,232] The ability to devise more potent, multi-faceted therapies can have tremendous implications on myocardial regeneration after MI by addressing multiple pathological processes.

Reperfusion strategies are a key component in the management of acute MI but can lead to ischemia reperfusion injury (IRI), which is widely characterized by oxidative stress, inflammation, intracellular Ca^{2+} overload, fibrosis, and endothelial dysfunction.[233–235] Although the exact mechanisms of IRI remain unknown, targeting oxidative damage and subsequent fibrotic response that occurs after myocardial reperfusion is critical to cardiac recovery after MI. Several naturally occurring biological macromolecules within the body possess unique characteristics that may enhance antioxidant functions. Small leucine rich proteoglycans (SLRPs) are ubiquitous ECM components involved in structural organization and are known regulators of collagen fibril assembly.[236] Decorin, a class I SLRP, has been shown to have both antifibrotic and antioxidant properties. It has been reported to sequester the profibrotic cytokine TGF-β with high affinity and modulate collagen fibrillogenesis.[237–243] Preclinical studies have demonstrated a therapeutic role of decorin in mitigating fibrosis in various in vivo models of ischemic injury[244–246] and in vitro fibrosis models.[247–249] There is a protective role of decorin after traumatic injury in vivo which is linked to oxidative stress response.[244,250] In cell studies with high glucose and oxygen/glucose-deprived environments, protective effects of decorin center on involvement in apoptosis and oxidative stress pathways.[251,252] Therefore,

there may exist an important role for decorin in early response therapies for cardiovascular injury.

Hence, our approach in this study is to introduce bioactive, decorin-loaded hyaluronic-acid (HA) microstructural cues into the post-infarct microenvironment to regulate pathological cell responses and transform the wound healing microenvironment by providing discrete micromechanical and biochemical cues. We demonstrate the impact of decorin-loaded microrods on cardiac function, ventricular remodeling, fibrosis, and hypertrophy post-MI.

4.2. Materials and Methods

4.2.1. Materials

Sodium hyaluronate (100kDa) was obtained from Lifecore Biomedical and stored at -20°C until use. Dimethylformamide (DMF), glycidyl methacrylate (GM), triethylamine (TEA), and 2-hydroxy-4′-(2-hydroxyethoxy)-2-methylpropiophenone (#410896) were purchased from Sigma-Aldrich and used as received. Spectrum™ Spectra/Por™ 3 RC dialysis membrane tubing, 3500 Dalton MWCO (#08-670-5B), Wheat Germ Agglutinin, Alexa Fluor 488 (#W11261), Hoescht (#33342), and high concentration rat tail collagen type I (#CB354249) was purchased from Thermo Fisher Scientific (Waltham, MA). Recombinant human TGF-β1 (#100-21) was obtained from PeproTech. Recombinant human decorin protein (ab167743), human decorin ELISA kit (ab99998), anti-decorin antibody (ab151988), anti-sarcomeric alpha actinin (ab137346), and anti-alpha smooth muscle actin (ab5694) were purchased from Abcam.

4.2.2. Decorin loading of HA microrods

HA methacrylate was synthesized and HA microrods (75 mg/mL) were fabricated per the methods described in Chapter 2. To passively load microrods with decorin protein, the microrod concentration was first determined. Next, 750,000 microrods were concentrated in 1 mL of deionized (DI) water and then 333 µL of decorin (600 µg/mL) was added. The microrods were passively loaded via incubation with inversion for four days at 4°C. After incubation, the microrods were centrifuged at 15000 × *g* for 10 minutes, the supernatant was removed, and then the microrods were resuspended in saline to the desired concentration.

4.2.3. Collagen turbidity assay

First, a 1 mg/mL stock solution of collagen type I was prepared by dilution of high concentration collagen type I with phosphate buffered saline (PBS) and was subsequently kept on ice along with a 96-well plate. Varying decorin concentrations ranging from 5−80 µg/mL were then prepared by diluting 600 µg/mL stock decorin solution with PBS. Then, a 1:1 ratio of 1 mg/mL collagen type I and the decorin stocks were added to each well in triplicate resulting in final decorin doses of 2.5, 5, 10, 20, and 40 µg/mL. Absorbance measurements at 405 nm were then taken every 5 min over the span of 2 hours at ambient temperature using a plate reader. The assay also included blank controls of water and PBS as well as a control for the highest concentration of decorin.

4.2.4. Cell culture & qCPR

NIH 3T3 mouse fibroblasts (ATCC, Manassas, Virginia) were cultured in Dulbecco's modified Eagle's medium with 10% fetal calf serum and 1% penicillin/streptomycin. For experiments where free decorin was dosed, cells were seeded into 24-well plates and then media was added that either contained only 10 ng/mL TGF-β1 or 10 ng/mL TGF-β1 plus 10 μg/mL decorin. Genetic material was harvested and purified using the RNeasy Mini Kit (Qiagen, Hilden, Germany). RNA was converted into cDNA using the iScript cDNA synthesis kit (Bio-Rad Laboratories, Hercules, CA) and a Viia7 qPCR machine (Life Technologies, Carlsbad, CA) was used to measure relative expression levels of gene targets compared to the housekeeping gene 60S ribosomal protein L19 (RPL19). Expression levels of all genes were evaluated using the Fast SYBR Green Mastermix (Life Technologies, Grand Island, NY) and custom DNA primers (Integrated DNA Technologies, Coralville, IA) in triplicate for three biological replicates (Table 4.1).

4.2.5. Infarct model and microrod injections

The animal protocol for induction of MI was approved by the Committee for Animal Research of the University of California, San Francisco and was performed in accordance with the recommendations of the American Association for Accreditation of Laboratory Animal Care. The I/R MI model used in this study has been extensively tested in our labs.[88,89,180] To produce the MI model, male Sprague-Dawley rats (200–225g) underwent occlusion of the left anterior descending coronary artery for 30 minutes followed by reperfusion while under general anesthesia achieved by inhalation of 2% L/min isoflurane.[180] The chest was then closed, and the animal was allowed to

recover. The rats were randomized 3–4 days after MI to saline-injected, HA microrod-injected, decorin microrod-injected, or free decorin-injected treatment groups (Table 4.2), and were given one intramuscular injection into the heart wall under blinded conditions via ultrasound guided transthoracic injection using a 29-gauge syringe.[88,180] Each injection consisted of 50 µL of sterile 0.9% sodium chloride solution (n = 5), 50 uL of 12 ug of decorin in sodium chloride solution (n = 4), 50,000 of microrods in sodium chloride solution (n = 7), or 50,000 decorin microrods sodium chloride solution (n = 10). 75 mg/mL HA microrods were used for all microrods injections presented in this study. Each injection was delivered to the center of the infarct region and successful injection was confirmed by a slight local increase in ultrasound signal and brief thickening of the LV wall near the tip of the syringe.

4.2.6. Echocardiography

Transthoracic echocardiography was performed with a 15-MHz linear array transducer system (Vevo 2100, FUJIFILM VisualSonics, Ontario, Canada) on all animals under 2% L/min isoflurane. Echocardiography was done prior to injection on day 3 or 4 post-MI and eight weeks post-injection using standard methods that have been performed reproducibly in our lab.[88,89,203] To determine left ventricular end diastolic volume (LVEDV), left ventricular end systolic volume (LVESV), and ejection fraction (EF) at 3–4 days and eight weeks, the ventricular shadow was outlined in both systole and diastole and the single plane area length algorithmic method was applied. Two-dimensional images were obtained in both parasternal long- and short-axis views at the papillary muscle level. Stroke volume (SV) was calculated by SV = LVEDV-LVESV, while change in EF was calculated by $\Delta EF = EF_{8\ weeks} - EF_{3\text{-}4\ days}$. Transverse images

were obtained at three levels: basal (at the tip of the mitral valve leaflets), middle (at the papillary muscle level), and apical (distal to papillary muscle but before the cap of the cavity). All image analyses were performed in a blinded fashion. In cases where the ventricular shadow was not clearly identifiable in the 72–96 h or eight-week image, the heart in question was excluded from echocardiographic analyses. Cases where ejection fraction was above 45% at 3–4 days were excluded because they indicated an insufficient infarct model.

4.2.7. Histology

Sacrifice was performed after eight weeks by maintaining the animal at 5% L/min isoflurane for five minutes, followed by bilateral thoracotomy and injection of potassium chloride into the right atrium to arrest the heart in diastole. The heart was then extracted and frozen in OCT (Sakura Finetech USA, Inc., Torrance, CA) on 2-methylbutane (Sigma Aldrich, St. Louis, MO) on dry ice and sectioned for histology and image analysis. Tissue blocks were cryo-sectioned at a thickness of 10 μm starting at the apex of the left ventricle and collecting 10 serial sections every 350 μm until 100 sections were collected. Sections were stained with H&E stains and Sirius red stains using standard protocols. For immunofluorescent stains, tissue sections were air dried and blocked with 10% serum, followed by incubation with primary and secondary antibodies using standard protocols. In brief, samples were fixed in ice cold acetone for 5 min., blocked with 10% goat serum for 20 min., and incubated overnight with primary antibodies at 4°C in a solution of 0.05% Tween-20, 10% goat serum and 1% BSA in PBS (anti-sarcomeric alpha actin 1:500, alpha smooth muscle actin 1:500). After washing, secondary antibody and WGA (1:100) was added for 45 minutes at room

temperature. Hoechst (1:500) was added for 5 min at room temperature to visualize nuclei.

4.2.8. Imaging and quantification

For whole heart histology, images were taken using a Nikon 6D optical microscope (NIKON Instruments, Inc., Melville, NY) with 4–40x magnification (H&E and Sirius Red) and a Nikon spinning disc confocal microscope. Quantifications were performed using custom scripts and ImageJ.

For collagen analysis, five alternating sections of each heart were selected from throughout the coronal plane of the heart and stained with Sirius red to assess the quantity and density of collagen in the injured hearts. These sections were imaged under brightfield as well as under cross-polarized light to visualize the collagen fibers at 4x magnification. Representative images for brightfield and polarized shading corrections were taken prior to the start of each imaging session. Infarct area and intensity was quantified in the left ventricle (LV), which included the septum. Intensity measurements in the regions of interest were determined using ImageJ.

For wall thickness analysis, five measurements of across the LV free wall were recorded for each tissue section where the LV free wall was distinguishable. The average length across all available sections in a given heart sample was reported.

For cardiomyocyte cross-sectional area analysis, three sections (apex, middle, and end of the heart) per heart (n = 3 per group) were selected and stained with anti-sarcomeric alpha actinin, WGA, and Hoechst. Approximately 10-15 high-magnification

(40x) images of the remote and border zone regions in each section were analyzed to obtain the average cross-sectional area and cells per area.

For preliminary vascular density analysis, one section (middle of the heart) per heart (n = 3 per group) were selected and stained with anti-alpha-smooth muscle actin, WGA, and Hoechst. Approximately 10-15 high-magnification (40x) images of the remote, infarct, and border zone regions in each section were analyzed to obtain the number of arterioles per field.

4.2.9. Statistical analysis

All data are presented as the mean ± standard deviation unless otherwise indicated. *In vitro* analysis was performed using a student's t-tests to identify statistical differences between two groups. One-way analysis of variance (ANOVA), followed by the Tukey's multiple comparisons test was used to identify differences between three or more groups. Statistical comparisons made between groups to assess differences in EF, end systolic volume (ESV), and end diastolic volume (EDV) at 8 weeks post-MI were made using a Two-way repeated measures ANOVA followed by the Tukey's multiple comparisons test.

4.3. Results

4.3.1. Effect of decorin treatment on fibroblast gene expression and collagen fibrillogenesis

To confirm anti-fibrotic biologic effects of decorin protein, NIH 3T3 fibroblasts were stimulated with 10 ng/mL TGF-β1 and cultured in the presence or absence of 10 μg/mL decorin. Relative gene expression results from RT-qPCR using primers specified

in Table 4.1 indicate stark reductions in ACTA2, COL1A2, COL3A1, and MMP2 expression ($p < 0.0001$, $p = 0.001$, $p = 0.005$, $p = 0.026$, respectively) in decorin-treated samples compared to control (Figure 4.1A-C). These results demonstrate decorin's ability to sequester TGF-β1 and prevent activation of its downstream signaling pathways that result in myofibroblast-like phenotypes in fibroblasts.

Turbidity was used to assess the degree of collagen fibrillogenesis. A broad range of decorin concentrations were used to assess dose-dependent effects of decorin on fiber formation. It is evident that fibril formation kinetics are dependent on concentration of decorin present, and while all doses of decorin tested significantly inhibited fibrillogenesis, the highest concentration of 40 μg/mL yielded the greatest impact (Figure 4.2, $p = 0.005$).

4.3.2. Effect of decorin microrods in ischemia-reperfusion myocardial infarction in vivo models

Decorin was loaded into HA microrods to devise a more potent anti-fibrotic strategy that leveraged biophysical regulation of microstructures and the ability of decorin to sequester TGF-β1 in the post-infarct environment. Decorin loading was calculated to be approximately 12 μg of decorin per 50,000 microrods and, as such, this was used to justify the chosen injection dose for the free decorin treatment group in subsequent animal studies (Table 4.2). A rodent model of ischemia-reperfusion myocardial infarction was utilized to generate a cardiac fibrosis model. All treatments– saline, HA microrods, decorin microrods, or free decorin were delivered into the infarct via ultrasound-guided, intramyocardial injection.

HA microrod and decorin microrod treatment were shown to result in significant improvements in cardiac function (Figure 4.3). The change in EF was assessed by taking the difference in EF measured at Day 3-4 post-MI and at Day 56 post-MI (Figure 4.3A). Rats treated with HA microrods (3.98% ± 3.47%) and decorin microrods (4.89% ± 5.39%) exhibited significantly improved change in EF after 56 days compared to rats treated with saline (-4.18% ± 2.78%) and free decorin (-3.42% ± 1.86%). Since decorin microrods performed better than HA microrods and free decorin, this suggests that the ability to locally retain decorin at the infarct site through the use of the microstructures was crucial to improving the efficacy of the microrod strategy. Decorin microrods also demonstrated a significant increase in EF at 56 days post-MI compared to free decorin (Figure 4.3B, $p = 0.007$). In addition to benefits observed in cardiac performance, ventricular remodeling was also improved in rats treated with decorin microrods as evidenced by significant reduction in ESV and EDV compared to rats treated with saline, HA microrod, and free decorin (Figure 4.4A-B). Additionally, both HA microrods and decorin microrods exhibit trends in improved change in stroke volume compared to saline and free decorin treatments after 56 days post-MI (Figure 4.5).

Histological evaluation of each treatment group was performed using H&E staining and Sirius red staining to assess LV wall thickness and degree of fibrosis (Figure 4.6). Wall thickness measurements were performed on five sections throughout the coronal plane of the heart where the LV cavity was distinguishable. Animals treated with decorin microrods (2154 ± 356 μm) exhibited trends in having greater LV wall thickness compared to those treated with saline (1791 ± 401 μm) and free decorin (1574 ± 210 μm) as seen in Figure 4.7. Collagen fibrosis was assessed by quantifying

the average intensity of Sirius red staining in the LV of 5 sections throughout each heart under cross-polarized imaging. Rats treated with no MI ($p = 0.02$) and those treated with HA microrods ($p = 0.029$) and decorin microrods ($p = 0.015$) all had significantly reduced intensity of collagen staining in the LV compared to those treated with saline (Figure 4.8).

We also investigated the impact of decorin microrods on cardiomyocyte and endothelial cell behaviors. Given that microrods were observed to be retained in the cardiac tissue for at least 8 weeks (Figure 4.9), we hypothesized that there could be additional long-term benefits bestowed by the presence of these structures. A crucial compensatory mechanism after myocardial injury is hypertrophic growth of cardiomyocytes.[40] Hypertrophy was assessed by immunofluorescence staining for sarcomeric alpha actinin, WGA (cell membrane), and nuclei in the border zone and remote zone (Figure 4.10A). Three sections from throughout the heart were assessed (n = 3 animals per group). While no differences in cardiomyocyte area were observed between groups in the border zone, a significant reduction in cardiomyocyte area in the remote zone was identified in decorin microrod ($p = 0.005$) and free decorin-treated ($p = 0.003$) animals compared to saline-treated animals (Figure 4.10B-C). Accordingly, we observed an increase in cardiomyocytes per area in the remote zone for decorin microrod ($p < 0.0001$) and free decorin ($p = 0.007$) groups compared to saline animals (Figure 4.10D-E). Preliminary experiments were performed to identify if an increase in vascular density was also responsible for the observed improvements in cardiac function brought about by decorin microrod treatment. Arteriole number was assessed by immunofluorescence staining for alpha smooth muscle actin, WGA, and nuclei in the

infarct, border zone, and remote zone (Figure 4.11A). In initial experiments, one section taken from the middle of each heart was analyzed (n = 3 animals per group). Based on initial results, after 56 days post-MI there do not appear to be significant differences in arteriole number between saline and decorin microrod groups in any region (Figure 4.11B-D). However, limited sample size may be responsible being unable to identify differences and so further experimentation is required to assess potential vascular differences more accurately.

4.4. Discussion

In this work, we investigated the capacity for HA microrods to locally deliver decorin protein to the infarct and modulate the post-infarct environment to dampen pathophysiological responses that occur post-MI. Our results demonstrate that decorin microrods can significantly improve cardiac function and attenuate deleterious ventricular dilatation, cardiac fibrosis, and hypertrophy in chronic models of ischemia-reperfusion MI.

An emerging paradigm in therapeutic biomaterials research focuses on leveraging the mechanosensing machinery of cells to elicit specific phenotypes and behaviors. The ability to reliably dictate cellular responses can be a powerful tool in addressing pathological responses that result from clinical diseases, such as heart failure.[226] While injections of bulk polymers may provide the myocardium with mechanical support to improve cardiac function and delay LV dilatation, biophysical regulation via micro and nanostructure cues can lead to reprogramming of resident cells to create microenvironments that are more amenable to tissue repair and

regeneration.[19] Our lab has previously shown the utility of high aspect ratio structures made from polypropylene and polyethylene glycol (PEG) to discourage myofibroblast transition.[89,171] However, developing therapeutic strategies should aim to employ materials that have biocompatibility, exhibit biodegradation, and possess tunable properties for facile translation to the clinic. As such, next generation microrods were fabricated from HA, a naturally occurring polysaccharide that is implicated in wound healing responses.[173–175] HA microrods were shown to outperform other materials in attenuating fibrotic response in vitro and in improving cardiac function in in vivo models of ischemia-reperfusion MI.[88] These observed benefits are likely due to additional biochemical effects bestowed by the HA material itself.

Not only do polymeric microrods have the capacity to modulate fibroblast behaviors through mechanical regulation, but they can be formulated to release bioactive factors. We have successfully utilized PEG microrods to locally deliver E-domain peptide and β-NGF to injured tissue in myocardial infarction and tibial fracture models.[101,232] To enhance efficacy of our microrod platform for applications in post-MI therapy, we investigated the ability for HA microrods to locally deliver decorin, a SLRP with both antifibrotic and antioxidant attributes. The core protein of decorin has two binding sites for TGF-β1 as well as binds collagen through its leucine rich repeat region.[253,254] Several studies have implicated decorin in playing an important role in post-infarct remodeling and others have demonstrated how decorin treatment can mitigate adverse outcomes in various models of cardiovascular disease.[34,255–258]

The results from our recently completed *in vivo* experiments support these observations about decorin's ability to improve cardiovascular outcomes after injury.

Similar to results we've published previously, HA microrods showed improved change in ejection fraction after 56 days post-MI (3.98% ± 3.47%). However, decorin microrods (4.89% ± 5.39%) exhibited the greatest improvement in cardiac function compared to all other groups, including saline (-4.18% ± 2.78%) and free decorin (-3.42% ± 1.86%). The fact that decorin microrods performed better than HA microrods and free decorin individually, points to the importance of the decorin being retained in the infarct region by the microrods to achieve the synergistic therapeutic effects from the combination strategy (Figure 4.3). The improvements in cardiac function observed in both HA microrod and decorin microrod groups may likely be due to reduced LV wall stress due to the mechanical support provided by the polymer injection. This is in line with what was observed in other studies where LV function improved in response to reduced LV volume and wall stress due to increased LV wall thickness resulting from biopolymer injection.[259] Similarly, in our study decorin microrods showed a trend towards increased average LV wall thickness compared to saline and free decorin groups whereas HA microrods only showed a trend for increased LV wall thickness compared to the free decorin group (Figure 4.7).

Interestingly, while both decorin microrod and free decorin groups had decreased fibrosis and cardiomyocyte hypertrophy compared to saline (Figure 4.8), only rats treated with decorin microrods exhibited improved cardiac function and ventricular remodeling outcomes (Figure 4.4). Decorin's role in reducing cardiac hypertrophy has only recently been elucidated. Yan *et al* reported that decorin decreases hypertrophic growth by regulating the Calcium/calmodulin-dependent protein kinase II (CaMKII)/myocyte enhancer factor 2 (MEF-2) signaling pathway to inhibit transcription

of MEF-2.[260] This observation is in accordance with our data that demonstrated both groups that were treated with decorin had decreased cardiomyocyte hypertrophy in the remote region (Figure 4.10). Given the differences in therapeutic outcomes regarding ejection fraction and LV volumes after 56 days post-MI between the two decorin groups, it is evident that the presence of microrods is responsible for the discrepancy in treatment efficacy. By identifying the relevant pathways and physiological responses that are affected by these microstructures, it will be possible to optimize this therapeutic strategy to achieve more holistic myocardial repair after injury. In conclusion, the use of decorin microrods represents a promising and novel translational strategy for cardiac treatment after MI.

Table 4.1. Primers used for qPCR.

Target Gene	Forward Primer (5' -> 3')	Reverse Primer (5' -> 3')
RPL19	CATTTTGCCCGACGAAAGGG	GATCTGCTGACGGGAGTTGG
ACTA2	GCTGCTCCAGCTATGTGTGA	CCATTCCAACCATTACTCCCTGA
COL1A2	AAGGGTGCTACTGGACTCCC	TTGTTACCGGATTCTCCTTTGG
COL3A1	CTGTAACATGGAAACTGGGGAAA	CCATAGCTGAACTGAAAACCACC
TGFB1	GGACTCTCCACCTGCAAGAC	CTGGCGAGCCTTAGTTTGGA
TGFBR2	ACGTTCCCAAGTCGGATGTG	TGTCGCAAGTGGACAGTCTC
SMAD3	AAGGCGACACATTGGGAGAG	GGGCAGCAAATTCCTGGTTG
MMP2	CAAGTTCCCCGGCGA TGTC	TTCTGGTCAAGGTCACCTGTC
MMP9	GGACCCGAAGCGGACATTG	CGTCGTCGAAATGGGCATCT
YAP1	TACTGATGCAGGTACTGCGG	TCAGGGATCTCAAAGGAGGAC
NOS2	GAGACAGGGAAGTCTGAAGCAC	CCAGCAGTAGTTGCTCCTCTTC
TNFA	TGGAACTGGCAGAAGAGG	AGACAGAAGAGCGTGGTG

Table 4.2. Experimental injection groups.

Treatment Group	Agent
No MI	None
MI + Vehicle	50 µL of 0.9% sodium chloride solution
MI + HA microrods	50 µL of 50,000 HA microrods in 0.9% sodium chloride solution
MI + Decorin microrods	50 µL of 50,000 decorin-loaded (12 µg) decorin microrods in 0.9% sodium chloride solution
MI + Free Decorin	50 µL of 12 µg decorin in 0.9% sodium chloride solution

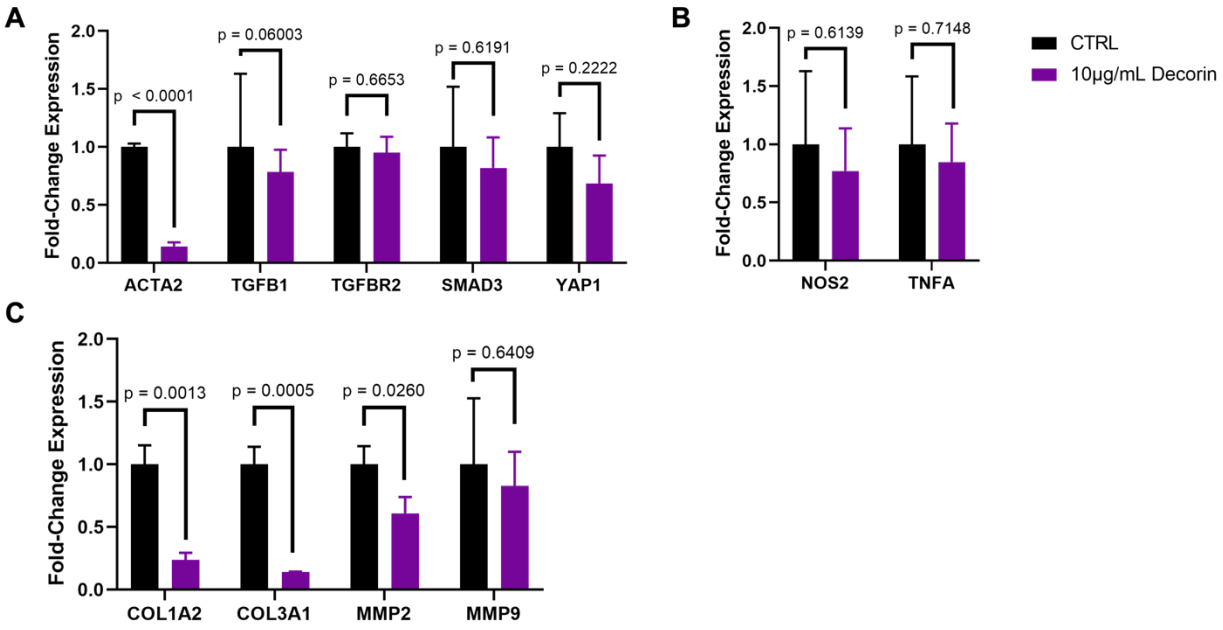

Figure 4.1. Decorin decreases expression of fibrotic markers. Relative fold-change expression of genes pertaining to (A) TGF-β cascade, (B) inflammation, and (C) extracellular matrix after NIH 3T3 fibroblasts stimulated with 10 ng/mL TGF-β1 were treated with 10 µg/mL decorin protein. Significant reduction in gene expression of ACTA2, COL1A2, COL3A1, and MMP2 were observed due to decorin treatment. The data are presented as the mean ± SD.

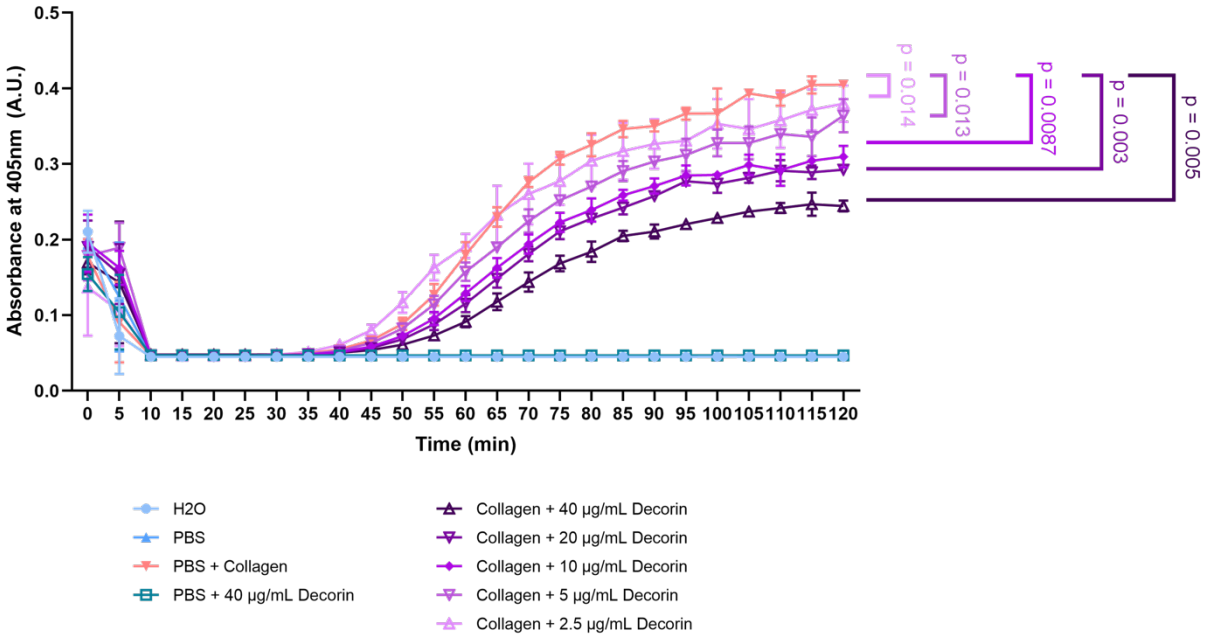

Figure 4.2. Decorin decreases collagen fibril formation. Collagen fibrillization was decreased in a dose-dependent manner corresponding to the concentration of decorin protein administered. The data are presented as the mean ± SD.

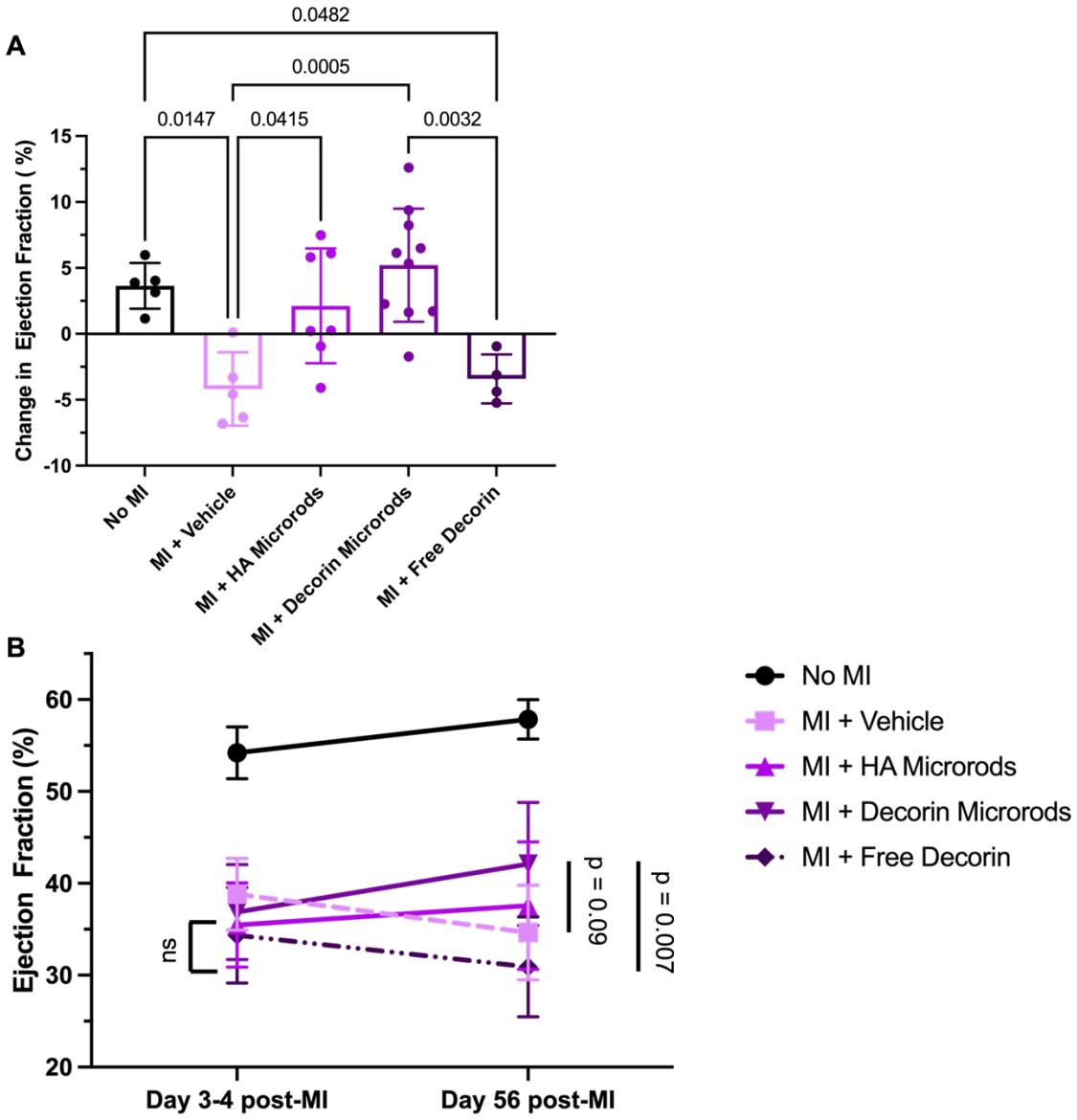

Figure 4.3. Treatment with decorin microrods improves ejection fraction. (A) Echocardiography was used to compare ejection fraction (EF) at 3-4 days after infarct and at 56 days after infarct in rats that had no MI performed (n = 5) and rats with MI that were treated with saline (n = 5), HA microrods (n = 7), decorin microrods (n = 10), and free decorin (n = 4). Rats treated with decorin microrods and HA microrods had a significantly higher change in EF compared to saline-treated animals. Rats treated with decorin microrods also had a significantly higher change in EF compared to those treated with free decorin. (B) The average EF for each group is plotted at Day 3-4 post-MI and at Day 56 post-MI. At Day 56, rats treated with decorin microrods had higher average EF compared to rats treated with saline and free decorin. The data are presented as the mean ± SD.

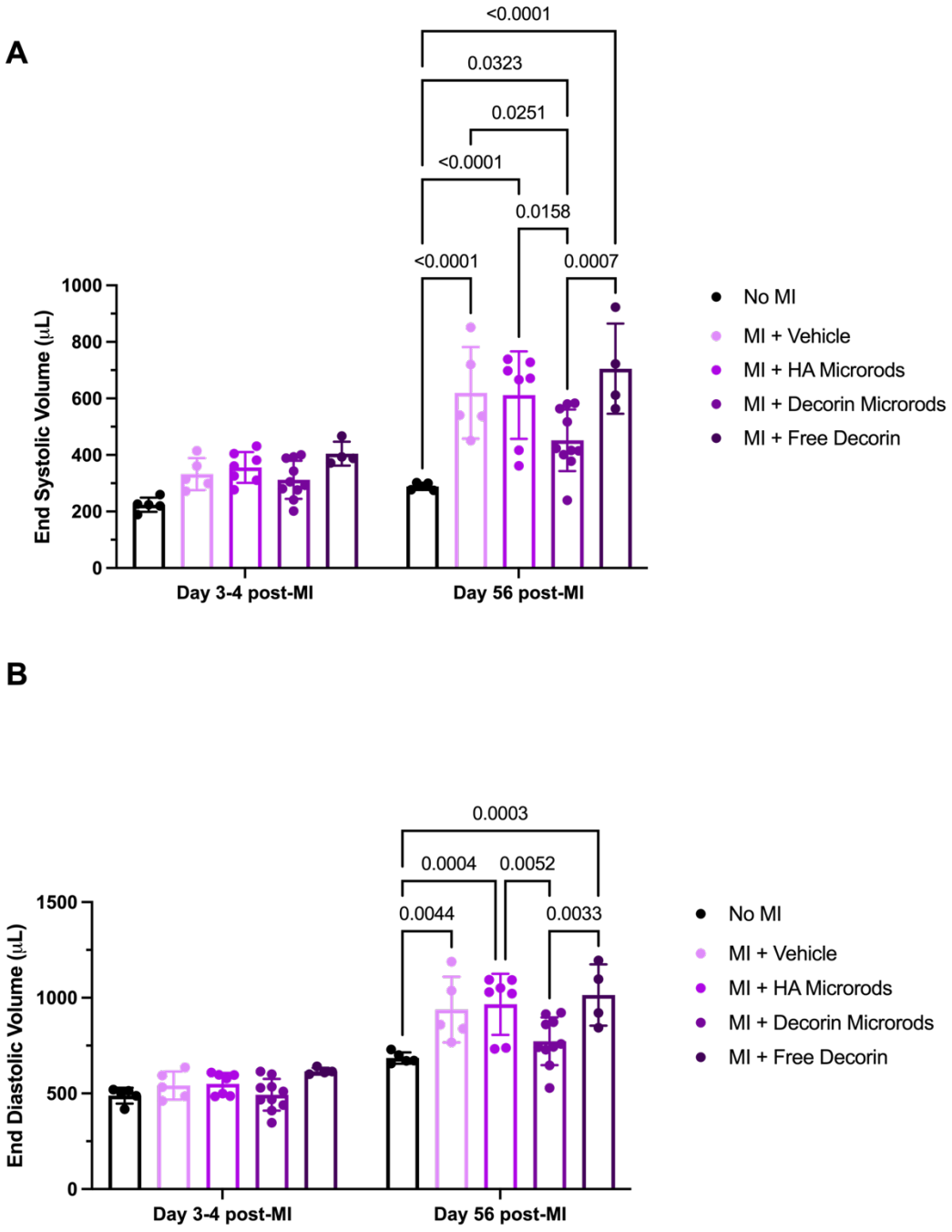

Figure 4.4. Treatment with decorin microrods reduces maladaptive ventricular remodeling. Echocardiography was used to evaluate (A) end systolic volume and (B) end diastolic volume at 3-4 days after infarct and at 56 days after infarct in rats that had no MI performed (n = 5) and rats with MI that were treated with saline (n = 5), HA microrods (n = 7), decorin microrods (n = 10), and free decorin (n = 4). End systolic volume and end diastolic volume were reduced in rats treated with decorin microrods compared to rats treated with saline, HA microrods, and free decorin. The data are presented as the mean ± SD.

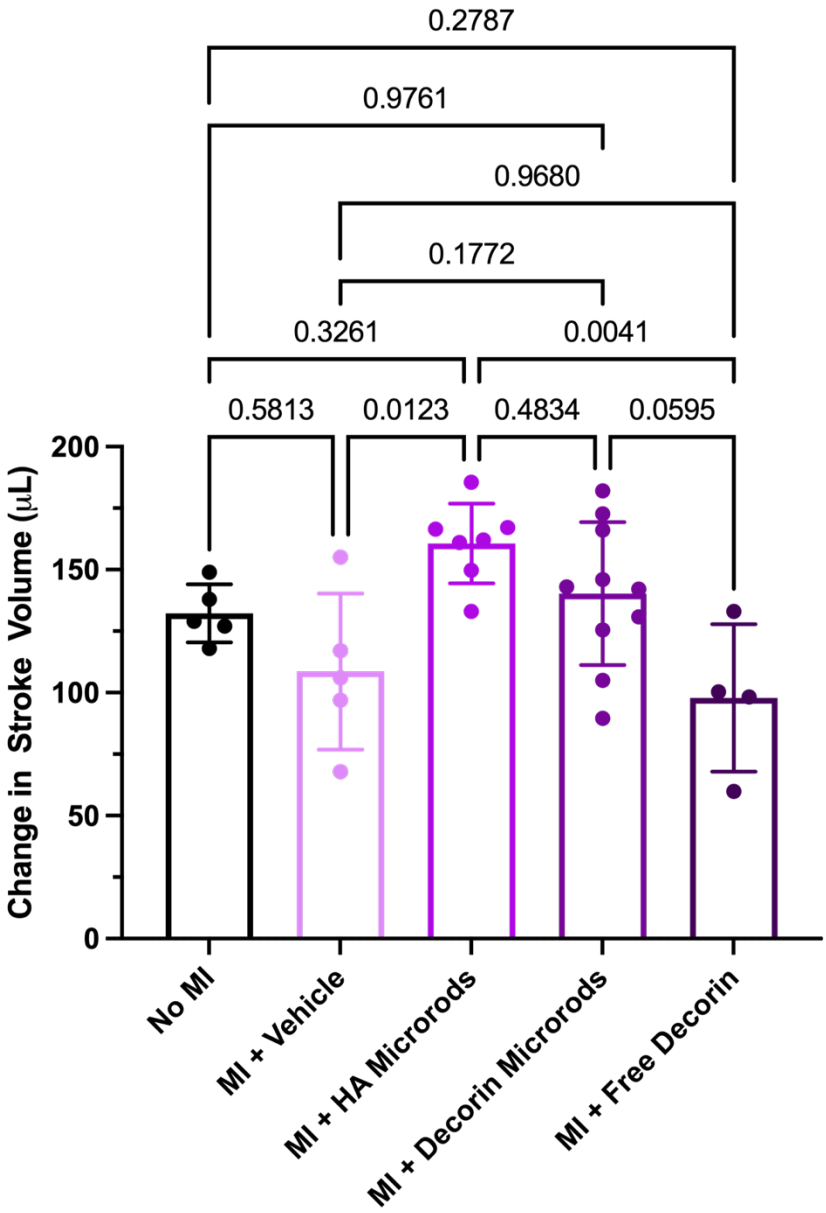

Figure 4.5. Treatment with microrods improves stroke volume after 56 days post-MI. Echocardiography was used to evaluate stroke volume at 3-4 days after infarct and at 56 days after infarct in rats that had no MI performed (n = 5) and rats with MI that were treated with saline (n = 5), HA microrods (n = 7), decorin microrods (n = 10), and free decorin (n = 4). Both treatment with HA microrods and decorin microrods exhibited trends in improved change in stroke volume compared to saline and free decorin treatments. The data are presented as the mean ± SD.

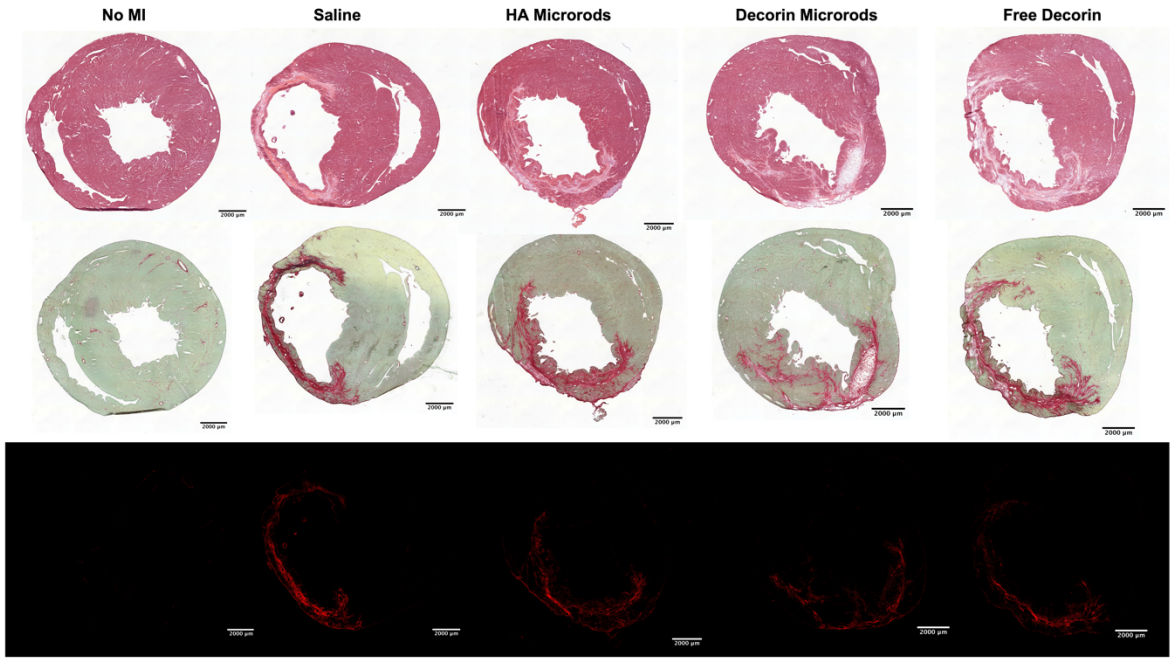

Figure 4.6. Morphological comparison of the various treatment groups. Histological evaluation of each treatment group was performed using H&E staining (top) and Sirius red staining (brightfield: middle, cross-polarized: bottom). Scale bars = 2000 μm.

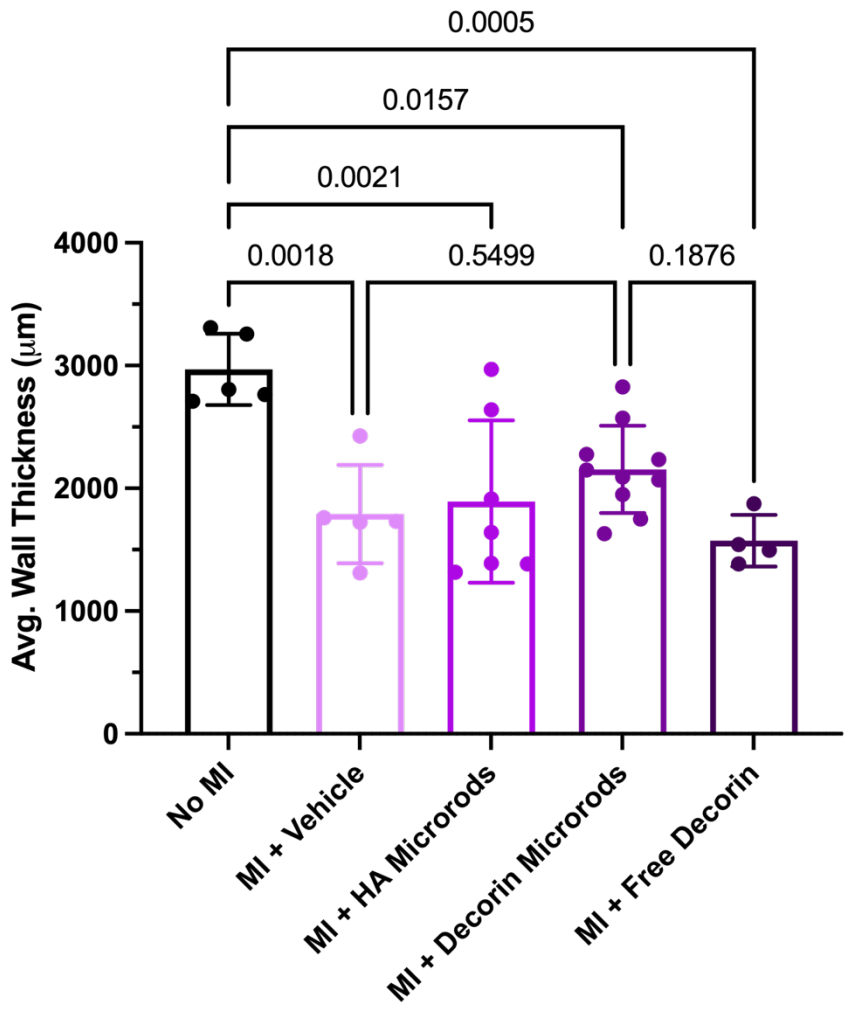

Figure 4.7. LV wall thickness comparison between the various treatment groups. The average wall thickness was assessed by measuring 5 different regions that were equally spaced throughout the LV free wall. Rats treated with decorin microrods showed a trend towards increased LV wall thickness compared to other treatment groups. The data are presented as the mean ± SD.

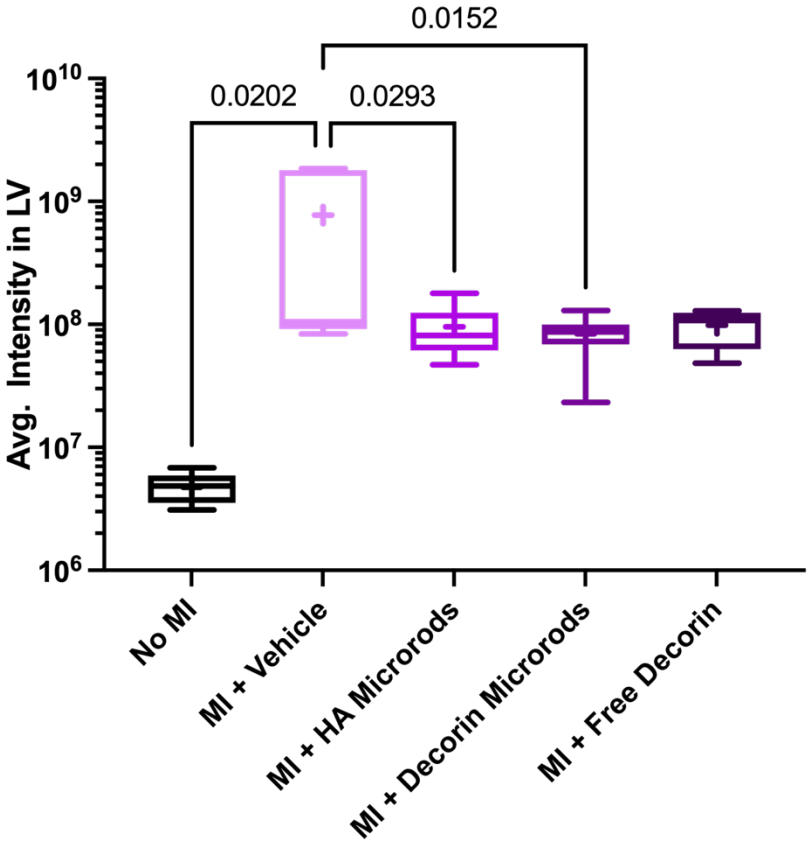

Figure 4.8. Treatment with HA microrods, decorin microrods, and free decorin decrease collagen in the left ventricle post-MI. Tissue sections were stained with Sirius red stain and visualized under cross-polarized light. Intensity of collagen staining in the left ventricle was measured. Treatment with HA microrods, decorin microrods, and free decorin have reduced degree of fibrosis in the left ventricle compared to saline treatment. The data are presented as the mean ± SD.

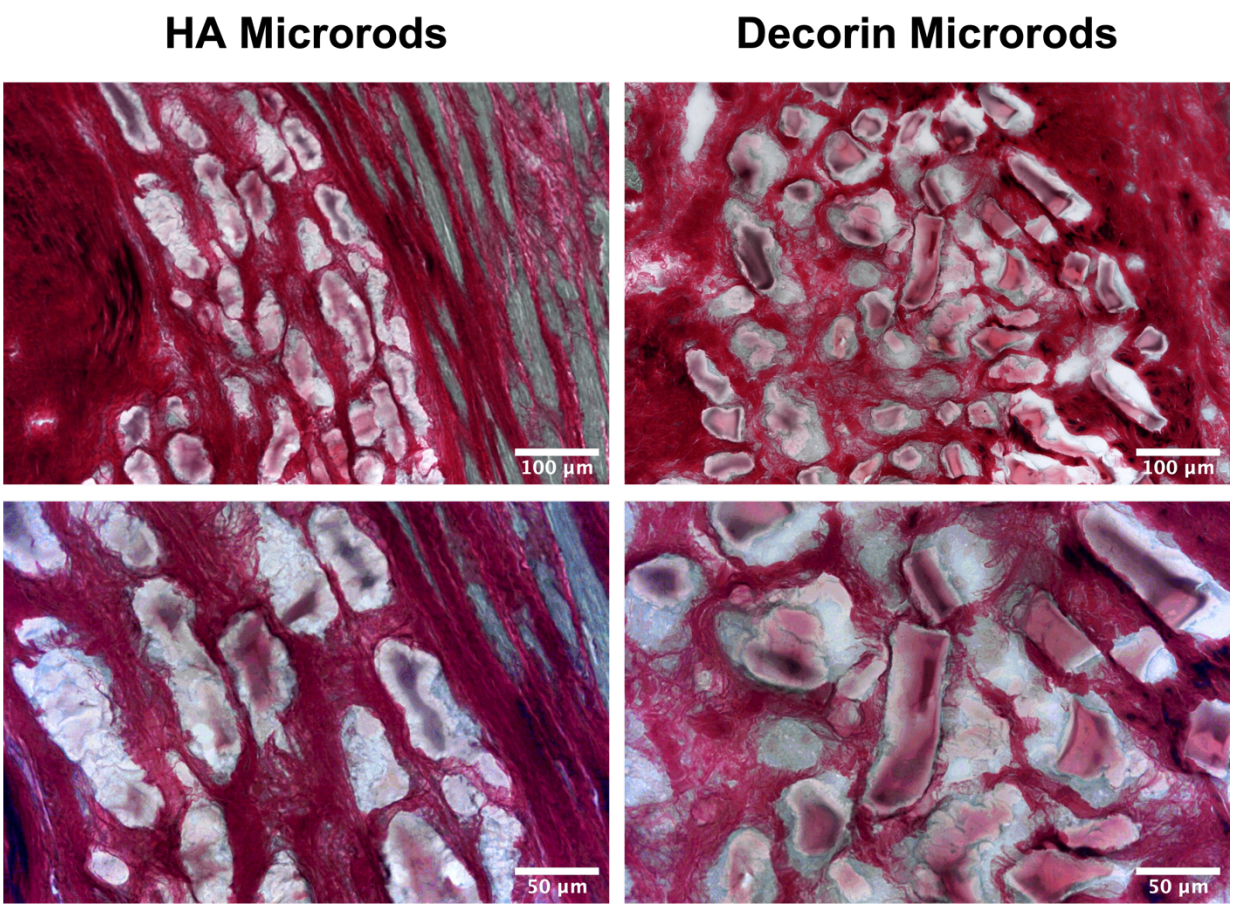

Figure 4.9. Microrods remain in cardiac tissue for 8 weeks after injection. Microscopy revealed that HA microrods and decorin microrods were still present in cardiac tissue after 8 weeks (20x magnification: top, 40x magnification: bottom). Scale bars = 100 µm (top) and 50 µm (bottom).

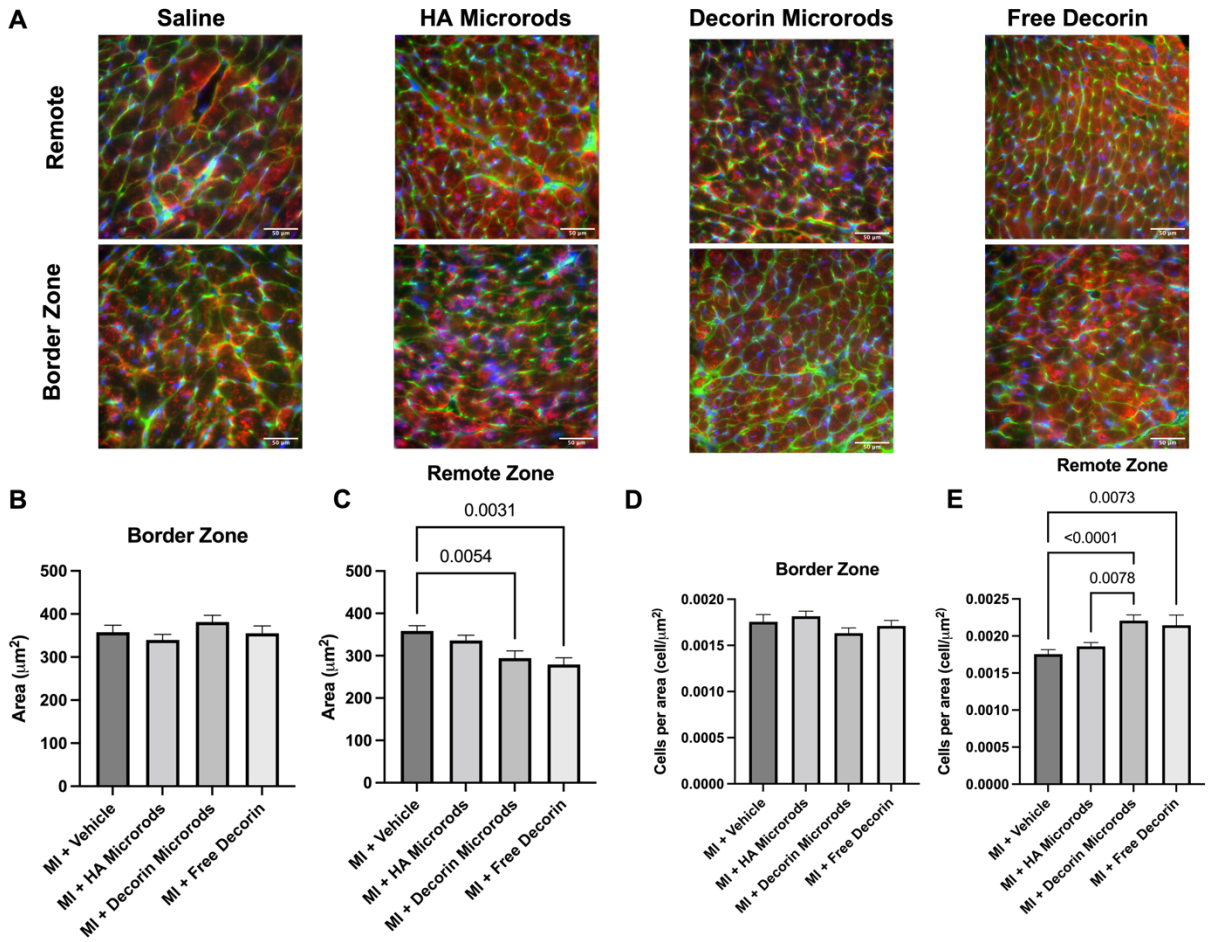

Figure 4.10. Treatment with decorin microrods and free decorin decrease cardiomyocyte hypertrophy post-MI. (A) Immunofluorescence staining for sarcomeric alpha actinin (red), wheat germ agglutinin (green), and nuclei (blue) was performed to identify cardiomyocytes. Scale bars = 50 μm. Tissue sections were quantified for (B-C) cardiomyocyte area and (D-E) cell number in the border zone and remote zone. Rats treated with decorin microrods and free decorin exhibited decreased cardiomyocyte area and increased cardiomyocyte number compared to rats treated with saline (n = 3 for all groups). The data are presented as the mean ± SD.

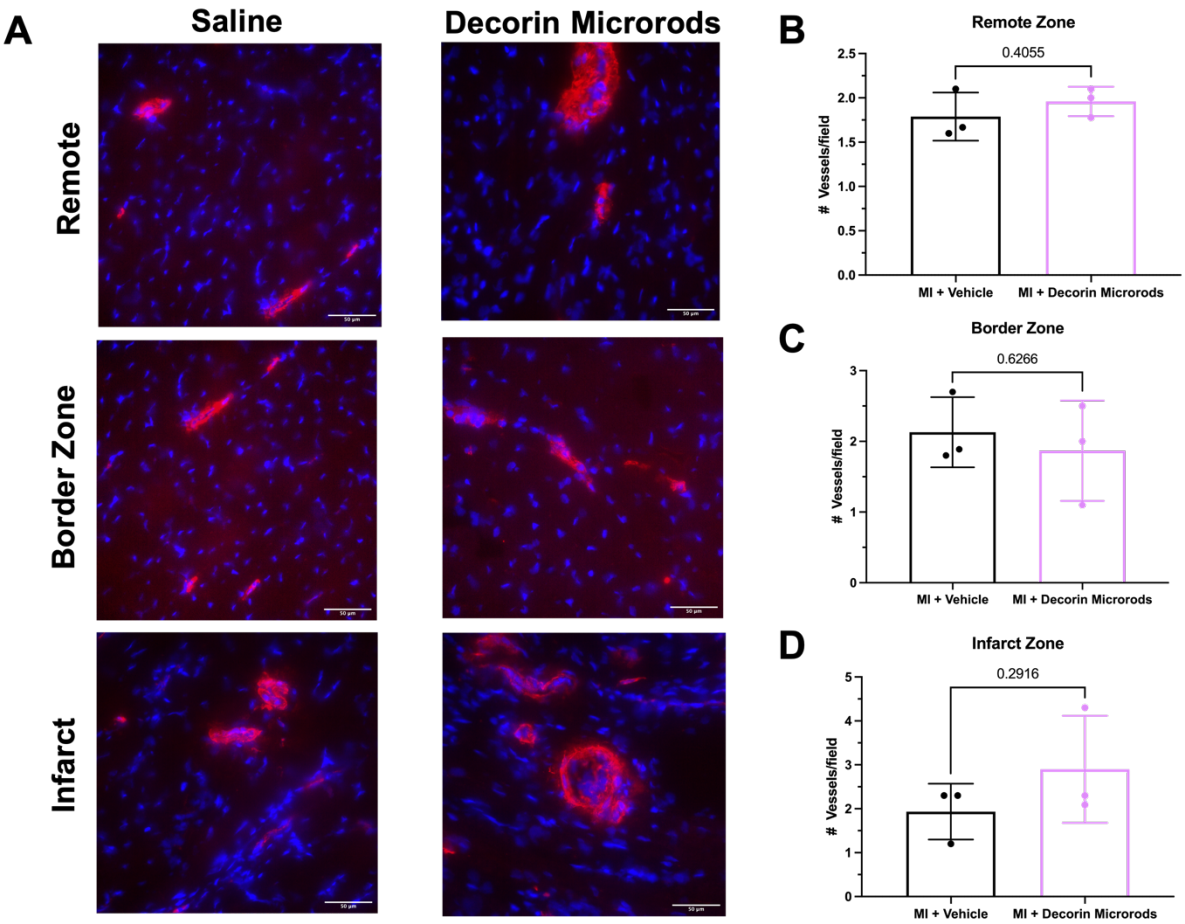

Figure 4.11. Preliminary results show that treatment with decorin microrods do not significantly improve vascularization post-MI. (A) Immunofluorescence staining for alpha smooth muscle actin (red) and nuclei (blue) was performed to identify arterioles. Scale bars = 50 μm. Tissue sections were quantified for arteriole number in the infarct, border zone, and remote zone. The number of arterioles observed in each of these regions did not appear different between rats treated with saline and decorin microrods (n = 3). The data are presented as the mean ± SD.

References

1. Mendis, S. *et al. Global status report on noncommunicable diseases 2014. World Health Organisation. World Health* (2014) doi:ISBN 9789241564854.
2. Bloom, D.E., Cafiero, E.T., Jané-Llopis, E., Abrahams-Gessel, S., Bloom, L.R., Fathima, S., Feigl, A.B., Gaziano, T., Mowafi, M., Pandya, A., Prettner, K., Rosenberg, L., Seligman, B., Stein, A.Z., & Weinstein, C. The Global Economic Burden of Noncommunicable Diseases. *Geneva World Econ. Forum* (2011).
3. Mendis, S., Puska, P. & Norrving, B. Global atlas on cardiovascular disease prevention and control. *World Heal. Organ.* (2011).
4. Lee, Y. & Gustafsson, Å. B. Role of apoptosis in cardiovascular disease. *Apoptosis* (2009) doi:10.1007/s10495-008-0302-x.
5. Ruparelia, N., Chai, J. T., Fisher, E. A. & Choudhury, R. P. Inflammatory processes in cardiovascular disease: A route to targeted therapies. *Nature Reviews Cardiology* (2017) doi:10.1038/nrcardio.2016.185.
6. Unger, T. The role of the renin-angiotensin system in the development of cardiovascular disease. in *American Journal of Cardiology* (2002). doi:10.1016/S0002-9149(01)02321-9.
7. Khan, R. & Sheppard, R. Fibrosis in heart disease: Understanding the role of transforming growth factor-β1 in cardiomyopathy, valvular disease and arrhythmia. *Immunology* (2006) doi:10.1111/j.1365-2567.2006.02336.x.
8. Zhang, M., Wang, B., Kent, K. C. & Guo, L.-W. Vascular Fibrosis and Disease. in 369–386 (Humana Press, Cham, 2019). doi:10.1007/978-3-319-98143-7_14.

9. Widmer, R. J. & Lerman, A. Endothelial dysfunction and cardiovascular disease. doi:10.5339/gcsp.2014.43.

10. Khurana, R., Simons, M., Martin, J. F. & Zachary, I. C. Role of angiogenesis in cardiovascular disease: A critical appraisal. *Circulation* vol. 112 1813–1824 (2005).

11. Kramer, C. M. *et al.* Regional myocyte hypertrophy parallels regional myocardial dysfunction during post-infarct remodeling. *J. Mol. Cell. Cardiol.* (1998) doi:10.1006/jmcc.1998.0741.

12. Kayar, S. R. & Weiss, H. R. Diffusion distances, total capillary length and mitochondrial volume in pressure-overload myocardial hypertrophy. *J. Mol. Cell. Cardiol.* (1992) doi:10.1016/0022-2828(92)93179-N.

13. Seiden, D., Navidad, P. & Weiss, H. R. Oxygen diffusion distance in thyroxine-induced hypertrophic rabbit myocardium. *J. Mol. Cell. Cardiol.* (1988) doi:10.1016/S0022-2828(88)80146-9.

14. Chaturvedi, R. R. *et al.* Patterning vascular networks in vivo for tissue engineering applications. *Tissue Eng. - Part C Methods* (2015) doi:10.1089/ten.tec.2014.0258.

15. Simons, M. *et al.* Pharmacological treatment of coronary artery disease with recombinant fibroblast growth factor-2: Double-blind, randomized, controlled clinical trial. *Circulation* **105**, 788–793 (2002).

16. Henry, T. D. *et al.* The VIVA trial: Vascular endothelial growth factor in ischemia for vascular angiogenesis. *Circulation* **107**, 1359–1365 (2003).

17. Wu, T. *et al.* Minimal Evidence of Transdifferentiation from Recipient Bone Marrow to Parenchymal Cells in Regenerating and Long-Surviving Human

Allografts. *Am. J. Transplant.* **3**, 1173–1181 (2003).

18. Tang, X. L. *et al.* Long-Term Outcome of Administration of c-kitPOS Cardiac Progenitor Cells after Acute Myocardial Infarction: Transplanted Cells Do not Become Cardiomyocytes, but Structural and Functional Improvement and Proliferation of Endogenous Cells Persist for at Least One Year. *Circ. Res.* **118**, 1091–1105 (2016).
19. Le, L. V., Mkrtschjan, M. A., Russell, B. & Desai, T. A. Hang on tight: reprogramming the cell with microstructural cues. *Biomed. Microdevices* (2019) doi:10.1007/s10544-019-0394-9.
20. Wang, T., Nanda, S. S., Papaefthymiou, G. C. & Yi, D. K. Mechanophysical Cues in Extracellular Matrix Regulation of Cell Behavior. *ChemBioChem* (2020) doi:10.1002/cbic.201900686.
21. Borg, T. K. & Caulfield, J. B. The collagen matrix of the heart. *Fed. Proc.* (1981).
22. Robinson, T. F., Geraci, M. A., Sonnenblick, E. H. & Factor, S. M. *Coiled Perimysial Fibers of Papillary Muscle in Rat Heart: Morphology, Distribution, and Changes in Configuration*. http://ahajournals.org.
23. Wang, B. *et al.* Structural and biomechanical characterizations of porcine myocardial extracellular matrix. *J. Mater. Sci. Mater. Med.* **23**, 1835–1847 (2012).
24. Liliensiek, S. J., Nealey, P. & Murphy, C. J. Characterization of endothelial basement membrane nanotopography in rhesus macaque as a guide for vessel tissue engineering. *Tissue Eng. Part A* **15**, 2643–2651 (2009).
25. Flemming, R. G., Murphy, C. J., Abrams, G. A., Goodman, S. L. & Nealey, P. F. Effects of synthetic micro- and nano-structured surfaces on cell behavior.

Biomaterials **20**, 573–588 (1999).

26. Al-Haque, S. *et al.* Hydrogel Substrate Stiffness and Topography Interact to Induce Contact Guidance in Cardiac Fibroblasts. *Macromol. Biosci.* **12**, 1342–1353 (2012).
27. Bettinger, C. J., Langer, R. & Borenstein, J. T. 'Engineering Substrate Micro-and Nanotopography to Control Cell Function' Lead-In. doi:10.1002/anie.200805179.
28. Ermis, M., Antmen, E. & Hasirci, V. Micro and Nanofabrication methods to control cell-substrate interactions and cell behavior: A review from the tissue engineering perspective. *Bioactive Materials* vol. 3 355–369 (2018).
29. Zhang, Y., Gordon, A., Qian, W. & Chen, W. Engineering Nanoscale Stem Cell Niche: Direct Stem Cell Behavior at Cell-Matrix Interface. *Adv. Healthc. Mater.* **4**, 1900–1914 (2015).
30. De Mel, A., Cousins, B. G. & Seifalian, A. M. Surface modification of biomaterials: A quest for blood compatibility. *International Journal of Biomaterials* (2012) doi:10.1155/2012/707863.
31. Xu, L. C., Bauer, J. W. & Siedlecki, C. A. Proteins, platelets, and blood coagulation at biomaterial interfaces. *Colloids Surfaces B Biointerfaces* (2014) doi:10.1016/j.colsurfb.2014.09.040.
32. Banerjee, M. N., Bolli, R. & Hare, J. M. Clinical Studies of Cell Therapy in Cardiovascular Medicine. *Circ. Res.* **123**, 266–287 (2018).
33. Segers, V. F. M. & Lee, R. T. Biomaterials to enhance stem cell function in the heart. *Circ. Res.* **109**, 910–922 (2011).
34. Li, L. *et al.* Postinfarction gene therapy with adenoviral vector expressing decorin

mitigates cardiac remodeling and dysfunction. *Am. J. Physiol. - Hear. Circ. Physiol.* **297**, 1504–1513 (2009).

35. Padin-Iruega, M. E. *et al.* Cardiac progenitor cells and biotinylated insulin-like growth factor-1 nanofibers improve endogenous and exogenous myocardial regeneration after infarction. *Circulation* **120**, 876–887 (2009).
36. Yang, H. *et al.* An in Vivo miRNA Delivery System for Restoring Infarcted Myocardium. *ACS Nano* **13**, 9880–9894 (2019).
37. Chen, H. S. V., Kim, C. & Mercola, M. Electrophysiological challenges of cell-based myocardial repair. *Circulation* (2009) doi:10.1161/CIRCULATIONAHA.107.751412.
38. Fukushima, S. *et al.* Direct intramyocardial but not intracoronary injection of bone marrow cells induces ventricular arrhythmias in a rat chronic ischemic heart failure model. *Circulation* (2007) doi:10.1161/CIRCULATIONAHA.106.662577.
39. Gerdes, A. M. *et al.* Structural remodeling of cardiac myocytes in patients with ischemic cardiomyopathy. *Circulation* (1992) doi:10.1161/01.CIR.86.2.426.
40. Gerdes, A. M. & Capasso, J. M. Structural remodeling and mechanical dysfunction of cardiac myocytes in heart failure. *Journal of Molecular and Cellular Cardiology* (1995) doi:10.1016/0022-2828(95)90000-4.
41. Sanger, J. W. *et al.* Assembly of myofibrils in cardiac muscle cells. in *Advances in Experimental Medicine and Biology* (2000). doi:10.1007/978-1-4615-4267-4_6.
42. Fromaget, C., Aoumari, A. El & Gros, D. Distribution pattern of connexin 43, a gap junctional protein, during the differentiation of mouse heart myocytes. *Differentiation* **51**, 9–20 (1992).

43. Peters, N. S. *et al.* Spatiotemporal relation between gap junctions and fascia adherens junctions during postnatal development of human ventricular myocardium. *Circulation* (1994) doi:10.1161/01.CIR.90.2.713.

44. Mengsteab, P. Y. *et al.* Spatiotemporal control of cardiac anisotropy using dynamic nanotopographic cues. *Biomaterials* (2016) doi:10.1016/j.biomaterials.2016.01.062.

45. Sun, S. *et al.* Progressive Myofibril Reorganization of Human Cardiomyocytes on a Dynamic Nanotopographic Substrate. *ACS Appl. Mater. Interfaces* (2020) doi:10.1021/acsami.0c03464.

46. Salick, M. R. *et al.* Micropattern width dependent sarcomere development in human ESC-derived cardiomyocytes. *Biomaterials* (2014) doi:10.1016/j.biomaterials.2014.02.001.

47. Carson, D. *et al.* Nanotopography-Induced Structural Anisotropy and Sarcomere Development in Human Cardiomyocytes Derived from Induced Pluripotent Stem Cells. *ACS Applied Materials and Interfaces* (2016) doi:10.1021/acsami.5b11671.

48. Hanft, L. M., Korte, F. S. & McDonald, K. S. Cardiac function and modulation of sarcomeric function by length. *Cardiovascular Research* (2008) doi:10.1093/cvr/cvm099.

49. Lundy, S. D., Zhu, W. Z., Regnier, M. & Laflamme, M. A. Structural and functional maturation of cardiomyocytes derived from human pluripotent stem cells. *Stem Cells Dev.* (2013) doi:10.1089/scd.2012.0490.

50. Castilho, M. *et al.* Melt Electrowriting Allows Tailored Microstructural and Mechanical Design of Scaffolds to Advance Functional Human Myocardial Tissue

Formation. *Adv. Funct. Mater.* (2018) doi:10.1002/adfm.201803151.

51. Lin, Y. D. *et al.* A nanopatterned cell-seeded cardiac patch prevents electro-uncoupling and improves the therapeutic efficacy of cardiac repair. *Biomater. Sci.* (2014) doi:10.1039/c3bm60289c.

52. Tsui, J. H. *et al.* Conductive silk-polypyrrole composite scaffolds with bioinspired nanotopographic cues for cardiac tissue engineering. *J. Mater. Chem. B* (2018) doi:10.1039/C8TB01116H.

53. Wu, Y., Wang, L., Guo, B. & Ma, P. X. Interwoven Aligned Conductive Nanofiber Yarn/Hydrogel Composite Scaffolds for Engineered 3D Cardiac Anisotropy. *ACS Nano* (2017) doi:10.1021/acsnano.7b01062.

54. Ma, Z. *et al.* Three-dimensional filamentous human diseased cardiac tissue model. *Biomaterials* (2014) doi:10.1016/j.biomaterials.2013.10.052.

55. Hesketh, G. G. *et al.* Ultrastructure and regulation of lateralized connexin43 in the failing heart. *Circ. Res.* **106**, 1153–1163 (2010).

56. Xiao, Y. *et al.* Microfabricated perfusable cardiac biowire: A platform that mimics native cardiac bundle. *Lab Chip* (2014) doi:10.1039/c3lc51123e.

57. Cui, H. *et al.* 4D physiologically adaptable cardiac patch: A 4-month in vivo study for the treatment of myocardial infarction. *Sci. Adv.* (2020) doi:10.1126/sciadv.abb5067.

58. Seo, H. R. *et al.* Nanopillar Surface Topology Promotes Cardiomyocyte Differentiation through Cofilin-Mediated Cytoskeleton Rearrangement. *ACS Appl. Mater. Interfaces* (2017) doi:10.1021/acsami.7b01555.

59. Xu, C. *et al.* Bioinspired onion epithelium-like structure promotes the maturation of

cardiomyocytes derived from human pluripotent stem cells. *Biomater. Sci.* (2017) doi:10.1039/c7bm00132k.

60. Wanjare, M. *et al.* Anisotropic microfibrous scaffolds enhance the organization and function of cardiomyocytes derived from induced pluripotent stem cells. *Biomater. Sci.* (2017) doi:10.1039/c7bm00323d.
61. Allen, A. C. B. *et al.* Temporal Impact of Substrate Anisotropy on Differentiating Cardiomyocyte Alignment and Functionality. *Tissue Eng. - Part A* (2019) doi:10.1089/ten.tea.2018.0258.
62. Morez, C. *et al.* Enhanced efficiency of genetic programming toward cardiomyocyte creation through topographical cues. *Biomaterials* (2015) doi:10.1016/j.biomaterials.2015.07.063.
63. Ding, M. *et al.* Aligned nanofiber scaffolds improve functionality of cardiomyocytes differentiated from human induced pluripotent stem cell-derived cardiac progenitor cells. *Sci. Rep.* (2020) doi:10.1038/s41598-020-70547-4.
64. Li, J. *et al.* Human Pluripotent Stem Cell-Derived Cardiac Tissue-like Constructs for Repairing the Infarcted Myocardium. *Stem Cell Reports* (2017) doi:10.1016/j.stemcr.2017.09.007.
65. Zhu, C. *et al.* Increased Cardiomyocyte Alignment and Intracellular Calcium Transients Using Micropatterned and Drug-Releasing Poly(Glycerol Sebacate) Elastomers. *ACS Biomater. Sci. Eng.* (2018) doi:10.1021/acsbiomaterials.8b00084.
66. Oyunbaatar, N. E., Lee, D. H., Patil, S. J., Kim, E. S. & Lee, D. W. Biomechanical characterization of cardiomyocyte using PDMS pillar with microgrooves. *Sensors*

(Switzerland) (2016) doi:10.3390/s16081258.

67. Bian, W., Jackman, C. P. & Bursac, N. Controlling the structural and functional anisotropy of engineered cardiac tissues. *Biofabrication* (2014) doi:10.1088/1758-5082/6/2/024109.

68. Teng, C. J., Luo, J., Chiu, R. C. J. & Shum-Tim, D. Massive mechanical loss of microspheres with direct intramyocardial injection in the beating heart: Implications for cellular cardiomyoplasty. *J. Thorac. Cardiovasc. Surg.* (2006) doi:10.1016/j.jtcvs.2006.05.034.

69. Domenech, M., Polo-Corrales, L., Ramirez-Vick, J. E. & Freytes, D. O. Tissue engineering strategies for myocardial regeneration: Acellular versus cellular scaffolds? *Tissue Engineering - Part B: Reviews* (2016) doi:10.1089/ten.teb.2015.0523.

70. Zhang, G., Hu, Q., Braunlin, E. A., Suggs, L. J. & Zhang, J. Enhancing efficacy of stem cell transplantation to the heart with a PEGylated fibrin biomatrix. *Tissue Eng. - Part A.* (2008) doi:10.1089/ten.tea.2007.0289.

71. Kapnisi, M. *et al.* Auxetic Cardiac Patches with Tunable Mechanical and Conductive Properties toward Treating Myocardial Infarction. *Adv. Funct. Mater.* (2018) doi:10.1002/adfm.201800618.

72. Li, X. *et al.* A PNIPAAm-based thermosensitive hydrogel containing SWCNTs for stem cell transplantation in myocardial repair. *Biomaterials* (2014) doi:10.1016/j.biomaterials.2014.03.067.

73. Mccauley, M. D. *et al.* In Vivo Restoration of Myocardial Conduction With Carbon Nanotube Fibers. *Circ. Arrhythmia Electrophysiol.* (2019)

doi:10.1161/CIRCEP.119.007256.

74. Shah, R. R. Can pharmacogenetics help rescue drugs withdrawn from the market? *Pharmacogenomics* (2006) doi:10.2217/14622416.7.6.889.

75. Chen, A. *et al.* Integrated platform for functional monitoring of biomimetic heart sheets derived from human pluripotent stem cells. *Biomaterials* (2014) doi:10.1016/j.biomaterials.2013.10.007.

76. Shum, A. M. Y. *et al.* A Micropatterned Human Pluripotent Stem Cell-Based Ventricular Cardiac Anisotropic Sheet for Visualizing Drug-Induced Arrhythmogenicity. *Adv. Mater.* (2017) doi:10.1002/adma.201602448.

77. Xu, B. *et al.* Nanotopography-responsive myotube alignment and orientation as a sensitive phenotypic biomarker for Duchenne Muscular Dystrophy. *Biomaterials* (2018) doi:10.1016/j.biomaterials.2018.08.047.

78. Souders, C. A., Bowers, S. L. K. & Baudino, T. A. Cardiac fibroblast: The renaissance cell. *Circulation Research* (2009) doi:10.1161/CIRCRESAHA.109.209809.

79. Travers, J. G., Kamal, F. A., Robbins, J., Yutzey, K. E. & Blaxall, B. C. Cardiac fibrosis: The fibroblast awakens. *Circulation Research* (2016) doi:10.1161/CIRCRESAHA.115.306565.

80. Herum, K. M., Choppe, J., Kumar, A., Engler, A. J. & McCulloch, A. D. Mechanical regulation of cardiac fibroblast profibrotic phenotypes. *Mol. Biol. Cell* (2017) doi:10.1091/mbc.E17-01-0014.

81. Goffin, J. M. *et al.* Focal adhesion size controls tension-dependent recruitment of α-smooth muscle actin to stress fibers. *J. Cell Biol.* (2006)

doi:10.1083/jcb.200506179.

82. Robotti, F. *et al.* A micron-scale surface topography design reducing cell adhesion to implanted materials. *Sci. Rep.* (2018) doi:10.1038/s41598-018-29167-2.

83. Wang, K. *et al.* Nanotopographical Modulation of Cell Function through Nuclear Deformation. *ACS Appl. Mater. Interfaces* (2016) doi:10.1021/acsami.5b10531.

84. Majd, H. *et al.* Novel micropatterns mechanically control fibrotic reactions at the surface of silicone implants. *Biomaterials* (2015) doi:10.1016/j.biomaterials.2015.03.027.

85. Hinz, B. *et al.* Recent developments in myofibroblast biology: Paradigms for connective tissue remodeling. *American Journal of Pathology* (2012) doi:10.1016/j.ajpath.2012.02.004.

86. Alisafaei, F., Jokhun, D. S., Shivashankar, G. V. & Shenoy, V. B. Regulation of nuclear architecture, mechanics, and nucleocytoplasmic shuttling of epigenetic factors by cell geometric constraints. *Proc. Natl. Acad. Sci. U. S. A.* (2019) doi:10.1073/pnas.1902035116.

87. Wang, Y., Nagarajan, M., Uhler, C. & Shivashankar, G. V. Orientation and repositioning of chromosomes correlate with cell geometry-dependent gene expression. *Mol. Biol. Cell* (2017) doi:10.1091/mbc.E16-12-0825.

88. Le, L. V. *et al.* Injectable hyaluronic acid based microrods provide local micromechanical and biochemical cues to attenuate cardiac fibrosis after myocardial infarction. *Biomaterials* (2018) doi:10.1016/j.biomaterials.2018.03.042.

89. Pinney, J. R. *et al.* Discrete microstructural cues for the attenuation of fibrosis following myocardial infarction. *Biomaterials* (2014)

doi:10.1016/j.biomaterials.2014.07.005.

90. Lee, J. S. *et al.* Modulation of Foreign Body Reaction against PDMS Implant by Grafting Topographically Different Poly(acrylic acid) Micropatterns. *Macromol. Biosci.* (2019) doi:10.1002/mabi.201900206.

91. Kyle, D. J. T., Oikonomou, A., Hill, E. & Bayat, A. Development and functional evaluation of biomimetic silicone surfaces with hierarchical micro/nano-topographical features demonstrates favourable invitro foreign body response of breast-derived fibroblasts. *Biomaterials* (2015) doi:10.1016/j.biomaterials.2015.02.003.

92. Cutiongco, M. F. A., Jensen, B. S., Reynolds, P. M. & Gadegaard, N. Predicting gene expression using morphological cell responses to nanotopography. *Nat. Commun.* (2020) doi:10.1038/s41467-020-15114-1.

93. De Vicente, G. & Lensen, M. C. Topographically and elastically micropatterned PEG-based hydrogels to control cell adhesion and migration. *Eur. Polym. J.* (2016) doi:10.1016/j.eurpolymj.2016.03.020.

94. Kim, S. E. *et al.* Cell migration according to shape of graphene oxide micropatterns. *Micromachines* (2016) doi:10.3390/mi7100186.

95. Barros, S. A. de L. *et al.* Influence of zirconia-coated bioactive glass on gingival fibroblast behavior. *Braz. Dent. J.* (2019) doi:10.1590/0103-6440201902417.

96. Ge, L., Yang, L., Bron, R., Burgess, J. K. & Van Rijn, P. Topography-Mediated Fibroblast Cell Migration Is Influenced by Direction, Wavelength, and Amplitude. *ACS Appl. Bio Mater.* (2020) doi:10.1021/acsabm.0c00001.

97. Lim, J. *et al.* Constrained Adherable Area of Nanotopographic Surfaces Promotes

Cell Migration through the Regulation of Focal Adhesion via Focal Adhesion Kinase/Rac1 Activation. *ACS Appl. Mater. Interfaces* (2018) doi:10.1021/acsami.7b18954.

98. Zhan, C., Baine, W. B., Sedrakyan, A. & Steiner, C. Cardiac device implantation in the United States from 1997 through 2004: A population-based analysis. *J. Gen. Intern. Med.* **23**, 13–19 (2008).

99. Borek, P. P. & Wilkoff, B. L. Pacemaker and ICD leads: Strategies for long-term management. *Journal of Interventional Cardiac Electrophysiology* vol. 23 59–72 (2008).

100. Anderson, J. M., Rodriguez, A. & Chang, D. T. Foreign body reaction to biomaterials. *Seminars in Immunology* (2008) doi:10.1016/j.smim.2007.11.004.

101. Peña, J. R., Pinney, J. R., Ayala, P., Desai, T. A. & Goldspink, P. H. Localized delivery of mechano-growth factor E-domain peptide via polymeric microstructures improves cardiac function following myocardial infarction. *Biomaterials* (2015) doi:10.1016/j.biomaterials.2014.12.050.

102. Choe, G. *et al.* Anti-oxidant activity reinforced reduced graphene oxide/alginate microgels: Mesenchymal stem cell encapsulation and regeneration of infarcted hearts. *Biomaterials* (2019) doi:10.1016/j.biomaterials.2019.119513.

103. Robotti, F. *et al.* Microengineered biosynthesized cellulose as anti-fibrotic in vivo protection for cardiac implantable electronic devices. *Biomaterials* (2020) doi:10.1016/j.biomaterials.2019.119583.

104. Kirkfeldt, R. E., Johansen, J. B., Nohr, E. A., Jorgensen, O. D. & Nielsen, J. C. Complications after cardiac implantable electronic device implantations: An

analysis of a complete, nationwide cohort in Denmark. *Eur. Heart J.* (2014) doi:10.1093/eurheartj/eht511.

105. Poole, J. E. *et al.* Complication rates associated with pacemaker or implantable cardioverter-defibrillator generator replacements and upgrade procedures: Results from the REPLACE registry. *Circulation* (2010) doi:10.1161/CIRCULATIONAHA.110.976076.
106. Rajendran, P. *et al.* The vascular endothelium and human diseases. *International Journal of Biological Sciences* (2013) doi:10.7150/ijbs.7502.
107. Charbonier, F. W., Zamani, M. & Huang, N. F. Endothelial Cell Mechanotransduction in the Dynamic Vascular Environment. *Advanced Biosystems* (2019) doi:10.1002/adbi.201800252.
108. Pashneh-Tala, S., MacNeil, S. & Claeyssens, F. The tissue-engineered vascular graft - Past, present, and future. *Tissue Engineering - Part B: Reviews* (2016) doi:10.1089/ten.teb.2015.0100.
109. Krüger-Genge, A., Blocki, A., Franke, R. P. & Jung, F. Vascular endothelial cell biology: An update. *International Journal of Molecular Sciences* (2019) doi:10.3390/ijms20184411.
110. Gorji, A., Toh, P. J. Y., Toh, Y.-C., Toyama, Y. & Kanchanawong, P. Enhancement of endothelialization by topographical features is mediated by PTP1B-dependent endothelial adherens junctions remodeling. *bioRxiv* 766816 (2019) doi:10.1101/766816.
111. Mascharak, S. *et al.* YAP-dependent mechanotransduction is required for proliferation and migration on native-like substrate topography. *Biomaterials*

(2017) doi:10.1016/j.biomaterials.2016.11.019.

112. Ding, Y. *et al.* Directing vascular cell selectivity and hemocompatibility on patterned platforms featuring variable topographic geometry and size. *ACS Appl. Mater. Interfaces* (2014) doi:10.1021/am502692k.

113. Hagen, M. W. & Hinds, M. T. The Effects of Topographic Micropatterning on Endothelial Colony-Forming Cells. *Tissue Eng. Part A* (2020) doi:10.1089/ten.tea.2020.0066.

114. Kim, P., Yuan, A., Nam, K. H., Jiao, A. & Kim, D. H. Fabrication of poly(ethylene glycol): Gelatin methacrylate composite nanostructures with tunable stiffness and degradation for vascular tissue engineering. *Biofabrication* (2014) doi:10.1088/1758-5082/6/2/024112.

115. Antonini, S. *et al.* Sub-micron lateral topography affects endothelial migration by modulation of focal adhesion dynamics. *Biomed. Mater.* (2015) doi:10.1088/1748-6041/10/3/035010.

116. Liu, Y. *et al.* Biointerface topography mediates the interplay between endothelial cells and monocytes. *RSC Adv.* (2020) doi:10.1039/d0ra00704h.

117. Lamichhane, S. *et al.* Responses of endothelial cells, smooth muscle cells, and platelets dependent on the surface topography of polytetrafluoroethylene. *J. Biomed. Mater. Res. - Part A* (2016) doi:10.1002/jbm.a.35763.

118. Moffa, M., Sciancalepore, A. G., Passione, L. G. & Pisignano, D. Combined nano- and micro-scale topographic cues for engineered vascular constructs by electrospinning and imprinted micro-patterns. *Small* (2014) doi:10.1002/smll.201303179.

119. Fioretta, E. S., Simonet, M., Smits, A. I. P. M., Baaijens, F. P. T. & Bouten, C. V. C. Differential response of endothelial and endothelial colony forming cells on electrospun scaffolds with distinct microfiber diameters. *Biomacromolecules* (2014) doi:10.1021/bm4016418.

120. Robotti, F. *et al.* The influence of surface micro-structure on endothelialization under supraphysiological wall shear stress. *Biomaterials* (2014) doi:10.1016/j.biomaterials.2014.06.046.

121. Whited, B. M. & Rylander, M. N. The influence of electrospun scaffold topography on endothelial cell morphology, alignment, and adhesion in response to fluid flow. *Biotechnol. Bioeng.* (2014) doi:10.1002/bit.24995.

122. Cao, Y. & Desai, T. A. TiO2-Based Nanotopographical Cues Attenuate the Restenotic Phenotype in Primary Human Vascular Endothelial and Smooth Muscle Cells. *ACS Biomater. Sci. Eng.* (2020) doi:10.1021/acsbiomaterials.9b01475.

123. Shin, Y. M. *et al.* Engineering an aligned endothelial monolayer on a topologically modified nanofibrous platform with a micropatterned structure produced by femtosecond laser ablation. *J. Mater. Chem. B* (2017) doi:10.1039/c6tb02258h.

124. Cutiongco, M. F. A., Chua, B. M. X., Neo, D. J. H., Rizwan, M. & Yim, E. K. F. Functional differences between healthy and diabetic endothelial cells on topographical cues. *Biomaterials* (2018) doi:10.1016/j.biomaterials.2017.10.037.

125. Zhong, S. *et al.* Effects of polydopamine functionalized titanium dioxide nanotubes on endothelial cell and smooth muscle cell. *Colloids Surfaces B Biointerfaces* (2014) doi:10.1016/j.colsurfb.2014.01.030.

126. Lee, P. P. & Desai, T. A. Nitinol-Based Nanotubular Arrays with Controlled Diameters Upregulate Human Vascular Cell ECM Production. *ACS Biomater. Sci. Eng.* (2016) doi:10.1021/acsbiomaterials.5b00553.

127. Jeon, H. *et al.* Combined effects of substrate topography and stiffness on endothelial cytokine and chemokine secretion. *ACS Appl. Mater. Interfaces* (2015) doi:10.1021/acsami.5b00554.

128. Ilhan, F. Atherosclerosis and the role of immune cells. *World J. Clin. Cases* (2015) doi:10.12998/wjcc.v3.i4.345.

129. Chen, J. Y. *et al.* Improved Antithrombotic Function of Oriented Endothelial Cell Monolayer on Microgrooves. *ACS Biomater. Sci. Eng.* (2018) doi:10.1021/acsbiomaterials.7b00496.

130. Gaharwar, A. K., Nikkhah, M., Sant, S. & Khademhosseini, A. Anisotropic poly (glycerol sebacate)-poly (-caprolactone) electrospun fibers promote endothelial cell guidance. *Biofabrication* (2015) doi:10.1088/1758-5090/7/1/015001.

131. Kim, J. J. *et al.* Microfibrous Scaffolds Enhance Endothelial Differentiation and Organization of Induced Pluripotent Stem Cells. *Cell. Mol. Bioeng.* (2017) doi:10.1007/s12195-017-0502-y.

132. Kukumberg, M., Yao, J. Y., Neo, D. J. H. & Yim, E. K. F. Microlens topography combined with vascular endothelial growth factor induces endothelial differentiation of human mesenchymal stem cells into vasculogenic progenitors. *Biomaterials* (2017) doi:10.1016/j.biomaterials.2017.03.036.

133. Almonacid Suarez, A. M., van der Ham, I., Brinker, M. G. L., van Rijn, P. & Harmsen, M. C. Topography-driven alterations in endothelial cell phenotype and

contact guidance. *Heliyon* (2020) doi:10.1016/j.heliyon.2020.e04329.

134. Liang, C. *et al.* Biomimetic cardiovascular stents for in vivo re-endothelialization. *Biomaterials* (2016) doi:10.1016/j.biomaterials.2016.06.042.
135. Nuhn, H., Blanco, C. E. & Desai, T. A. Nanoengineered Stent Surface to Reduce In-Stent Restenosis in Vivo. *ACS Appl. Mater. Interfaces* (2017) doi:10.1021/acsami.7b04626.
136. Jang, T. S. *et al.* Ta ion implanted nanoridge-platform for enhanced vascular responses. *Biomaterials* (2019) doi:10.1016/j.biomaterials.2019.119461.
137. Nakayama, K. H. *et al.* Aligned-Braided Nanofibrillar Scaffold with Endothelial Cells Enhances Arteriogenesis. *ACS Nano* (2015) doi:10.1021/acsnano.5b00545.
138. Hu, C. *et al.* Delivery of Human Stromal Vascular Fraction Cells on Nanofibrillar Scaffolds for Treatment of Peripheral Arterial Disease. *Front. Bioeng. Biotechnol.* (2020) doi:10.3389/fbioe.2020.00689.
139. Wanjare, M. *et al.* Vascularization of Engineered Spatially Patterned Myocardial Tissue Derived From Human Pluripotent Stem Cells in vivo. *Front. Bioeng. Biotechnol.* (2019) doi:10.3389/fbioe.2019.00208.
140. Cutiongco, M. F. A. *et al.* Planar and tubular patterning of micro and nano-topographies on poly(vinyl alcohol) hydrogel for improved endothelial cell responses. *Biomaterials* (2016) doi:10.1016/j.biomaterials.2016.01.036.
141. Redd, M. A. *et al.* Patterned human microvascular grafts enable rapid vascularization and increase perfusion in infarcted rat hearts. *Nat. Commun.* (2019) doi:10.1038/s41467-019-08388-7.
142. Brady, E. L. *et al.* Guided vascularization in the rat heart leads to transient vessel

patterning. *APL Bioeng.* (2020) doi:10.1063/1.5122804.

143. Jamaiyar, A. *et al.* Alignment of inducible vascular progenitor cells on a micro-bundle scaffold improves cardiac repair following myocardial infarction. *Basic Res. Cardiol.* (2017) doi:10.1007/s00395-017-0631-4.
144. Zhu, M. *et al.* Circumferentially aligned fibers guided functional neoartery regeneration in vivo. *Biomaterials* (2015) doi:10.1016/j.biomaterials.2015.05.024.
145. Muhammad, R. *et al.* Micro- and nano-topography to enhance proliferation and sustain functional markers of donor-derived primary human corneal endothelial cells. *Acta Biomater.* (2015) doi:10.1016/j.actbio.2015.03.016.
146. Tallawi, M. *et al.* Novel PGS/PCL electrospun fiber mats with patterned topographical features for cardiac patch applications. *Mater. Sci. Eng. C* **69**, 569–576 (2016).
147. Mummery, C. L. *et al.* Differentiation of Human ES and iPS Cells to Cardiomyocytes: A Methods Overview. *Circ. Res.* (2012).
148. Yuan, H. *et al.* Highly aligned core-shell structured nanofibers for promoting phenotypic expression of vSMCs for vascular regeneration. *Nanoscale* (2016) doi:10.1039/c6nr05075a.
149. Crapo, P. M. & Wang, Y. Physiologic compliance in engineered small-diameter arterial constructs based on an elastomeric substrate. *Biomaterials* (2010) doi:10.1016/j.biomaterials.2009.11.035.
150. Pan, Y. *et al.* Small-diameter hybrid vascular grafts composed of polycaprolactone and polydioxanone fibers. *Sci. Rep.* (2017) doi:10.1038/s41598-017-03851-1.

151. Tara, S. *et al.* Well-organized neointima of large-pore poly(l-lactic acid) vascular graft coated with poly(l-lactic-co-ε-caprolactone) prevents calcific deposition compared to small-pore electrospun poly(l-lactic acid) graft in a mouse aortic implantation model. *Atherosclerosis* (2014) doi:10.1016/j.atherosclerosis.2014.09.030.

152. Gao, Y. *et al.* Pilot Mouse Study of 1 mm Inner Diameter (ID) Vascular Graft Using Electrospun Poly(ester urea) Nanofibers. *Adv. Healthc. Mater.* (2016) doi:10.1002/adhm.201600400.

153. Gupta, P., Moses, J. C. & Mandal, B. B. Surface Patterning and Innate Physicochemical Attributes of Silk Films Concomitantly Govern Vascular Cell Dynamics. *ACS Biomater. Sci. Eng.* (2019) doi:10.1021/acsbiomaterials.8b01194.

154. Hotchkiss, K. M. *et al.* Titanium surface characteristics, including topography and wettability, alter macrophage activation. *Acta Biomater.* (2016) doi:10.1016/j.actbio.2015.12.003.

155. Sugiura, T. *et al.* Novel Bioresorbable Vascular Graft With Sponge-Type Scaffold as a Small-Diameter Arterial Graft. in *Annals of Thoracic Surgery* (2016). doi:10.1016/j.athoracsur.2016.01.110.

156. Liguori, G. R. *et al.* Directional topography influences adipose mesenchymal stromal cell plasticity: Prospects for tissue engineering and fibrosis. *Stem Cells Int.* (2019) doi:10.1155/2019/5387850.

157. George, B. Regulation of Combination Products—Evolving Landscape. *Encycl. Tissue Eng. Regen. Med.* **1**–**3**, 207–213 (2019).

158. Guidance for Industry and FDA Staff: Early Development Considerations for

Innovative Combination Products. (2006).

159. eCFR :: 21 CFR 3.2 -- Definitions. https://www.ecfr.gov/current/title-21/chapter-I/subchapter-A/part-3/subpart-A/section-3.2.

160. Cogle, C. R. *et al.* An Overview of Stem Cell Research and Regulatory Issues. *Mayo Clin. Proc.* **78**, 993–1003 (2003).

161. Prestwich, G. D. *et al.* What is the greatest regulatory challenge in the translation of biomaterials to the clinic? *Sci. Transl. Med.* **4**, (2012).

162. Qiu, T., Hanna, E., Dabbous, M., Borislav, B. & Toumi, M. Regenerative medicine regulatory policies: A systematic review and international comparison. *Health Policy (New. York).* **124**, 701–713 (2020).

163. Segura, A. M., Frazier, O. H. & Buja, L. M. Fibrosis and heart failure. *Heart Fail. Rev.* **19**, 173–185 (2014).

164. Frangogiannis, N. G. Pathophysiology of Myocardial Infarction. *Compr. Physiol.* **5**, 1841–1875 (2015).

165. Denton, C. P. *et al.* Recombinant human anti-transforming growth factor β1 antibody therapy in systemic sclerosis: A multicenter, randomized, placebo-controlled phase I/II trial of CAT-192. *Arthritis Rheum.* **56**, 323–333 (2007).

166. Shi, N. *et al.* Research progress on drugs targeting the TGF-β signaling pathway in fibrotic diseases. *Immunol. Res. 2022* **1**, 1–13 (2022).

167. Mohindra, P. & Desai, T. Micro- and nanoscale biophysical cues for cardiovascular disease therapy. *Nanomedicine Nanotechnology, Biol. Med.* 102365 (2021) doi:10.1016/j.nano.2021.102365.

168. Curtis, M. W. & Russell, B. Micromechanical regulation in cardiac myocytes and

fibroblasts: implications for tissue remodeling. *Pflugers Arch.* **462**, 105–117 (2011).

169. Hinz, B. The myofibroblast: paradigm for a mechanically active cell. *J. Biomech.* **43**, 146–155 (2010).
170. Orr, A. W., Helmke, B. P., Blackman, B. R. & Schwartz, M. A. Mechanisms of mechanotransduction. *Dev. Cell* **10**, 11–20 (2006).
171. Allen, J. *et al.* Tunable Microfibers Suppress Fibrotic Encapsulation via Inhibition of TGFβ Signaling. *Tissue Eng. - Part A* (2016) doi:10.1089/ten.tea.2015.0087.
172. Ayala, P. & Desai, T. A. Integrin α3 blockade enhances microtopographical down-regulation of α-smooth muscle actin: role of microtopography in ECM regulation. *Integr. Biol.* **3**, 733–741 (2011).
173. Yang, C. *et al.* The High and Low Molecular Weight Forms of Hyaluronan Have Distinct Effects on CD44 Clustering. *J. Biol. Chem.* **287**, 43094 (2012).
174. Slevin, M. *et al.* Hyaluronan-mediated angiogenesis in vascular disease: Uncovering RHAMM and CD44 receptor signaling pathways. *Matrix Biol.* **26**, 58–68 (2007).
175. Gao, F., Yang, C. X., Mo, W., Liu, Y. W. & He, Y. Q. Hyaluronan oligosaccharides are potential stimulators to angiogenesis via RHAMM mediated signal pathway in wound healing. *Clin. Investig. Med.* **31**, E106–E116 (2008).
176. Wang, Y., Han, G., Guo, B. & Huang, J. Hyaluronan oligosaccharides promote diabetic wound healing by increasing angiogenesis. *Pharmacol. Reports* **68**, 1126–1132 (2016).
177. Cyphert, J. M., Trempus, C. S. & Garantziotis, S. Size Matters: Molecular Weight

Specificity of Hyaluronan Effects in Cell Biology. *Int. J. Cell Biol.* **2015**, (2015).

178. Garantziotis, S. & Savani, R. C. Hyaluronan biology: A complex balancing act of structure, function, location and context. *Matrix Biol.* **78**–**79**, 1 (2019).
179. Bencherif, S. A. *et al.* Influence of the degree of methacrylation on hyaluronic acid hydrogels properties. *Biomaterials* **29**, 1739–1749 (2008).
180. Mihardja, S. S. *et al.* The effect of a peptide-modified thermo-reversible methylcellulose on wound healing and LV function in a chronic myocardial infarction rodent model. *Biomaterials* **34**, 8869–8877 (2013).
181. Kim, Y. & Kumar, S. CD44-mediated Adhesion to Hyaluronic Acid Contributes to Mechanosensing and Invasive Motility. *Mol. Cancer Res.* **12**, 1416 (2014).
182. Entwistle, J., Hall, C. L. & Turley, E. A. HA receptors: regulators of signalling to the cytoskeleton. *J. Cell. Biochem.* **61**, 569–577 (1996).
183. Tous, E. *et al.* Influence of injectable hyaluronic acid hydrogel degradation behavior on infarction-induced ventricular remodeling. *Biomacromolecules* **12**, 4127–4135 (2011).
184. So, J. Y. *et al.* Regeneration of ischemic heart using hyaluronic acid-based injectable hydrogel. *J. Biomed. Mater. Res. B. Appl. Biomater.* **91**, 163–171 (2009).
185. Ifkovits, J. L. *et al.* Injectable hydrogel properties influence infarct expansion and extent of postinfarction left ventricular remodeling in an ovine model. *Proc. Natl. Acad. Sci. U. S. A.* **107**, 11507–11512 (2010).
186. Bhattacharya, D. S. *et al.* Impact of structurally modifying hyaluronic acid on CD44 interaction. *J. Mater. Chem. B* **5**, 8183–8192 (2017).

187. Zeng, H. & Chen, J. X. Microvascular Rarefaction and Heart Failure With Preserved Ejection Fraction. *Front. Cardiovasc. Med.* **6**, 15 (2019).

188. Robich, M. P., Chu, L. M., Oyamada, S., Sodha, N. R. & Sellke, F. W. Myocardial Therapeutic Angiogenesis: A Review of the State of Development and Future Obstacles. *Expert Rev. Cardiovasc. Ther.* **9**, 1469 (2011).

189. Sellke, F. W., Laham, R. J., Edelman, E. R., Pearlman, J. D. & Simons, M. Therapeutic angiogenesis with basic fibroblast growth factor: technique and early results. *Ann. Thorac. Surg.* **65**, 1540–1544 (1998).

190. Sabra, M. *et al.* Clinical Application of Novel Therapies for Coronary Angiogenesis: Overview, Challenges, and Prospects. *Int. J. Mol. Sci.* **22**, (2021).

191. Ruel, M. *et al.* Concomitant treatment with oral L-arginine improves the efficacy of surgical angiogenesis in patients with severe diffuse coronary artery disease: the Endothelial Modulation in Angiogenic Therapy randomized controlled trial. *J. Thorac. Cardiovasc. Surg.* **135**, (2008).

192. Hedman, M. *et al.* Safety and feasibility of catheter-based local intracoronary vascular endothelial growth factor gene transfer in the prevention of postangioplasty and in-stent restenosis and in the treatment of chronic myocardial ischemia: Phase II results of the Kuopio angiogenesis trial (KAT). *Circulation* **107**, 2677–2683 (2003).

193. Henry, T. D. *et al.* Effects of Ad5FGF-4 in Patients With Angina: An Analysis of Pooled Data From the AGENT-3 and AGENT-4 Trials. *J. Am. Coll. Cardiol.* **50**, 1038–1046 (2007).

194. Lee, R. J. *et al.* VEGF Gene Delivery to Myocardium. *Circulation* **102**, 898–901

(2000).

195. Yin, N. *et al.* VEGF-conjugated alginate hydrogel prompt angiogenesis and improve pancreatic islet engraftment and function in type 1 diabetes. *Mater. Sci. Eng. C* **59**, 958–964 (2016).

196. Vijayan, A., Sabareeswaran, A. & Kumar, G. S. V. PEG grafted chitosan scaffold for dual growth factor delivery for enhanced wound healing. *Sci. Rep.* **9**, (2019).

197. Davies, N. H., Schmidt, C., Bezuidenhout, D. & Zilla, P. Sustaining Neovascularization of a Scaffold Through Staged Release of Vascular Endothelial Growth Factor-A and Platelet-Derived Growth Factor-BB. *Tissue Eng. Part A* **18**, 26 (2012).

198. Prokoph, S. *et al.* Sustained delivery of SDF-1α from heparin-based hydrogels to attract circulating pro-angiogenic cells. *Biomaterials* **33**, 4792–4800 (2012).

199. D'Andrea, L. D. *et al.* Targeting angiogenesis: Structural characterization and biological properties of a de novo engineered VEGF mimicking peptide. *Proc. Natl. Acad. Sci. U. S. A.* **102**, 14215–14220 (2005).

200. Santulli, G. *et al.* In vivo properties of the proangiogenic peptide QK. *J. Transl. Med.* **7**, 1–10 (2009).

201. Hardy, B., Battler, A., Weiss, C., Kudasi, O. & Raiter, A. Therapeutic angiogenesis of mouse hind limb ischemia by novel peptide activating GRP78 receptor on endothelial cells. *Biochem. Pharmacol.* **75**, 891–899 (2008).

202. Raiter, A. *et al.* Activation of GRP78 on endothelial cell membranes by an ADAM15-derived peptide induces angiogenesis. *J. Vasc. Res.* **47**, 399–411 (2010).

203. Mihardja, S. S. *et al.* Targeted In Vivo Extracellular Matrix Formation Promotes Neovascularization in a Rodent Model of Myocardial Infarction. doi:10.1371/journal.pone.0010384.

204. Namba, T. *et al.* Angiogenesis Induced by Endothelial Nitric Oxide Synthase Gene Through Vascular Endothelial Growth Factor Expression in a Rat Hindlimb Ischemia Model. *Circulation* **108**, 2250–2257 (2003).

205. Potente, M., Gerhardt, H. & Carmeliet, P. Basic and Therapeutic Aspects of Angiogenesis. *Cell* **146**, 873–887 (2011).

206. Meier, P. *et al.* Beneficial effect of recruitable collaterals: A 10-year follow-up study in patients with stable coronary artery disease undergoing quantitative collateral measurements. *Circulation* **116**, 975–983 (2007).

207. Kobayashi, K. *et al.* Dynamics of angiogenesis in ischemic areas of the infarcted heart. *Sci. Reports 2017 71* **7**, 1–13 (2017).

208. Lim, S. Y. *et al.* Ischemic preconditioning promotes intrinsic vascularization and enhances survival of implanted cells in an in vivo tissue engineering model. *Tissue Eng. Part A* **18**, 2210–2219 (2012).

209. Bouchentouf, M. *et al.* Vascular endothelial growth factor reduced hypoxia-induced death of human myoblasts and improved their engraftment in mouse muscles. *Gene Ther.* **15**, 404–414 (2008).

210. Azarnoush, K. *et al.* Enhancement of the functional benefits of skeletal myoblast transplantation by means of coadministration of hypoxia-inducible factor 1α. *J. Thorac. Cardiovasc. Surg.* **130**, 173–179 (2005).

211. Lunde, K. *et al.* Intracoronary injection of mononuclear bone marrow cells in acute

myocardial infarction. *N. Engl. J. Med.* **355**, 1199–1209 (2006).

212. Hosoyama, K., Lazurko, C., Muñoz, M., McTiernan, C. D. & Alarcon, E. I. Peptide-based functional biomaterials for soft-tissue repair. *Front. Bioeng. Biotechnol.* **7**, 205 (2019).
213. Setty, S. *et al.* Interactions of Type IV Collagen and Its Domains with Human Mesangial Cells *. *J. Biol. Chem.* **273**, 12244–12249 (1998).
214. Maldonado, B. A. & Furcht, L. T. Involvement of integrins with adhesion-promoting, heparin-binding peptides of type IV collagen in cultured human corneal epithelial cells. | IOVS | ARVO Journals. *Investig. Ophthalmol. Vis. Sci.* **36**, (1995).
215. Senger, D. R. *et al.* The α1β1 and α2β1 Integrins Provide Critical Support for Vascular Endothelial Growth Factor Signaling, Endothelial Cell Migration, and Tumor Angiogenesis. *Am. J. Pathol.* **160**, 195–204 (2002).
216. Manohar, A. *et al.* Alpha 3 beta 1 integrin promotes keratinocyte cell survival through activation of a MEK/ERK signaling pathway. *J. Cell Sci.* **117**, 4043–4054 (2004).
217. Kuwabara, M. *et al.* Nitric oxide stimulates vascular endothelial growth factor production in cardiomyocytes involved in angiogenesis. *J. Physiol. Sci.* **56**, 95–101 (2006).
218. Parenti, A. *et al.* Nitric Oxide Is an Upstream Signal of Vascular Endothelial Growth Factor-induced Extracellular Signal-regulated Kinase½ Activation in Postcapillary Endothelium *. *J. Biol. Chem.* **273**, 4220–4226 (1998).
219. Hood, J. D., Meininger, C. J., Ziche, M. & Granger, H. J. VEGF upregulates

ecNOS message, protein, and NO production in human endothelial cells. *Am. J. Physiol.* **274**, (1998).

220. Raiter, A. *et al.* Angiogenic peptides improve blood flow and promote capillary growth in a diabetic and ischaemic mouse model. *Eur. J. Vasc. Endovasc. Surg.* **40**, 381–388 (2010).
221. Virani, S. S. *et al.* Heart Disease and Stroke Statistics—2021 Update. *Circulation* **143**, E254–E743 (2021).
222. Wu, T. *et al.* Minimal evidence of transdifferentiation from recipient bone marrow to parenchymal cells in regenerating and long-surviving human allografts. *Am. J. Transplant* **3**, 1173–1181 (2003).
223. Tang, X. L. *et al.* Long-Term Outcome of Administration of c-kitPOS Cardiac Progenitor Cells After Acute Myocardial Infarction: Transplanted Cells Do Not Become Cardiomyocytes, Structural and Functional Improvement and Proliferation of Endogenous Cells Persist for at Least One Year. *Circ. Res.* **118**, 1091 (2016).
224. Rosenbloom, J., Mendoza, F. A. & Jimenez, S. A. Strategies for anti-fibrotic therapies. *Biochim. Biophys. Acta* **1832**, 1088–1103 (2013).
225. Denton, C. P. *et al.* Recombinant human anti-transforming growth factor beta1 antibody therapy in systemic sclerosis: a multicenter, randomized, placebo-controlled phase I/II trial of CAT-192. *Arthritis Rheum.* **56**, 323–333 (2007).
226. Mohindra, P. & Desai, T. A. Micro- and nanoscale biophysical cues for cardiovascular disease therapy. *Nanomedicine Nanotechnology, Biol. Med.* **34**, 102365 (2021).

227. Travers, J. G., Kamal, F. A., Robbins, J., Yutzey, K. E. & Blaxall, B. C. Cardiac Fibrosis. *Circ. Res.* **118**, 1021–1040 (2016).

228. Ayala, P., Lopez, J. I. & Desai, T. A. Microtopographical Cues in 3D Attenuate Fibrotic Phenotype and Extracellular Matrix Deposition: Implications for Tissue Regeneration. *Tissue Eng. Part A* **16**, 2519 (2010).

229. Allen, J. *et al.* Tunable Microfibers Suppress Fibrotic Encapsulation via Inhibition of TGFβ Signaling. *Tissue Eng. Part A* **22**, 142 (2016).

230. Pinney, J. R. *et al.* Discrete Microstructural Cues for the Attenuation of Fibrosis Following Myocardial Infarction. *Biomaterials* **35**, 8820 (2014).

231. Le, L. V. *et al.* Injectable hyaluronic acid based microrods provide local micromechanical and biochemical cues to attenuate cardiac fibrosis after myocardial infarction. *Biomaterials* **169**, 11–21 (2018).

232. Rivera, K. O. *et al.* Localized delivery of β-NGF via injectable microrods accelerates endochondral fracture repair. *bioRxiv* 2021.11.16.468864 (2021) doi:10.1101/2021.11.16.468864.

233. Neri, M., Riezzo, I., Pascale, N., Pomara, C. & Turillazzi, E. Ischemia/Reperfusion Injury following Acute Myocardial Infarction: A Critical Issue for Clinicians and Forensic Pathologists. *Mediators Inflamm.* **2017**, (2017).

234. Verma, S. *et al.* Fundamentals of reperfusion injury for the clinical cardiologist. *Circulation* **105**, 2332–2336 (2002).

235. Takawale, A. *et al.* Myocardial recovery from ischemia-reperfusion is compromised in the absence of tissue inhibitor of metalloproteinase 4. *Circ. Hear. Fail.* **7**, 652–662 (2014).

236. Kalamajski, S. & Oldberg, A. The role of small leucine-rich proteoglycans in collagen fibrillogenesis. *Matrix Biol.* **29**, 248–253 (2010).

237. Reese, S. P., Underwood, C. J. & Weiss, J. A. Effects of decorin proteoglycan on fibrillogenesis, ultrastructure, and mechanics of type I collagen gels. *Matrix Biol.* **32**, 414–423 (2013).

238. Iwasaki, S. *et al.* The modulation of collagen fibril assembly and its structure by decorin: an electron microscopic study. *Arch. Histol. Cytol.* **71**, 37–44 (2008).

239. Raspanti, M., Viola, M., Sonaggere, M., Tira, M. E. & Tenni, R. Collagen fibril structure is affected by collagen concentration and decorin. *Biomacromolecules* **8**, 2087–2091 (2007).

240. Rada, J. A., Cornuet, P. K. & Hassell, J. R. Regulation of corneal collagen fibrillogenesis in vitro by corneal proteoglycan (lumican and decorin) core proteins. *Exp. Eye Res.* **56**, 635–648 (1993).

241. Yamaguchi, Y., Mann, D. M. & Ruoslahti, E. Negative regulation of transforming growth factor-beta by the proteoglycan decorin. *Nature* **346**, 281–284 (1990).

242. Hildebrand, A. *et al.* Interaction of the small interstitial proteoglycans biglycan, decorin and fibromodulin with transforming growth factor beta. *Biochem. J.* **302 (Pt 2)**, 527–534 (1994).

243. Hill, L. J. *et al.* Sustained release of decorin to the surface of the eye enables scarless corneal regeneration. *NPJ Regen. Med.* **3**, (2018).

244. Alan, C., Kocoglu, H., Altintas, R., Alici, B. & Ersay, A. R. Protective effect of decorin on acute ischaemia-reperfusion injury in the rat kidney. *Arch. Med. Sci.* **7**, 211–216 (2011).

245. Faust, S. M., Lu, G., Wood, S. C. & Bishop, D. K. Transforming Growth Factor β Neutralization within Cardiac Allografts by Decorin Gene Transfer Attenuates Chronic Rejection. *J. Immunol.* **183**, 7307 (2009).

246. Li, L. *et al.* Postinfarction gene therapy with adenoviral vector expressing decorin mitigates cardiac remodeling and dysfunction. *Am. J. Physiol. Heart Circ. Physiol.* **297**, (2009).

247. Zhang, Z. *et al.* Recombinant human decorin inhibits TGF-β1-induced contraction of collagen lattice by hypertrophic scar fibroblasts. *Burns* **35**, 527–537 (2009).

248. Mohan, R. R., Gupta, R., Mehan, M. K., Cowden, J. W. & Sinha, S. Decorin transfection suppresses profibrogenic genes and myofibroblast formation in human corneal fibroblasts. *Exp. Eye Res.* **91**, 238–245 (2010).

249. Kwan, P., Ding, J. & Tredget, E. E. MicroRNA 181b regulates decorin production by dermal fibroblasts and may be a potential therapy for hypertrophic scar. *PLoS One* **10**, e0123054–e0123054 (2015).

250. Özay, R. *et al.* Does Decorin Protect Neuronal Tissue via Its Antioxidant and Antiinflammatory Activity from Traumatic Brain Injury? An Experimental Study. *World Neurosurg.* **97**, 407–415 (2017).

251. Du, S., Shao, J., Xie, D. & Zhang, F. Decorin inhibits glucose-induced lens epithelial cell apoptosis via suppressing p22phox-p38 MAPK signaling pathway. *PLoS One* **15**, (2020).

252. Santra, M. *et al.* Protection of adult mouse progenitor cells and human glioma cells by de novo decorin expression in an oxygen- and glucose-deprived cell culture model system. *J. Cereb. Blood Flow Metab.* **26**, 1311–1322 (2006).

253. Takeuchis, Y., Kodama, Y. & Matsumoto, T. THE JOURNAL OF BIOLOGICAL CHEMISTRY Bone Matrix Decorin Binds Transforming Growth Factor+ and Enhances Its Bioactivity*. **269**, 3263632638 (1994).

254. Gubbiotti, M. A., Vallet, S. D., Ricard-Blum, S. & Iozzo, R. V. Decorin interacting network: A comprehensive analysis of decorin-binding partners and their versatile functions. *Matrix Biol.* **55**, 7 (2016).

255. Weis, S. M. *et al.* A role for decorin in the remodeling of myocardial infarction. *Matrix Biol.* **24**, 313–324 (2005).

256. Hao, J. *et al.* Elevation of Expression of Smads 2, 3, and 4, Decorin and TGF-βin the Chronic Phase of Myocardial Infarct Scar Healing. *J. Mol. Cell. Cardiol.* **31**, 667–678 (1999).

257. Alan, C., Kocoglu, H., Altintas, R., Alici, B. & Ersay, A. R. Protective effect of decorin on acute ischaemia-reperfusion injury in the rat kidney. *Arch. Med. Sci.* **7**, 211 (2011).

258. Yan, W. *et al.* Decorin Gene Delivery Inhibits Cardiac Fibrosis in Spontaneously Hypertensive Rats by Modulation of Transforming Growth Factor-β/Smad and p38 Mitogen-Activated Protein Kinase Signaling Pathways. *https://home.liebertpub.com/hum* **20**, 1190–1200 (2009).

259. Lee, L. C. hua., Zhihong, Z., Hinson, A. & Guccione, J. M. Reduction in Left Ventricular Wall Stress and Improvement in Function in Failing Hearts using Algisyl-LVR. *J. Vis. Exp.* 50096 (2013) doi:10.3791/50096.

260. Yang, Y., Yu, W. wei, Yan, W. & Xia, Q. Decorin Induces Cardiac Hypertrophy by Regulating the CaMKII/MEF-2 Signaling Pathway In Vivo. *Curr. Med. Sci. 2021*

415 **41**, 857–862 (2021).

Publishing Agreement

It is the policy of the University to encourage open access and broad distribution of all theses, dissertations, and manuscripts. The Graduate Division will facilitate the distribution of UCSF theses, dissertations, and manuscripts to the UCSF Library for open access and distribution. UCSF will make such theses, dissertations, and manuscripts accessible to the public and will take reasonable steps to preserve these works in perpetuity.

I hereby grant the non-exclusive, perpetual right to The Regents of the University of California to reproduce, publicly display, distribute, preserve, and publish copies of my thesis, dissertation, or manuscript in any form or media, now existing or later derived, including access online for teaching, research, and public service purposes.

DocuSigned by:
Priya Mohindra
EF33C80F40DC476...
Author Signature

5/27/2022
Date